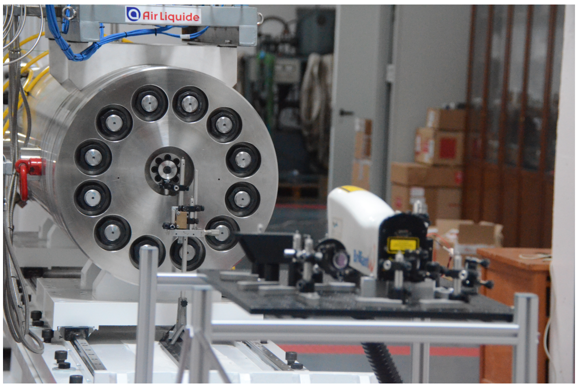

High-Pressure He/H_2/O_2 Mixtures Combustion on the ESTHER Driver: Experiment and Modeling

Beatriz Querido Oliveira

Thesis to obtain the Master of Science Degree in

Aerospace Engineering

Supervisor: Prof. Mário António Prazeres Lino da Silva

Examination Committee

Chairperson: Prof. Fernando José Parracho Lau
Supervisor: Prof. Mário António Prazeres Lino da Silva
Member of the Committee: Prof. Miguel Abreu de Almeida Mendes

November 2021

Dedicated to my parents, sister, and loved ones.

Acknowledgments

First of all, I would like to thank my supervisor Professor Mário Lino da Silva, for giving me the opportunity of working on such an amazing and interesting project that is the development of a shock tube, and also for his guidance and support. I would also like to thank Duarte Gonçalves, for always being available to help and support with the SPARK code, and Ricardo Ferreira, for his support during ESTHER's combustion driver experimental campaign.

To my parents, for all the unconditional support, love, and the freedom of choice and trust that you always gave me.

To my big sister, the person that knows me the best and that has always been a friend and inspiration to me.

To my dear friends, that accompanied me during this demanding journey, for all your friendship, amazing moments, and for showing me the value of teamwork.

Resumo

O tube de choque ESTHER é uma nova instalação no Instituto Superior Técnico destinado ao apoio de missões de exploração planetária sob o financiamento da ESA. O *driver* de combustão é operado com uma mistura de $\mathrm{He/H_2/O_2}$ e a ignição é conseguida via laser.

O principal objetivo deste trabalho é compreender a influência que o driver tem no desempenho do tubo de choque e estudar a combustão a altas pressões. É também feito um estudo de CFD de combustão a altas pressões de chamas pré-misturadas de $\mathrm{He/H_2/O_2}$ em livre expansão.

A temperatura e a pressão pós-combustão são os principais parâmetros do driver que influenciam o desempenho, onde para pressões e temperaturas mais elevadas, o desempenho aumenta. Ao alterar o diluente de He para $\mathrm{N_2}$, é possível obter um desempenho inferior, uma vez que a mistura de gás é mais pesada e a temperatura de combustão mais baixa.

O desempenho do driver depende principalmente da pressão inicial e da composição do gás. À medida que a diluição diminui, o desencadeamento de detonações é mais provável. Para pressões mais elevadas, a amplitude das ondas acústicas aumenta, mas este comportamento é amortecido se a quantidade de $\mathrm{O_2}$ for aumentada. O desempenho e a repetibilidade do driver também foram comprovados.

No estudo de combustão *CFD*, o código SPARK foi utilizado para modelar chamas 2D pré-misturadas e obter a velocidade da chama laminar. Embora os resultados não correspondam aos valores experimentais, algumas tendências corretas são reproduzidas numericamente e foram identificadas algumas falhas nos modelos utilizados.

Palavras-chave: Tubo de choque, *Driver* de combustão, Combustão a altas pressões, Mecânica de Fluidos Computacional

Abstract

The ESTHER shock tube is a new kinetic facility at Instituto Superior Técnico to support planetary exploration missions under the funding of the European Space Agency. The ESTHER combustion driver is operated with an initial mixture of $\mathrm{He/H_2/O_2}$ and ignition is achieved with a laser pulse.

The main goal is to understand the influence that the ESTHER combustion driver has on the performance of the shock tube and study the high-pressure combustion that takes place inside the driver. Besides this, a CFD high-pressure combustion study of freely expanding premixed flames of $\mathrm{He/H_2/O_2}$ is done.

It was found that the post-combustion temperature and pressure are the main driver parameters that influence the performance, where for higher pressures and temperatures, the performance increases. By changing the driver gas diluent from He to $\mathrm{N_2}$, lower performance can be achieved since the gas mixture is heavier and the combustion temperature is lower.

The driver performance depends mostly on the initial filling pressure and gas composition. It was found that as the dilution decreases the onset of detonations is more likely. For higher filling pressures, the amplitude of the acoustic waves increased significantly, but this behaviour would be damped if the ratio of $\mathrm{O_2}$ was increased. The performance and repeatability of the driver were proven.

In the CFD combustion study, the main goal was to use SPARK to model 2D laminar premixed flames and obtain the laminar flame speed. Although the results do not correspond to the experimental values, some models shortfalls were identified.

Keywords: Shock tube, Combustion driver, High pressure combustion, Hydrogen, Computational Fluid Dynamics

Contents

List of Tables

List of Figures

Nomenclature

Greek symbols

α	Thermal diffusivity.
β	Parameter dependent on the boundary layer development layer.
δ_{bl}	Boundary layer thickness.
δ_f	Flame thickness.
γ	Ratio of specific heats.
κ	Thermal conductivity coefficient.
λ	Air-fuel equivalence ratio.
μ	Dynamic viscosity coefficient.
ν	Kinematic viscosity coefficient.
Ω	Sorce term contribution.
ρ	Density.
τ	Test time.
$[\boldsymbol{\tau}]$	Viscous stress tensor.

Roman symbols

$[\mathbf{I}]$	Identity matrix.
$[X]$	Species concentration.
$\boldsymbol{U}$	Velocity vector.
$\mathcal{M}$	Molar mass.
$\mathcal{R}$	Ideal gas constant.
$\mathfrak{n}$	Overall reaction order.
$\mathscr{D}$	Molecular diffusivity.

A	Area.
a	Speed of sound.
c_i	Chemical species i mass fraction.
c_p	Specific heat at constant pressure.
c_v	Specific heat at constant volume.
D	Dilution ratio.
d	Diameter.
E	Internal energy.
E_a	Activation energy.
f	Frequency.
G	Universal gravitational constant.
g	Equivalent factor defined by Alpher and White.
H	Enthalpy.
J	Dissipative flux vector.
k	Chemical rate coefficient.
k_G	Global rate coefficient.
l	Length.
Le	Lewis number.
M	Mach number.
m	Mass.
n	Number of moles.
p	Pressure.
Q	Heat release rate.
R	Specific gas constant.
r	Radius.
S	Flame propagation velocity.
S_L	Laminar flame velocity.
S_L^0	Unstretched laminar flame velocity.

T	Temperature.
t	Time.
u	Velocity.
x_1	Shock tube length.
x_7	Compression tube length.
x_i	Chemical species i mole fraction.
x_{11}	Compression tube length.
$\dot{m}_b$	Mass burning rate.
${\dot{m}_b}^0$	Laminar mass burning rate.

Subscripts

0	Free stream conditions directly downstream of the shock wave.
1	Working tube initial state.
10	Tail of unsteady expansion driver gas state.
11	Driver tube initial state.
2	Post-shock state.
3	Unsteadily expanded test gas state.
$3a$	Unsteadily expanded test gas state for single diaphragm with variable area shock tubes.
$3b$	Steadily expanded test gas state for single diaphragm with variable area and convergent geometry shock tubes.
$3b'$	Steadily expanded test gas state for single diaphragm with variable area shock tubes.
4	Intermediate throat state/driver tube initial state for single diaphragm shock tubes.
5	Reflected gas state.
6	Intermediate post-shock state.
7	Intermediate pre-shock state.
8	Unsteadily expanded intermediate gas state.
9	Driver throat state.
ac	Accoustic.
ad	Adiabatic.

b	Burned.
c	Contact surface.
dil	Diluent.
e	Free stream conditions.
$init$	Initial.
l_m	Development distance of the boundary layer.
s	Shock.
u	Unburned.
w	Wall.

Glossary

ADST Arc-Driven Shock Tube.

CEA Chemical Equilibrium with Applications.

CFD Computational Fluid Dynamics.

CTN Campus Tecnológico e Nuclear.

CUBRC Calspan-University of Buffalo Research Center.

DDT Deflagration to Detonation Transition.

EAST Electrical Arc Shock Tube.

ESA European Space agency.

ESTHER European Shock Tube for High Enthalpy Research.

FFT Fast Fourier Transform.

HVST HyperVelocity Shock Tube.

IPFN Instituto de Plasmas e Fusao Nuclear.

IST Instituto Superior Tecnico.

JAXA Japan Aerospace Exploration Agency.

LENS Large Energy National Shock-tunnel.

LES Large Eddy Simulation.

NASA National Aeronautics and Space Administration.

RANS Reynolds-averaged Navier–Stokes equations.

SPARK Software Package for Aerothermodynamics.

STAGG Shock Tube And Gas Guns.

TsAGI Central Aerohydrodynamic Institute.

Chapter 1

Introduction

1.1 Motivation

The urge to fly faster and higher is widely present in humanity's history during the 20th century and until nowadays. This motivation aligned with the fact that by the latter half of the 20th century there were rockets powerful enough to overcome the gravitational force of Earth and to reach orbital velocities, which paved the way to Space exploration. From the first launched satellite in 1957, through the Apollo missions where a total of 12 astronauts had the possibility to actually walk on the Moon [1], to the more recent rover missions on Mars, our knowledge about the Solar system and beyond is constantly growing.

But as these missions become more ambitious, the engineering challenge grows, and their success strongly depends on our ability to predict and understand the multiple environments that the vehicles will be exposed to. When a spacecraft enters an atmosphere, very high speeds are achieved, and the free stream flow forms a bow shock ahead of the forebody. In these conditions, extremely high heat fluxes, non-ideal gas behaviour, and shocks dominate the flow field, with widely complex physical phenomena that are yet to be completely understood. For example, the shock-heated gas transfers heat to the body by convection and radiation, but while convection is well understood and predictable, radiation predictions still have uncertainties larger than 30% [2].

To overcome these challenges, combined efforts with computational simulations and experimental measurements have to be done. Experimental work plays an essential role to study hypersonic flows. Experimentally, one may test a scientific hypothesis, and validate theoretical and numerical models so that these models can be used in computational fluid dynamics simulations, which can provide a good understanding of these flows once the knowledge is validated.

To validate such theories, typical wind tunnels are not suitable since the operation fundamentals of such facilities would not be able to sustain the heating rates of such flows for long periods and continuous operation is impossible for flows with such energy densities. To recreate hypersonic flows, the suitable laboratory is an impulse facility. In these facilities, a finite amount of test gas is contained inside a tube. This test gas is processed by a shock wave that will increase its temperature and pressure and also accelerate it. With these facilities it is possible to achieve supersonic and hypersonic flows, at the cost of very short test times.

Currently, the European Space Agency (ESA) is preparing exploration missions like ExoMars wherein the second phase by 2022, a rover will be sent to the surface of the red planet [3]. Such a mission is very difficult since Mars's atmosphere is very thin and hence, the sequence of entry, descent, and landing, must happen very quickly and with extreme precision. Other missions like sample-returns from Mars or even from a Near-Earth Object involve capsule return [4]. In sample-return missions, the capsule will have to make a re-entry in the Earth's atmosphere, where issues like chemical kinetics at high enthalpy, and plasma radiation are actively present. To ensure the success of such a mission, the use of an impulse facility such as a shock tube is very important, and, as a consequence, ESA has fostered the development of a new facility dedicated to such fundamental studies [5].

To support these planetary exploration missions, the European Shock Tube for high Enthalpy Research (ESTHER) is currently being developed at Instituto Superior Técnico under the funding of the European Space Agency. This state-of-the-art facility will be used to study high-speed flows that can exceed 10 km/s for super-orbital speeds.

1.2 Topic Overview

1.2.1 Atmospheric Conditions

To understand the phenomena behind the entry of a capsule through a celestial body atmosphere, it is necessary to know the conditions of that flow to recreate it. The conditions of the flow will depend on the type of mission and especially, the celestial body of destiny.

In our Solar system, all planets, with the exception of Mercury, have substantial atmospheres, including one of Saturn's natural satellites Titan. These atmospheres have different compositions, as it can be seen in table 1.1 adapted from [6], where the main components of each atmosphere are given in volume.

Table 1.1: Atmospheric compositions in volume. Adapted from [6]

	Celestial Body	Composition	
		Major	Minor
Terrestrial planets	Venus	96.5% CO_2 3.5% N_2	SO_2, Ar, H_2O
	Earth	78.08% N_2 20.95% O_2 0.9% Ar	CO_2
	Mars	95.1% CO_2 2.59% N_2 1.6% Ar 0.13% O_2	CO, H_2O, NO
Gas Giants	Jupiter	89.8±2.0% H_2 10.2±2.0% He	CH_4, NH_3
	Saturn	96.3±2.4% H_2 3.25±2.4% He	CH_4, NH_3
	Uranus	82.5±3.3% H_2 15.2±3.3% He	-
	Neptune	80.0±3.2% H_2 19.0±3.2% He	-
Natural Satellite	Titan	98.5% N_2 and 1.5% CH_4	Ar, H_2

For these celestial bodies, it is possible to use the atmosphere as a way for the spacecraft to lose energy and lower the orbit. This can be used in different manoeuvrers like aerocapture, where the aerodynamic forces that the probe is subjected to when passing through an atmosphere can be used to insert the probe in the desired orbit without the use of a propulsive manoeuvrer, or even in aerobraking where this same principle is used to lower the orbital period by dipping into the outer regions of the atmosphere during many successive orbits.

For in situ missions like rovers, landers, or even balloons, an atmospheric entry is required, where the vehicle enters an atmosphere from either a bound or unbound orbit to a fully decelerated state. The entry speed needs to be at least the corresponding escape velocity so that the probe does not fall, but not too high since the heat flux may overcome the dissipation capability of the shield, and the mission is lost.

If the atmospheric entry is done from a circular orbit, the initial entry speed is in the order of the first cosmic velocity [7], given by equation (1.1), where G is the universal gravitational constant ($G = 6.67408 \times 10^{-11} m^3 kg^{-1} s^{-2}$), m_{body} is the mass of the celestial body, and r_{body} the radius. If the entry is performed from a hyperbolic orbit, the lower value of the initial entry speed is in the order of the second cosmic velocity, which is given by equation (1.2). Hence, the initial atmospheric entry speeds, will be between these two values and be greater than u_{c2} depending on the entry orbit. In table 1.2, the calculations of the cosmic velocities with equations (1.1) and (1.2) done by Diana Luís [8] are given. These velocities were calculated considering the properties r_{body} and m_{body} from [6].

$$u_{c1} = \sqrt{\frac{G m_{body}}{r_{body}}}. \quad (1.1) \qquad\qquad u_{c2} = \sqrt{2} u_{c1}. \quad (1.2)$$

Table 1.2: Cosmic velocities. Adapted from [8]

	Celestial Body	u_{c1} (km/s)	u_{c2} (km/s)
Terrestrial planets	Venus	7.33	10.36
	Earth	7.91	11.19
	Mars	3.55	5.03
Gas Giants	Jupiter	42.14	59.60
	Saturn	25.09	35.48
	Uranus	15.06	21.29
	Neptune	16.74	23.67
Natural Satellite	Titan	1.86	2.64

From previous missions, it is possible to know the performed entry speeds for different celestial bodies. In figure 1.1, some atmospheric entries of Mars and Titan missions, and also re-entries from sample return missions to Earth, are given, with the evolution of the velocity as the altitude decreased. On the right, a different altitude axis for the entry trajectory of the Huygens mission is given.

The sample return missions of Genesis, Hayabusa and Stardust, had an initial re-entry velocity of 10.8 km/s [9], 11.7 km/s [10], and 12.9 km/s [11], respectively. For the mentioned missions to Mars, the entry velocities were lower, between a range of 4.5 km/s to 7.5 km/s [12]. In the Cassini-Huygens mission to Titan, the entry velocity is similar to the Martian ones, with a value of 6 km/s [13].

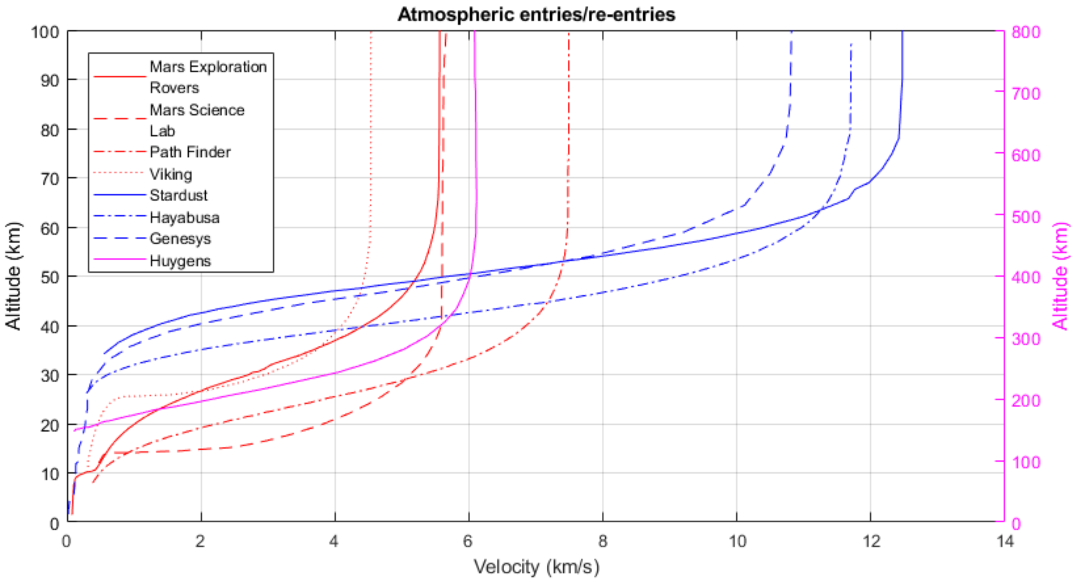

Figure 1.1: Entry and re-entry altitude versus speed. Adapted from [12] [11] [9] [10] [13]

Up to date, the only lander missions to Venus took place from the ’60s to the ’80s, and are called Venera. For the Venera 9 mission, the initial entry speed was 10.7 km/s, and for the Venera 12 and 13 missions, the entry speed was 11.2 km/s [14]. For the gas giant planets, the required entry speeds are much larger. In the Galileo mission to Jupiter, an entry speed of 47.3 km/s was recorded. For atmospheric entries in Saturn and Uranus, the required speed are around 27 km/s and 22.3 km/s, and for Neptune around 30 km/s [15] [16].

1.2.2 Impulse Facilities

An impulse facility is an experimental equipment capable of producing high enthalpy flows, with high Mach numbers for a short period of time. There are three main types of impulse facilities, shock-tubes, like ESTHER, reflected shock tunnels, and the expansion tunnels.

An example of the main performance differences of these three types of facilities is presented in table 1.3. This data was obtained from the specifications of the T6 Stalker Tunnel, a facility that can operate in these three distinct ways. With the same infrastructure, by differing some components at the end of the shock tube or by not using them at all, three very distinct performances are obtained.

1.2.2.1 Reflected Shock Tunnel

In figure 1.2 a generic scheme of a reflected shock tunnel and the respective x-t diagram is represented. Besides the typical driver conditions, in this facility the middle section referred to as the shock tube, contains the test gas at lower pressures. Separated from this section with a weak diaphragm, usually made of mylar, there is a diverging nozzle that opens up to the larger diameter test section that can contain a subscale model. Initially, the test section and the nozzle are evacuated.

Table 1.3: T6 configurations and specifications. Extracted from [17]

	Mode of operation		
	Reflected Shock Tunnel	Expansion Tunnel	Shock Tube
Testing type	Subscale model	Subscale model	Shock layer radiation
Test duration	1-3 ms	50-500 μs	2-50 μs
Flow core diameter	150-200 mm	50-120 mm	80 or 250 mm
Max flow speed	6.5 km/s	12 km/s	18 or 9 km/s

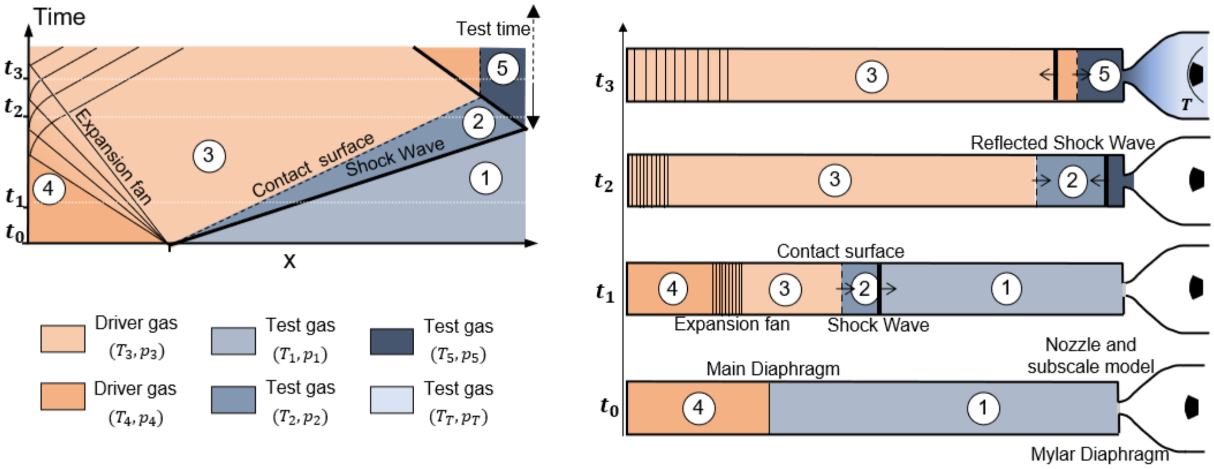

Figure 1.2: Generic scheme of a reflected shock tunnel and the respective x-t diagram.

Once the main diaphragm is ruptured, the shock wave travels through the test gas and once it reaches the end of the shock tube, it reflects on the weaker diaphragm. When the shock wave is reflected, the gas that once was heated and compressed by the moving shock is processed again and its temperature and pressure rise even more but leaving the test gas at rest. When the reflection occurs, the weaker mylar diaphragm cannot resist the extreme temperatures and disintegrates completely, and hence the test gas suffers a steady expansion through the nozzle and reaches the subscale model.

Here, the available test time will depend deeply on the interaction of the reflected shock wave with the contact surface. Their interaction has to be planned in a way that does not result in any waves. By tuning the initial driver and test gases conditions, this is possible and it is called tailored-interface operation. So, in this type of facility, the available test time will correspond approximately to the time between the first arrival of the test gas and the arrival of the driver gas when all of the test gas passes through the model.

The reflected shock tunnel is the facility that can provide longer test times, but its maximum performance is limited. To increase the performance, the driver temperature and pressure have to increase, and hence stronger shock waves can be produced. Since the test gas is brought to rest, extreme stagnation conditions can occur if the shock wave is further strengthened, but these conditions are limited by the surrounding materials that can melt if this is not taken into account. Besides this, the test gas around the model can be prematurely contaminated by the driver's gas if the tailoring is not done correctly.

1.2.2.2 Expansion Tunnel

In an expansion tunnel, at least three sections exist as can be seen in figure 1.3. Similar to the reflected shock tunnel, when the main diaphragm ruptures, the shock wave generated travels through the test gas heating, compressing, and accelerating. At the end of the shock tube, a secondary diaphragm is placed, but the shock wave instead of reflecting like in the previous facility, breaks the diaphragm and the test gas already processed by the shock waves travels to this section.

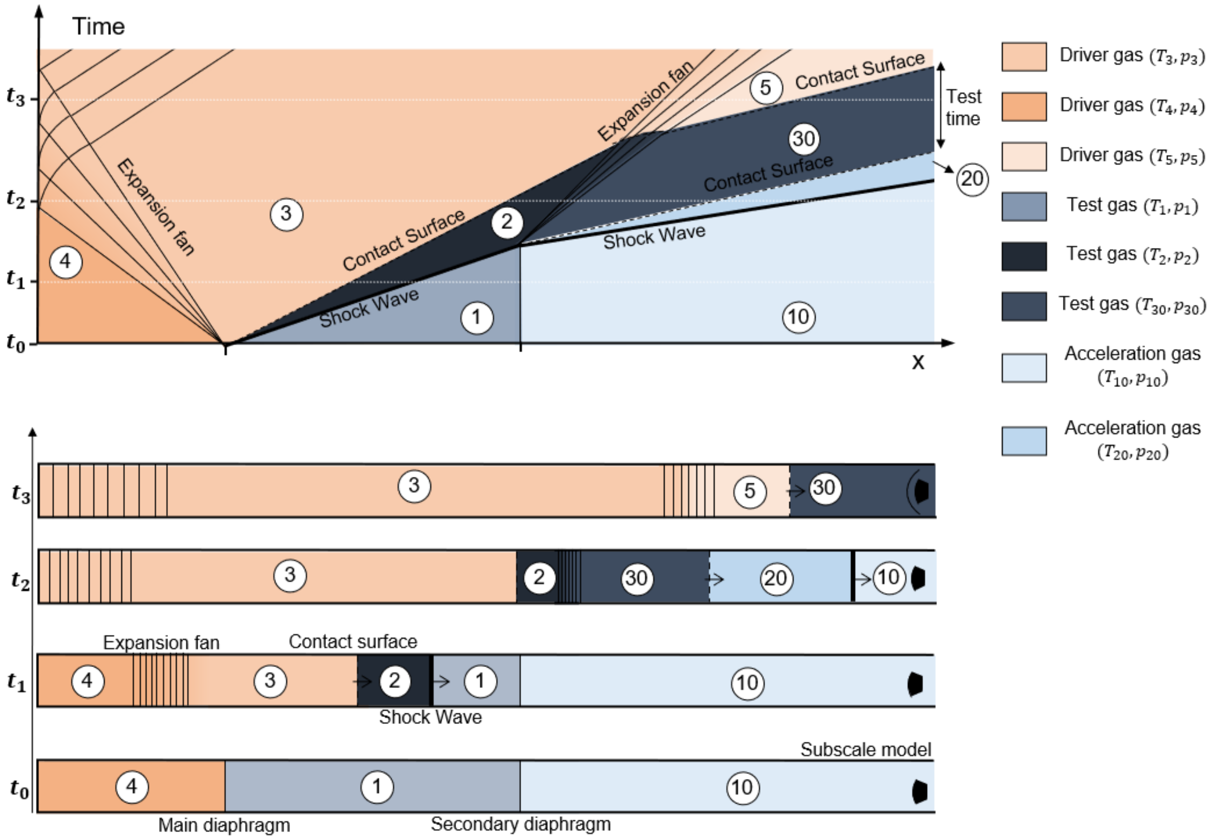

Figure 1.3: Generic scheme of an expansion tunnel and the respective x-t diagram.

This part of the facility is called the acceleration tube. It contains gas at very low pressures, and when the test gas enters it, it is exposed to practically a vacuum and it undergoes a rapid unsteady expansion and acceleration towards the test section. At the end of the expansion tube, a nozzle can be added, so that the test section has a larger core flow and hence bigger models can be used. When the front of the expanded test gas reaches the test model, the test time begins, and once all of the test gas passes through the model, the test time ends, so it is limited by the acceleration-gas test-gas contact surface, and by the leading edge of the reflection of the unsteady expansion from the driver-gas test-gas contact surface.

The expansion tunnel is mainly used for subscale models when higher flows velocities are required, but the extra performance comes at the price of much lower test times compared to the reflected shock tunnel. The reduced test time can be compensated with longer tubes, by delaying the arrival of the contact surface to the test section. The test time can also be shortened due to the secondary diaphragm opening time.

1.2.2.3 Shock Tube

A shock tube is very similar to the reflected shock tunnel. In its most simple configuration, it is composed of a driver and the shock tube but with an open-end directly connected to the dump tank (figure 2.1). Instead of studying the flow around a subscale model, the shocked test gas is the subject of study. This is done by analysing the radiating shock layer through viewing windows, and by observing the emitted spectrum one can learn about the thermochemical state of the gas flow with good detail. Although no model is being tested, with this type of experiment it is possible to validate theoretical and numerical models, and hence predict, for example, the aerodynamic forces and heating that a spacecraft is subjected to during re-entry/entry. In this facility, the test time corresponds to the difference of times between the arrival of the shock wave and the contact surface.

Since there is not a type of impulse facility that is capable of producing all the relevant flight conditions with adequate fidelity, it is very important to understand the main differences and modes of operation when choosing a facility for a specific experiment, and later interpret the results.

As it was mentioned, in a shock tube the subject of study is the shock layer radiation emission, absorption, or scattering characteristics that usually are studied with spectroscopic techniques. In a shock tube, similar to the expansion tunnel, there are also test time limitations. Another aspect that can affect the quality of the experiment is the cleanliness of the test gas sample produced behind the primary shock, which must be spectroscopically clean [18].

1.2.3 The European Shock Tube for High Enthalpy Research

Three main requirements had to be present in ESTHER, being those performance, repeatability, and availability. High performance requires the facility to achieve flows with speeds higher than 10 km/s, repeatability asks for the ability to reproduce the same condition for the test flow with precision, and availability requests a design with low turnaround times and reasonable costs per shot.

This facility is driven by a combustion driver, and it is composed of the driver section followed by the compression tube and the shock tube, and finally a dump tank (figure 2.13). The driver is one of the most important components of the shock tube since it will be one of the main performance boosters of the facility, and hence, its performance is by itself a challenge and the main focus of this thesis.

The ESTHER combustion driver was designed to operate with a combustible mixture of hydrogen and oxygen diluted with helium, inspired by the combustion driver of the Convair shock-tube [19]. The combustion can occur in two different regimes, deflagration where the combustion occurs subsonically, and detonation, where a shock wave is formed and combustion proceeds supersonically. The optimal regime to fulfill ESTHER requirements is deflagration since it is predictable and hence, repeatability can be achieved. In the detonation regime, higher compression ratios can be achieved but with low repeatability and higher stress levels on the chamber. To avoid detonations, the combustible mixture of $\mathrm{H_2}$ and $\mathrm{O_2}$ is diluted with helium since the combustion of confined pure mixtures with $\mathrm{H_2}$ and $\mathrm{O_2}$ can lead to detonations.

Before the final combustion driver, a smaller scaled model of the chamber was developed to test and improve the final design, an operation that underwent from late 2012 to early 2017 [20]. In this campaign it was possible to implement a laser ignition system, that proved to be a better source of ignition than the previous hot wire configuration, being one of the advantages more cleanliness.

1.3 Objectives

The driver of a shock tube will be one of the main sections responsible for the overall performance of the facility, and hence, it has been one of the main focus throughout the years when it comes to increasing the attainable shock speeds in ground facilities. The same applies to ESTHER, and the correct operation of the shock tube will depend strongly on the good performance of the driver, the main focus of this work.

In this work, the performance of ESTHER and more specifically, ESTHER combustion driver, will be the main focus. Besides this, a computational study of high-pressure combustion will be carried out.

The specific objectives are:

1. Study the influence that the driver conditions have on ESTHER's performance.
2. Find an appropriate set of operational points for the initial driver's gas mixture.
3. Study of high-pressure combustion of $\mathrm{He/H_2/O_2}$, and understand the influence of each initial parameter on the performance and related phenomena.
4. Computational fluid dynamics study of high pressure $\mathrm{He/H_2/O_2}$ premixed combustion.

1.4 Thesis Outline

This thesis is organized as follows:

Chapter 2 presents the shock tube theory, with the equations that govern the performance of this type of facility for single and double diaphragm configurations, and the corresponding test time. Besides this, a review of different types of drivers will be discussed. Following this section, a performance study of ESTHER will be carried out, with an emphasis on the influence that the driver conditions have on the performance.

Chapter 3 presents the combustion driver qualification campaign. Firstly, the necessary background regarding premixed combustion in confined vessels is explored, followed by the experimental set-up, results, and discussion. A parametrical study will be conducted, and the performance of the driver will be analysed.

Chapter 4 presents a CFD study of high pressure combustion of $\mathrm{He/H_2/O_2}$. The direct numerical simulations provide qualitative results of the influence that initial parameters like the composition have on the flame speed.

Chapter 5 discusses the conclusions and achievements of this work, followed by the recommendations for future work.

Chapter 2

Shock-Tube facilities background and the description of ESTHER shock tube

As the name implies, ESTHER was designed to operate as a shock tube. To fully understand the designed mode of operation of ESTHER and the existing facilities, this chapter introduces an overview of the topic with the associated theoretical background.

Firstly, ideal shock tube theory is presented, for single and double diaphragm configurations, and also different cross-sections areas. A review of different types of drivers is also presented, followed by an estimation of ESTHER performance, with a focus on different driver initial conditions.

2.1 Shock Tube Theory

A shock tube in its most simple configuration corresponds to a tube divided into two chambers separated by a diaphragm, with a finite amount of gas. In one of the chambers, a gas at high temperature and pressure is produced, and in the second chamber, a low-pressure test gas is contained. Once the diaphragm bursts due to the high-pressure differential, a shock wave is produced and travels through the test gas, raising its temperature and pressure and accelerating it. The regions initially at high and low pressure are designated as the driver and driven sections, respectively.

This working principle can be observed in figure 2.1, where a simple scheme of a shock tube is presented at multiple representative instants.

The instant t_0 corresponds to the moment before the bursting of the diaphragm, with region 4 being the driver gas at high temperature and pressure (p_4, T_4) and region 1 the test gas at low pressure and temperature (p_1, T_1).

The instant t_1 occurs right after the diaphragm is opened. Once the moving shock wave is generated, it compresses and heats the test gas creating region 2, and this induces a mass movement in this region towards the right with velocity u_2. Besides the moving shock wave, an expansion also takes place after the diaphragm opens, expanding the driver gas from region 4 to region 3. Between regions 2 and 3, a contact surface that separates the two different gases exists. This surface travels towards the right with a velocity equal to region 2. Across this slip line, the velocities and pressures are continuous, so that $p_3 = p_2$ and $u_3 = u_2$.

The flow of interest during the experience corresponds to region number 2. So, the available test time will correspond to the difference of times between the arrival of the shock wave and the contact surface to the test location, located at the x_{test} coordinate. The instant t_2 corresponds to the arrival of the shock wave, and the instant t_3 corresponds to the arrival of the contact surface to the x_{test} location. Therefore, the difference between these two moments will correspond to the test time.

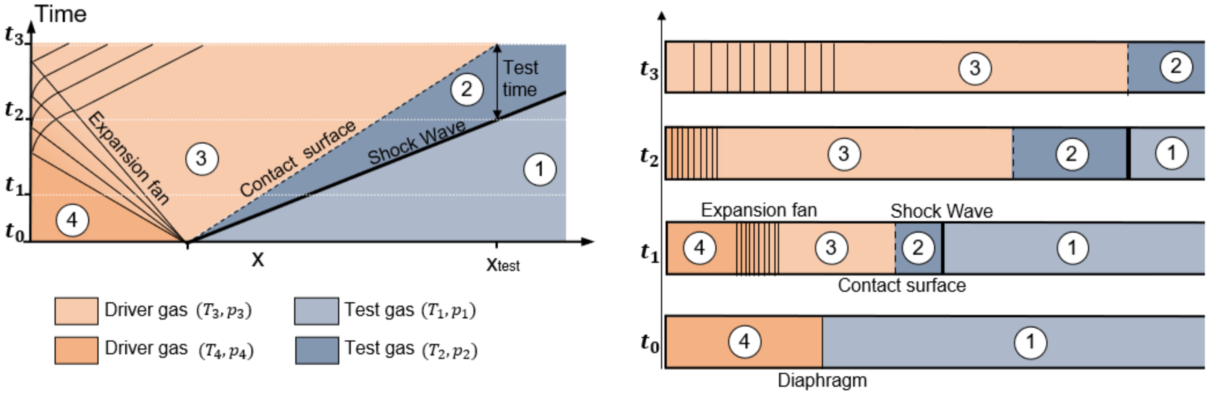

Figure 2.1: Shock tube scheme with x-t diagram.

Operationally speaking, the imposed properties are the initial conditions and gases in regions 1 and 4, although these can have limitations depending on the type of driver and facility. So, to test the conditions of interest in region 2, one should model the flow and try to mathematically reproduce the physical evolution of this facility.

2.1.1 Single diaphragm shock tube with uniform section

As a first approach, the ideal shock tube theory will be presented, where the flow is assumed to be inviscid, calorically perfect, and modelled in 1D.

By making an energy, momentum, and continuity balance across the moving shock wave, equation A.1 to A.3, it is possible to get the *Hugoniot equation* (2.1), that relates the changes of thermodynamic variables across a normal shock wave.

$$e_2 - e_1 = \frac{p_1 + p_2}{2}\left(u_1 - u_2\right). \tag{2.1}$$

From equation (2.1) and assuming a calorically perfect gas $e = c_v T$ and $v = RT/p$, it is possible to obtain the temperature ratio across the moving shock wave, given by equation (2.2).

$$\frac{T_2}{T_1} = \frac{p_2}{p_1}\left(\frac{\frac{\gamma_1+1}{\gamma_1-1} + \frac{p_2}{p_1}}{1 + \frac{\gamma_1+1}{\gamma-1}\frac{p_2}{p_1}}\right). \tag{2.2}$$

Incorporating the definition of the shock wave Mach number $M_s = u_s/a_1$ through the equations of energy, momentum, and continuity, and the calorically perfect gas equations, we can obtain the shock wave velocity, given by equation (2.3).

$$u_s = a_1\sqrt{\frac{\gamma_1+1}{2\gamma_1}\left(\frac{p_2}{p_1}-1\right)+1}. \tag{2.3}$$

The shock induces a mass movement in region 2. From equation A.1, and incorporating equations (2.3) and (2.2), the velocity in region 3 and hence, region 2, is obtained and given by (2.4).

$$u_2 = \frac{a_1}{\gamma_1}\left(\frac{p_2}{p_1}-1\right)\left(\frac{\frac{2\gamma_1}{\gamma_1+1}}{\frac{p_3}{p_1}+\frac{\gamma_1-1}{\gamma_1+1}}\right)^{\frac{1}{2}}. \tag{2.4}$$

From the characteristics method, one may find an expression that relates the pressure ratio across the expansion wave and the local velocity, given by equation (2.5).

$$\frac{p_3}{p_4} = \left[1-\frac{\gamma_4-1}{2}\frac{u_3}{a_4}\right]^{\frac{2\gamma_4}{\gamma_4-1}}. \tag{2.5}$$

Remembering the fact that u_3=u_2 and $p_3 = p_2$, by rearranging equations (2.5) and (2.4), the equation that relates the known initial pressure ratio p_4/p_1 to the unknown p_2/p_1 is given by 2.6

$$\frac{p_4}{p_1} = \frac{p_2}{p_1}\left\{1-\frac{(\gamma_4-1)\left(\frac{a_1}{a_4}\right)\left(\frac{p_2}{p_1}-1\right)}{\sqrt{2\gamma_1\left[2\gamma_1+(\gamma_1+1)\left(\frac{p_2}{p_1}-1\right)\right]}}\right\}^{-\frac{2\gamma_4}{\gamma_4-1}} \tag{2.6}$$

Although the inspection of the relation between the properties of equation 2.6 is not straightforward because the shock strength p_2/p_1 is expressed implicitly, it is possible to make some conclusions from it. For a given pressure ratio p_4/p_1, the shock strength, represented by the pressure ratio p_2/p_1, will be bigger as the sound of speed ratio a_1/a_4 is made lower. So, to maximize the shock strength, the driver gas should have a big sound speed velocity, and the test gas a lower one. The speed of sound is defined as $a = \sqrt{\gamma R T}$, so if the specific gas constant (R) and temperature (T) are high, the speed of sound will be high. Hence, if we want to increase the shock strength, hot low molecular weight gases are used in the driver and cold high molecular weight gases in the test section. But since the test gas has a specific composition and requirements for the experience, the driver gas properties and composition are some of the main factors that contribute to the increase of performance of the shock tube.

2.1.2 Single diaphragm shock tube with cross section area reduction

The use of a non-uniform section in the diaphragm region can bring several benefits when compared with a simple uniform tube.

Represented in figure 2.2, a shock tube with a non-unitary area ratio between the driven and driver sections is presented, with a simple convergent connection between them. Once the diaphragm bursts, an unsteady expansion wave propagates towards the left, between regions 3a and 4, and between regions 3a and 3b in the convergent nozzle, a steady expansion occurs. Following the steady expansion in the nozzle, in section 3b the flow can either be subsonic or sonic. If the velocity is subsonic, in region 3 ($M_3 < 1$) and the flow is uniform. If the sonic condition in section 3b is achieved, the flow endures an unsteady supersonic expansion towards region 3.

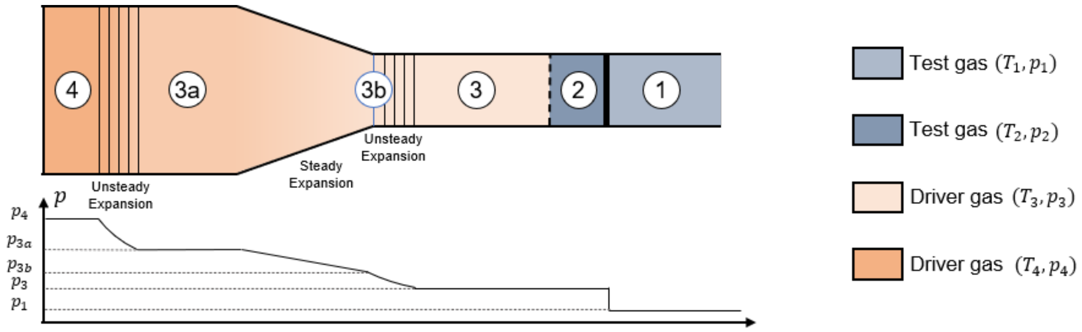

Figure 2.2: Shock tube with area change in the diaphragm section. Adapted from Alpher and White [21].

So, to obtain the pressure ratio p_4/p_1, one has to take into account the referred phenomena according to equation (2.7), where p_4/p_{3a} is the pressure ratio across the unsteady expansion wave, p_{3a}/p_{3b} is the pressure ratio across the steady nozzle flow, p_{3b}/p_3 is the pressure ratio across the unsteady expansion wave, p_3/p_2 is equal to one as it was previously mentioned and p_2/p_1 is the pressure ratio across the shock wave.

$$\frac{p_4}{p_1} = \frac{p_4}{p_{3a}} \frac{p_{3a}}{p_{3b}} \frac{p_{3b}}{p_3} \frac{p_3}{p_2} \frac{p_2}{p_1}, \tag{2.7}$$

Using the equations (A.5) and (A.4), we can rewrite the equation (2.7) and it is given by (2.8).

$$\frac{p_4}{p_1} = \left\{ \left[1 + \frac{\gamma_4 - 1}{2} M_{3a} \right] \left[\frac{2 + (\gamma_4 - 1) M_{3b}^2}{2 + (\gamma_4 - 1) M_{3a}^2} \right]^{1/2} \left[\frac{2 + (\gamma_4 - 1) M_3}{2 + (\gamma_4 - 1) M_{3b}} \right] \right\}^{\frac{2\gamma_4}{\gamma_4 - 1}} \frac{p_2}{p_1}. \tag{2.8}$$

Using further equations that relate the Mach number in the different regions and the area ratio A_4/A_1, the pressure ratio p_4/p_1 can be finally written by equation (2.10), where quantity g is called equivalence factor and is given by equation (2.9).

$$g = \left\{ \left[\frac{2 + (\gamma_4 - 1) M_{3a}^2)}{2 + (\gamma_4 - 1) M_{3b}^2} \right]^{\frac{1}{2}} \left[\frac{2 + (\gamma_4 - 1) M_{3b}}{2 + (\gamma_4 - 1) M_{3a}} \right] \right\}^{\frac{2\gamma_4}{\gamma_4 - 1}}, \tag{2.9}$$

$$\frac{p_4}{p_1} = \frac{1}{g} \frac{p_2}{p_1} \left[1 - \frac{u_2}{a_1} \frac{a_1}{a_4} \frac{\gamma_4 + 1}{2} g^{\frac{1 - \gamma_4}{2\gamma_4}} \right]^{-2\gamma_4(\gamma_4 - 1))}. \tag{2.10}$$

Within this configuration, the main advantage is related to the velocity increase that the extra forced expansion due to the area ratio can provide. Since for unsteady expansions $du/dp = -1/(\rho a)$, and for steady expansions $du/dp = -1/(\rho u)$, the ratio $(du/dp)_{unsteady}/(du/dp)_{steady} = M$, for a given pressure drop, the velocity gain is bigger for steady subsonic expansion or unsteady supersonic expansion. With this technique, a higher driver performance can be obtained at the expense of increased driver volume. For the same shock Mach number, a smaller pressure ratio p_4/p_1 is required.

2.1.3 Double diaphragm shock tube with cross section area reduction

In the most simple configuration, with two sections with the same cross-section and the same gas, the shock tube can not produce flows with high Mach numbers. Assuming a perfect gas, and the scenario of theoretical infinite pressure ratio (p_4/p_1), the shock Mach number is limited by 2.11, that for a $\gamma = 1.4$ is gives $Ms < 6.16$.

$$M_s < \frac{\gamma+1}{2(\gamma-1)} + \sqrt{1 + \left[\frac{\gamma+1}{2(\gamma-1)}\right]^2}. \tag{2.11}$$

One of the ways to increase the facility performance is by adding a third section, called the compression tube. With this configuration, the facility will be composed by the driver, followed by the compression tube, with the first diaphragm separating the two sections, and finally the shock tube that comprises the test section, with a second diaphragm between the two last sections.

After the bursting of the first diaphragm, a primary shock wave is produced and travels through the intermediate gas, heating it and increasing the pressure. Once this shock wave reaches the second diaphragm, if we assume that the diaphragm is weak, it will disintegrate almost instantly, and the main shock wave is produced and travels through the test gas. With this technique, for the same pressure ratio between the driver and the shock tube, a greater shock velocity can be obtained.

The area cross-section change may also provide extra performance to the shock tube. So, by conjugating these two performance enhancement techniques, the flow velocity can be even greater. In figure 2.3, a double diaphragm shock tube with area reduction in both diaphragm sections is presented. Two representative moments are schematized. The first corresponds to the time after the bursting of the first diaphragm, and another image to the disintegration of the second diaphragm, where regions 9 and 4 correspond to the conditions in the indicated sections in figure 2.3.

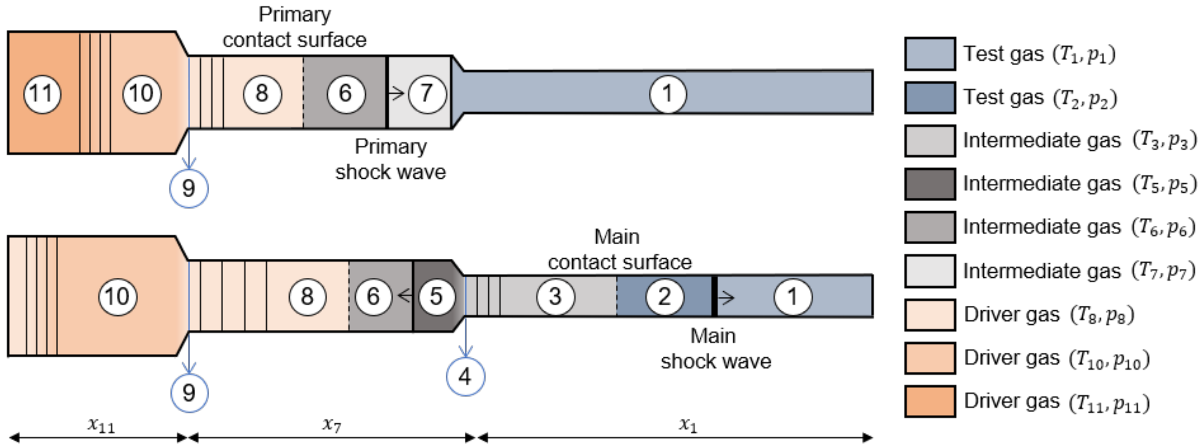

Figure 2.3: Shock tube with three sections with different cross section areas.

To understand the performance of a shock tube with this type of configuration, firstly regions 11 through 3 are considered. So, the pressure ratio p_{11}/p_3 necessary to obtain the velocity ratio u_3/a_7 will be derived. It was assumed that the second diaphragm is sufficiently weak so that it bursts when the primary shock wave hits it. Since in this analysis we are interested in the generation of strong shocks, they are assumed to be strong enough that in regions 3 and 8 the flow is supersonic and the primary shock reflects in the second area reduction as a shock ($M_6 \geq M_5$). A steady acceleration to the sonic speed in the cross-section area reduction is assumed to occur as an isentropic process. Another assumption of the following equations is that no liquefaction of gas can occur in any region of the flow.

The pressure ratio p_{11}/p_3 necessary to obtain a given velocity ratio u_3/a_7 is given by equation (2.12), where p_{11}/p_8 is given by (A.6), $p_8/p_6 = 1$, p_6/p_5 is given by (A.9), p_5/p_4 is given by (A.14), and p_4/p_3 is given by (A.15). The mentioned equations are deduced in appendix A, section A.3.

$$\frac{p_{11}}{p_3} = \frac{p_1 1}{p_8}\frac{p_8}{p_6}\frac{p_6}{p_5}\frac{p_5}{p_4}\frac{p_4}{p_3}. \tag{2.12}$$

One of the variables that the pressure ratio p_{11}/p_3 depends on is the Mach number of the primary shock wave, M_{s7}. This variable is of particular interest and can be simply calculated with equation (2.13), where p_6/p_7 is given by equation (A.21).

$$\frac{p_{11}}{p_7} = \frac{p_{11}}{p_8}\frac{p_8}{p_6}\frac{p_6}{p_7}. \tag{2.13}$$

Nevertheless, the value of the primary shock Mach number may be optimized. For a given u_3/a_7, it is of interest that the pressure ratio p_{11}/p_3 is as small as possible, or even that for a given p_{11}/p_3, u_3/a_7 is maximized. Considering the first statement, the optimal M_{s7} can be translated into equation (2.14).

$$\frac{\partial}{\partial M_{s7}}\left(\ln\frac{p_{11}}{p_3}\right) = 0 \tag{2.14}$$

Equation (2.14) is further developed in appendix A, section A.3. Using equations (A.22) to (A.30), it is possible to calculate for any given M_{s7}, the value of u_3/a_7 for which that value of M_{s7} is optimum.

Summing up, for a desired test flow velocity in region 2, and since $u_3 = u_2$ and $p_3 = p_2$, one calculates the pressure ratio p_{11}/p_3 with, or not, the optimal value of M_{s7}.

Although the analysis of the presented equations is not as straightforward as in section 2.1.1 with the most simple configuration of the shock tube, the same behaviour occurs. As the driver's pressure and sound velocity increase, the shock tube performance is also increased, as will be showed in section 2.3.3.

2.1.3.1 Dimensions

In a double diaphragm shock tube with cross section reductions, several physical disturbances like shock waves and unsteady expansions are generated. If the facility is not correctly dimensioned, these disturbances may easily reflect in the walls and disturb the test flow in region 2 (see figure 2.3). Thus, to have a good test flow, the sections must have some dimensional constraints.

Firstly, considering x_{11} and x_7, the head of the expansion wave, reflected from the end of the driver section, must not overtake the primary contact surface before it intersects with the shock reflected from the second diaphragm. Considering this condition, the ratio x_{11}/x_7 can be expressed in terms of x_{test} and M_{s7} in equation (2.15), where the variable x_{test} is defined as the distance between the second diaphragm and the test section in the shock tube, and determines the useful quasi-steady flow duration.

$$\left(\frac{x_{11}}{x_7}\right)_{\min} = \left(\frac{M_{10}+1}{4}\right)\frac{a_{11}}{a_7}\left(\frac{1+\frac{U_R}{M_{87}a_7}}{X^{\frac{a_6}{a_7}}}\right)\left\{\frac{\gamma_{11}+1}{k\left[(\gamma_{11}-1)\,M_{10}+2\right]}\left[k-\frac{\gamma_{11}-1}{\gamma_7+1}\frac{a_7}{a_{11}}\left(M_{s7}-\frac{1}{M_{s7}}\right)\right]\right\}^{\frac{\gamma_{11}+1}{2(\gamma_{11}-1)}}. \tag{2.15}$$

The ratio U_R/a_7 is given by equation (2.16).

$$\frac{U_R}{a_7} = \frac{u_6}{a_7}\left(\frac{X}{M_6}-1\right). \tag{2.16}$$

Secondly, the wave generated at the intersection of the primary contact surface with the shock reflected from the second diaphragm must not overtake the main contact surface before the test section. This condition yields the minimum value of $(x_7/x_{test})_{min}$, and may be translated into equation (2.17), where it was assumed that the wave generated at the intersection of the primary contact surface with the shock reflected from the second area reduction behaves like a characteristic line, and considering the quantities calculated in A.3.

$$\left(\frac{x_7}{x_{\text{test}}}\right)_{min} = \frac{1}{2\frac{u_3}{a_7}\phi}\left(\frac{\gamma_7+1}{2}-\frac{\gamma_7-1}{2}\frac{\frac{u_3}{a_7}}{\frac{a_4}{a_7}}\right)^{\frac{\gamma_7+1}{2(\gamma_7-1)}} \tag{2.17}$$

The variable ϕ is given by equation (2.18).

$$\phi = \frac{\gamma_7-1}{\gamma_7+1}\frac{\left[1+\frac{2}{(\gamma_7-1)M_{s7}^2}\right]}{X^{\frac{a_6}{a_7}}}\left[1+\frac{\frac{U_R}{a_7}}{(1+M_5)\,\frac{a_5}{a_6}\frac{a_6}{a_7}}\right] \tag{2.18}$$

2.1.4 Test time

In the previous sections, the effects of viscosity, finite diaphragm bursting time, heat losses, and flow non-uniformities were neglected. Although this approach may predict results close to reality at moderate velocities and high test gas densities, for experiments that represent interesting hypersonic points, with higher velocities, non-ideal effects have a significant impact on the shock tube operation.

In a shock tube, the test time is the difference in time between the arrival of the shock and the arrival of the contact surface at the test coordinate, x_{test}. In an ideal shock tube, this time depends on the shock tube length, since it is assumed that the shock and contact surface move with constant velocity and that the flow between them is uniform, neglecting the viscous effects. But in reality, a shock layer develops between the contact surface and the shock wave.

The presence of a boundary layer in regions 3 and 2 acts like an aerodynamic sink, removing mass in this region and causing the shock wave to de-accelerate ($u_{s_{ideal}} > u_{s_{real}}$) and the contact surface to accelerate ($u_{c_{ideal}} < u_{c_{real}}$). Since the shock wave and contact surface get closer, the real test time decreases. This effect increases as the length to diameter ratio of a shock tube increases and as the initial pressure in the low-pressure section is reduced.

However this scenario does not develop indefinitely. When the mass flow through the shock equals the boundary layer flow past the contact surface, the shock and the contact surface start moving with constant and equal velocities, and hence, the test time tends to a constant value, even if the shock tube length is increased.

In figure 2.4, this phenomena is represented with a x-t diagram and the respective shock tube view at a representative instant t_1. The flow between the contact surface and shock wave is not uniform and the discontinuity between the two gases is closer to a ”U” shape. In the x-t diagram, the slope of the shock wave and contact surface lines is no longer constant.

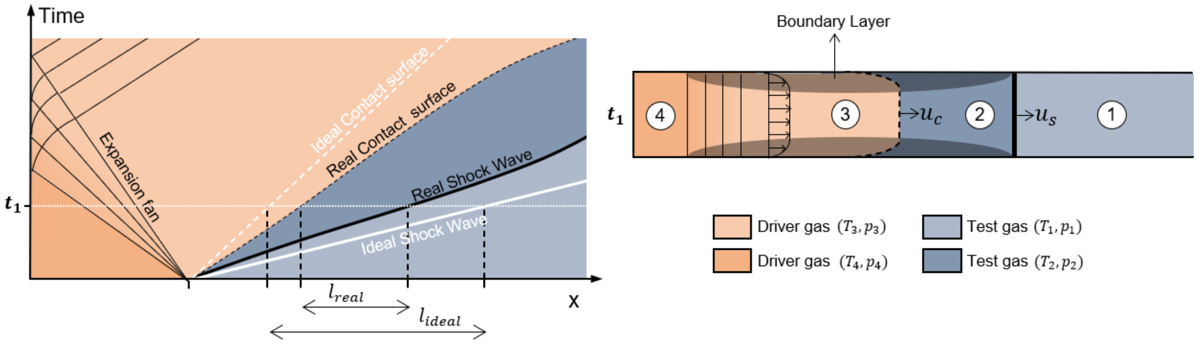

Figure 2.4: Simple shock tube with real contact surface and shock.

In Mirels work [22], a theory to solve the problem of test times in low-density shock tube is presented. In this theory the shock wave is considered to move with uniform velocity and the coordinate system used puts the shock stationary and the wall moving with velocity $u_w = u_s$. Previous works from Roshko [23] and Hooker [24] also studied this, but using a contact surface fixed coordinate system.

The non-uniform flow between the shock wave and the contact surface is considered, because of the existence of a boundary layer. The boundary layer is assumed to be laminar, an assumption generally valid for low-pressure shock tubes. This theory has better results with shocks of moderate and high strengths.

In the mentioned works, the approach to find an expression for the test time starts with the calculation of the distance between the shock wave and the contact surface, defined as l_m. Firstly, one may calculate the mass flow through the shock wave, that is given by equation (2.19), where A is the shock tube cross-section area, the subscript e corresponds to the free stream conditions between the shock and the contact surface, and subscript 0 to the conditions right after the shock.

$$\dot{m}_s = (\rho_e u_e)_0 A. \tag{2.19}$$

Secondly, one calculates the mass flow through the contact surface. If one assumes that the shock tube is long enough for the asymptotic behaviour of the shock wave moving with the same velocity of the contact surface to occur, and using the mentioned coordinate system that is represented in figure 2.5, there is only mass flow in the boundary layer region. If we consider a thin boundary layer ($\delta_R <<$Tube diameter), the mass flow in the contact surface is given by equation (2.20), where L is the perimeter of the tube, δ_R is the boundary layer thickness at l_m and $\rho_{w,0}$ and $u_w - u_{e,0}$ are characteristic boundary layer densities and velocities respectively.

$$\dot{m}_e = L\rho_{w,0}(u_w - u_{e,0})\delta_R. \tag{2.20}$$

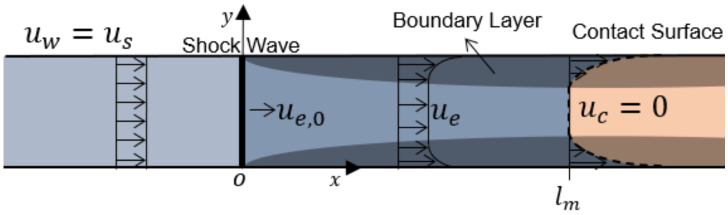

Figure 2.5: Boundary layer development inside shock tube.

The boundary layer thickness is given by equation (2.21), where β is a constant that has to be calculated from the exact solution of the boundary layer development in the tube.

$$\delta_R = \beta \left(\frac{\nu_{w,0} l_m}{u_w - u_{e,0}} \right)^{1/2}. \tag{2.21}$$

By equating equations (2.19), (2.20) and (2.21), the distance l_m is given by (2.22), where $d = 4A/L$ is the hydraulic diameter..

$$l_m = \frac{d^2}{16\beta^2} \left(\frac{\rho_{e,0}}{\rho_{w,0}} \right)^2 \frac{u_{e,0}}{u_w - u_{e,0}} \frac{u_{e,0}}{\nu_{w,0}}. \tag{2.22}$$

In Mirels work [22], one of the main focuses was to improve the estimations of the parameter β, especially for moderate shocks. This was done by using equation 2.22 to define β, to determine l_m as accurately as possible.

Firstly, Mirels assumed that the boundary layer was produced due to a uniform external stream. For this scenario, β is referred to as β_0 with the subscript 0 to distinguish the different approaches to calculate this parameter.

Numerical values of β_0 where computed assuming an ideal gas and $\rho\mu = const.$ in the boundary layer. Afterwards, these values were correlated, within 2%, and this correlation is given by 2.23, where $C_{e,0}^{0.37}$ is correction factor of the constant $\rho\mu$. When the shock is considered to be ideal, $Z = (\gamma+1)/(\gamma-1)$, but for a strong non-ideal shock, Z is replaced by W, that is given by $W = u_w/u_{e,0}$.

$$\frac{\beta_0}{C_{e,0}^{0.37}} = 1.135 \left(\frac{2(W-1)}{1+1.022W} \right)^{1/2} \left(1 + \frac{1.328 + 0.890W}{ZW - 1} \right) \tag{2.23}$$

Once the parameter β_0 is found, the value of l_m can be calculated, and the length of the useful flow may be known. However it was found that the values of β_0 were too small compared with real values and hence, l_m was overestimated. Hence, to obtain a more accurate estimate of β, the variation of the free stream was taken into account.

In this approach, the concept of local similarity is used. It is assumed that the boundary layer profile at each l corresponds to one associated with a uniform free stream and a wall velocity u_w, and that the boundary layer growth at each section is the same as the corresponding uniform free stream boundary layer.

For this concept, β is referred to as β_1, and can be calculated with a numeric integration along l of a non-dimensional constant that characterizes $\bar{\delta}$, the ratio of the excess mass flow through the boundary layer. Once the relevant calculations are made, the correlation may be obtained and is given by equation (2.24), where $C_{e,0}^{0.37}$ is correction factor of the constant $\rho\mu$. When the shock is considered to be ideal, $Z = (\gamma+1)/(\gamma-1)$, but for a strong non-ideal shock, Z is replaced by W.

$$\frac{\beta_1}{C_{e,0}^{0.37}} = 1.59\left(1 + \frac{1.796 + 0.802W}{ZW - 1}\right). \tag{2.24}$$

Once the value of β is obtained, the calculation of l_m is straightforward with equation 2.22. If we consider that the shock tube is sufficiently long to permit the asymptotic steady-state flow to be reached, the length of the useful test flow is in fact l_m, and the test time is simply given by equation 2.25.

$$\tau = \frac{l_m}{u_w}. \tag{2.25}$$

However to calculate the test time in situations where the flow hasn't reached this asymptotic state, one must know the separation distance l as a function of t.

To do so, it is assumed that the shock moves with constant velocity u_s and the same shock fixed coordinates in figure 2.5. The flow in regions 2 and 3 is assumed to be in steady state at each instant, but with the contact surface getting closer to the shock, at distant l from the shock, that decreases over time. Thus, t and l are related by $t = \int_0^l dl/u_s$.

By introducing the quantities X and T given by equations (2.26a) and (2.26b) respectively, one may measure the wall boundary layer effect, which is stronger the further these two quantities move apart, and for inviscid flows $X = T$.

$$X = \frac{u_{e,0}t}{l_m}. \tag{2.26a}$$

$$T = \frac{l}{l_m}. \tag{2.26b}$$

Using an expression that characterises the ratio of the excess mass flow through the boundary layer($\bar{\delta}$) at l, the equation (2.27) that relates X and T and hence, characterizes l along t.

$$-\frac{1}{2}X = ln(1 - T^{\frac{1}{2}}) + T^{\frac{1}{2}}. \tag{2.27}$$

Now that we have the general expression that relates X and T, one may get the final expression to calculate the test time, τ. If we define $\bar{\tau} = u_s\tau/l_m$, which is the test time at x divided by the test time when $l = l_m$, using equation (2.27), the relation between X and $\bar{\tau}$ is given by equation (2.28).

$$-X = 2\left[ln(1 - \bar{\tau}^{\frac{1}{2}}) + \bar{\tau}^{\frac{1}{2}}\right] + \frac{\bar{\tau}}{W} \tag{2.28}$$

2.2 Drivers

The configuration and design of the shock tube's driver is one of the key aspects to take into account when defining the shock tube's performance goal. It has been shown that aspects like the geometry, the pressure ratio between the driver and driven sections, the driver's mixture of gases, and temperature have a significant influence on the main shock wave speed.

Since shock-tubes were first developed to study high-speed flow phenomena, the driver's configuration was one of the main focuses when trying to increase the main shock wave speed. The goal over the years was to increase the driver's speed of sound by increasing the temperature and using lighter gases.

Theoretically speaking, it is understandable that these aspects play a significant role, but the implementation of a configuration that can fulfill the requirements can be tricky and it has evolved over the years. Depending on the type of shock tube, the driver configuration can vary. For super-orbital facilities like ESTHER, the driver must have a very high performance in terms of temperature and pressure. Since the main focus of this thesis is about ESTHER's high-performance driver, a list of some types of drivers from facilities with high performances is going to be given next.

2.2.1 Free piston driver

One of the configurations widely used for the driver section is the free piston scheme, firstly developed by Stalker in 1961 [25] [26]. In this configuration, there is a high-pressure room-temperature reservoir that induces movement in a heavy piston. With the movement of this piston, the compression tube that is usually filled with helium/argon starts to be compressed. When the peak pressure is about to be achieved, the diaphragm bursts, and a shock wave is transmitted to the next section's gas [27]. The driver gas that firstly was at room temperature and low pressure now has temperatures in the range of 1500K to 7000K and pressures up to 120 times bigger than its first state. Although this process has heat losses that reduce the achieved temperature, it is close to an isentropic compression.

A free-piston driver is advantageous for the mechanical and thermal constraints. Since the compression is transient, the compression tube is under high stresses for a very short period of time, reducing the mechanical and thermal stresses.

In this type of configuration, a detailed analysis of the piston movement and mass is crucial to understand the driver's structural limits and also predict the pressure, with piston speeds of the order of hundreds of meters per second required. If the piston speed is maintained after the rupture of the first diaphragm, the test time can be increased because the arrival of the unsteady expansion wave can be delayed by maintaining the driver's pressure approximately constant. There's also a large area change at the primary diaphragm that allows a stronger shock wave to be developed.

Some of these types of facilities are at the expansion tubes located at the University of Queensland in Australia, that currently has two super-orbital facilities, X2 and X3.

Commissioned in 1995, the X2 free-piston-driven expansion tube was first developed to test concepts and configurations for the larger X3 tube that was afterward commissioned in 2001 [28]. One of the initial characteristics of this facility was the fact that instead of a single piston, a compound piston was used. This type of piston consisted of a light outer piston and a heavier inner piston where, after an initial compression, the inner one would separate from the outer one and continued the driver's gas compression through a smaller diameter tube, making this configuration less expensive than if the driver had a constant diameter. Afterward, this configuration was converted to a single-piston driver [5].

This facility is a two diaphragm shock tunnel that can be used as an expansion tube or a shock tube. Figure 2.6 presents a scheme of X2 expansion tube with the corresponding dimensions. With a total length of 23 m including the high-pressure reservoir and driver, X2 can reach a shock wave velocity of 10.3km/s and test times of 50 ms with the configuration of an expansion tube [5]. X2 has been used to investigate radiation phenomena, scramjet testing, ablation-radiation coupling over carbonaceous test models, and the flow over a toroidal ballute.

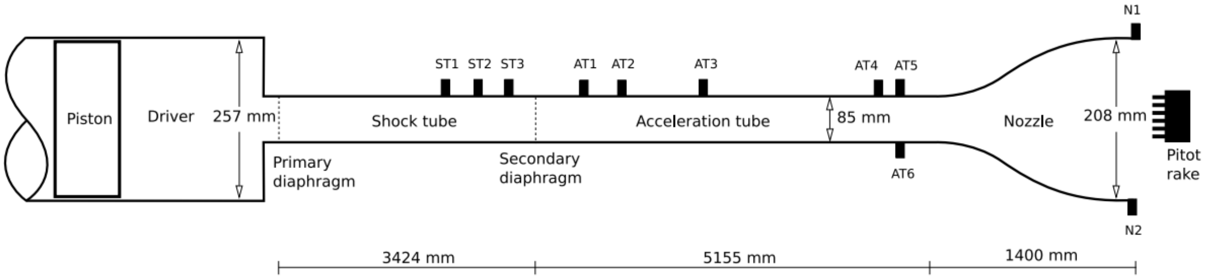

Figure 2.6: Scheme of the X2 expansion tube with dimensions. Taken from Potter et al. [29].

The X3 tube, shown in figure 2.7, is much longer than the X2, with a total length of 69 m and wider sections, that bring benefits like a larger test slug length and increased test section. Hence, bigger models can be tested [28].

Similar to the X2's initial driver, X3 had a compound piston that due to its operation complexity triggered the mentioned conversion of X2 to a single-stage piston since this was its prototype. In 2004 when the funds became available, X3 was converted to a single-stage piston and proved to have a big performance enhancement [30]. Unlike X2, this expansion tube has not been widely used for experiences investigating radiation and high enthalpy flows, it has been going thorough a period of upgrades [31].

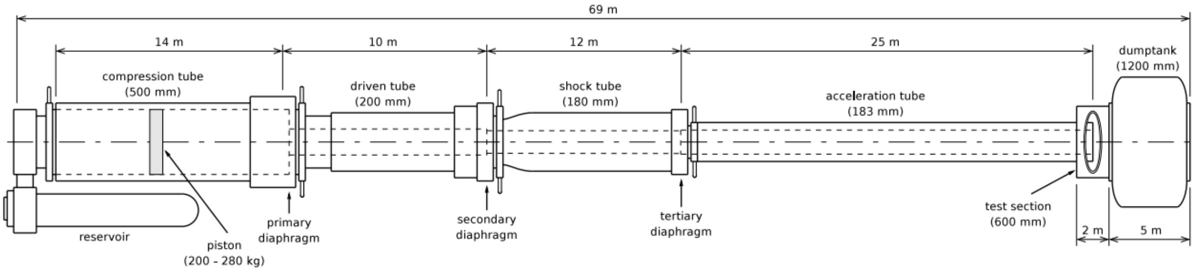

Figure 2.7: Scheme of the X3 expansion tube with dimensions. Taken from Morgan et al. [32].

Represented in figure 2.8 is HVST, the Hyper Velocity Shock Tube. This facility, located in Japan, belongs to JAXA, the Japan Aerospace Exploration Agency. It is a double diaphragm shock-tube with approximately 23 m length and is composed of the reservoir and compression tube that behaves as the driver, the high-pressure tube, and the low-pressure tube with a square profile where the test section of 70x70 mm is located. HVST can reach a shock wave speed of 15 km/s with a pressure of 13 bar in the test section [33].

The main researches developed in HVST are about non-equilibrium phenomena behind the shock wave and the emitted radiation that is later decomposed by a spectrometer. Depending on the subject/atmosphere of study, the composition of the test gas can vary. The facility t was used to investigate the re-entry trajectory of the Hayabusa mission [34] [35].

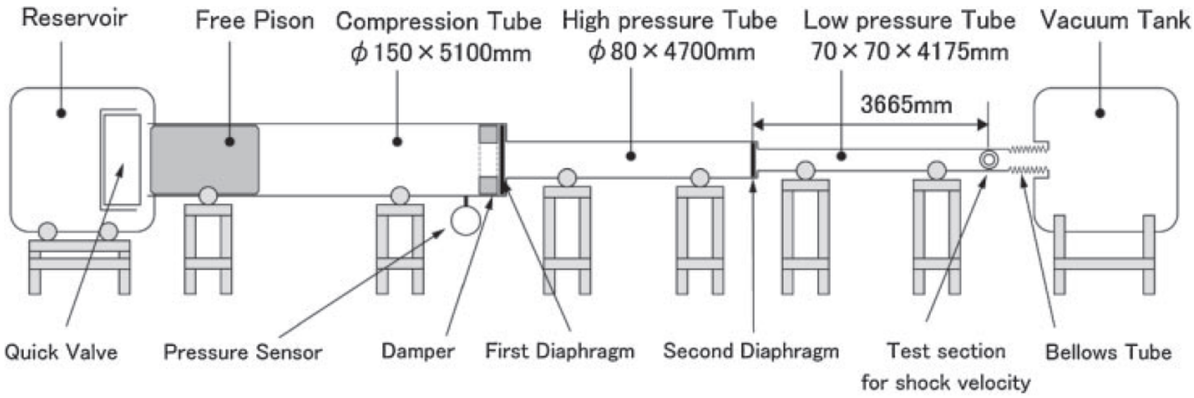

Figure 2.8: Scheme of the HVST with dimensions. Taken from Yamada et al. [36].

The next facility is called T6, a multi-mode tunnel developed by the Osney Thermo-Fluids Laboratory at the University of Oxford (United Kingdom) in collaboration with the Centre for Hypersonics from the University of Queensland (Australia). From all of the free-piston driver facilities presented, T6 is the only one that can operate in three modes, as reflected shock tunnel, as an expansion tunnel, for the generation of super-orbital flow conditions, and also as a shock tube, for examining shock layer radiation phenomena.

This facility's driver was from the decommissioned T3 Australian shock-tube, designed by Prof. Ray Stalker, the inventor of this type of mechanism. Besides the driver, some components like a nozzle and the test section were reused from the Oxford Gun Tunnel.

Shown in figure 2.9, T6 has approximately 16 m of length, including the high-pressure reservoir, and a third diaphragm, used as a reflected shock tunnel whenever needed. Similar to HVST, the test section is not circular, with dimensions of 610 x 608 mm.

This type of driver can provide very good performance to the facility, but caution must be taken when considering the compression time. Although the compression occurs in small periods of time, temperatures up to 3000 K can be reached, and if the process takes too long, the materials of the driver can start to melt and ablate [38].

2.2.2 Electric heated driver

LENS XX is an expansion tube designed and constructed by CUBRC, an American research and development company located in Buffalo, after the successful prototype LENS X. The construction of this facility was concluded in 2009 and it is the longest expansion tunnel in the world with a length of approximately of 73 m, a test section of 0.6 m or 2.4 m of diameter after the nozzle, depending on the type of experiment, and as it can be seen in figure 2.10.

This facility driver is electrically heated and is designed to operate at 690 bar and with hydrogen as

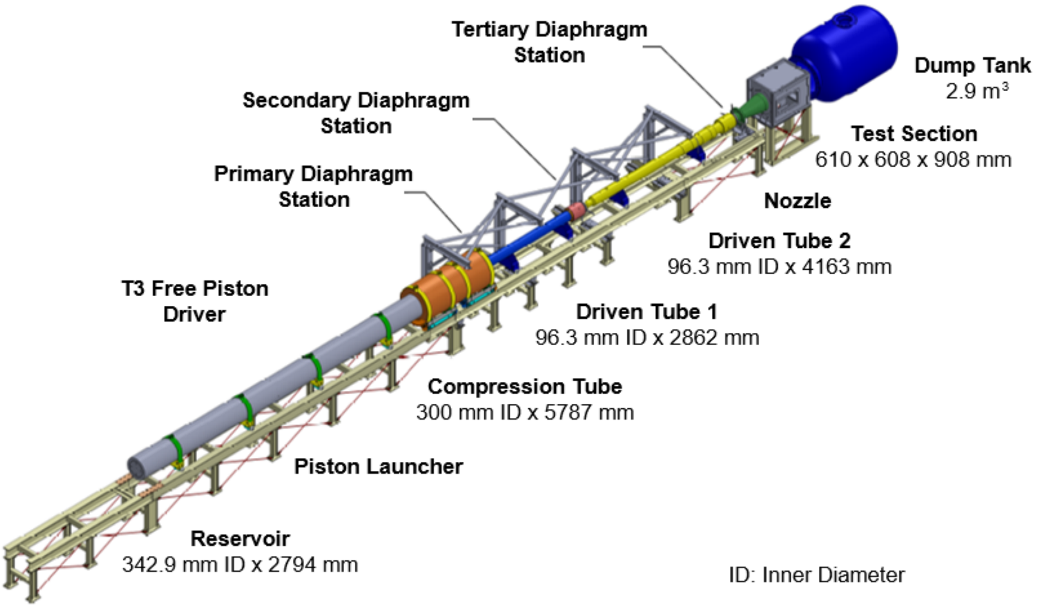

Figure 2.9: Scheme of the T6 shock-tube with dimensions. Adapted from Mcgilvray et al. [37].

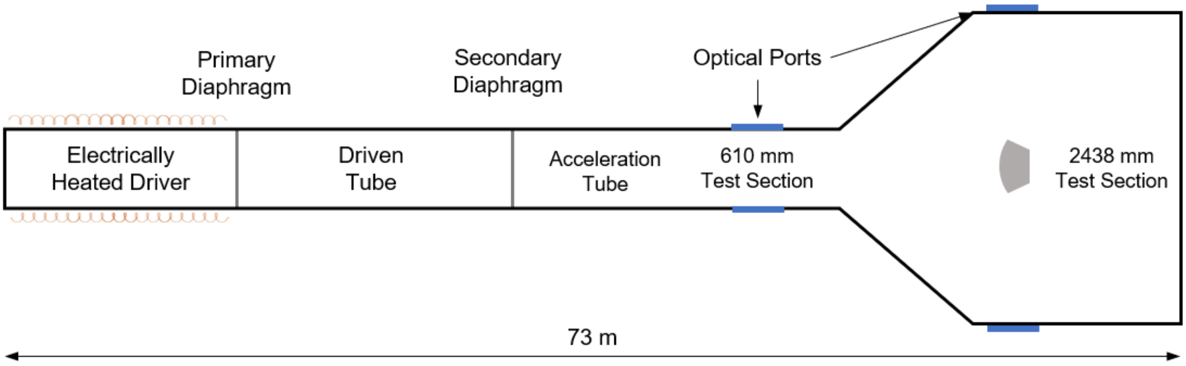

Figure 2.10: LENS XX schematic view. Adapted from [39].

the driver gas if the goal is a big performance, or argon, for bigger test times, or helium. The fact that LENS XX has larger chamber sizes brings many advantages for the investigations performed, although it is much more expensive to operate with such large amounts of gas. The length of approximately 73 m increases the test time and the large diameter produces a bigger core flow without significant viscous interferences, which creates a better quality test flow. Another benefit of a larger chamber diameter is the fact that the frequency of the acoustic waves, that act as disturbances, is lower. These disturbances were proven to come from the driver chamber and transmitted through the expansion wave by Paull and Stalker [40] and may disturb the flow significantly [41] [42].

One of the aspects that makes this facility versatile is the fact that it can also operate with four chambers, with an extra diaphragm, for a bigger performance. With this type of configuration shock speeds over 17 km/h can be achieved [43]. Besides this, the secondary diaphragm station is movable, which makes it easier to control the arrival of the tail of the secondary expansion or the reflected head of the secondary expansion wave, and hence, the test time can be optimized with a tailoring condition.

The LENS XX Expansion Tunnel has been used to study real gas effects, shock layer chemistry, viscous interactions, and ablation effects on the performance of hyper-velocity vehicles [43].

With this kind of driver, the maximum temperature achievable by the gas is around 700 K, the lowest operation temperature of the presented drivers [5]. Although it seems low, the LENS XX has a very good performance since it is operated as an expansion tube, which can maximize the shock speed. But the main advantage of this type of driver is the repeatability. Since the driver's gas temperature and pressure are easy to control and predict, the test conditions can be easily tuned and repeated. Another advantage of the electric heated driver is the fact that it does not produce soot, hence the produced flow is very clean [43].

2.2.3 Eletric Arc driver

Another type of driver used in high-performance facilities is the Electrical Arc Driver, EAST.

One of the facilities that operates with this type of driver is the Electric Arc Shock Tube, or EAST, at NASA Ames Research Center. Built-in 1965, EAST is composed of an arc driver that can have two configurations (conical or cylindrical), a driven tube with 9 m of length and 10.16 cm of inner diameter that includes the test section, if a reflected tunnel operation is being used, and 76.2 cm exit diameter nozzle, as it can be seen on figure 2.11 [5].

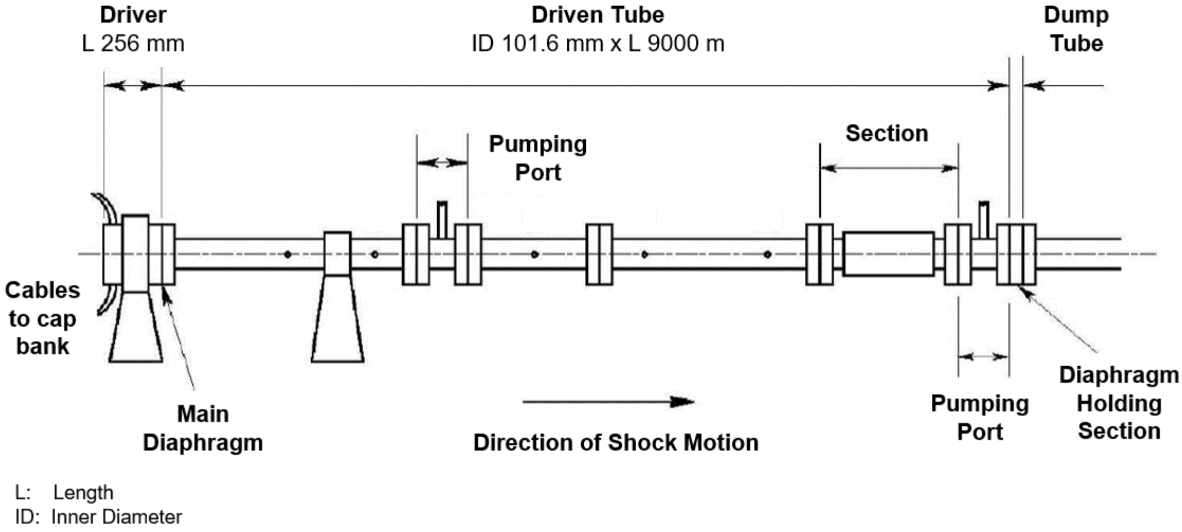

Figure 2.11: EAST schematic. Adapted from Grinstead et al [44].

The driver can operate with two types of configurations, a conical or a cylindrical driver represented in figure 2.12, (a) and (b) respectively. The conical driver has 25.6 cm of length, with sections of 6.35 cm and 10.16 cm of diameter inside the chamber, which has a volume of 1292 cm^3 [44]. The cylindrical driver has an inner diameter of 10 cm and a variable length of 34-137 cm and hence, a variable volume driver of 2700-10700 cm^3 . This characteristic is very useful since with a variable volume driver more sets of conditions, like temperature and pressure, may be obtained, and therefore, a wide range of shock wave velocities may be achieved. The main gases used in the arc chamber are $\mathrm{H_2}$, He, $\mathrm{N_2}$, or a combination of $\mathrm{H_2}$ and Ne [38].

As the name suggests, in this type of driver an electric arc is used to heat the gas. To do so, a high voltage electrode connected to a current collector ring and trigger wire along the length of the chamber is used. The trigger wire, made of tungsten, has one of the ends attached to the ring ground electrode, located at the end of the chamber. The other end of the wire is connected to a non-conducting pull cord that passes through the centre of the high voltage electrode. At the time the high voltage set-point is reached, the cord is pulled towards the high voltage electrode, connecting the wire, closing the circuit, and initiating the discharge [44].

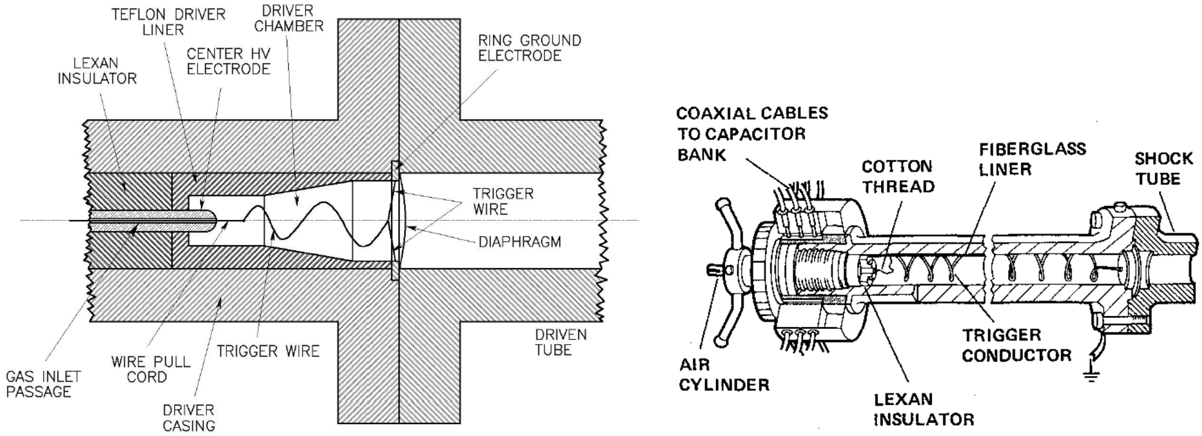

(a) Conical driver scheme. Taken from [45].

(b) Conical driver scheme. Taken from [38].

Figure 2.12: Scheme of EAST different drivers.

Once the trigger wire heats, its temperature starts to rise significantly by ohmic eating, and hence the surrounding gas. The heating of the gas causes its ionization as it becomes a plasma. With the presence of electrons caused by the ionization, the plasma conductivity increases, and a portion of the electric current passes through it. During this process, the temperatures can reach values of 8000 to 10000 K and the trigger wire vaporizes. Because the produced plasma is highly conductive, an electric arc forms as a result. The current rise strongly depends on the impedance of the gaseous discharge column in the driver, which in turn depends on the amount of and type of gas, density, charging pressure, ionization potential, and specific heat [38, 44].

Taking into account the described phenomena that occurs inside the arc chamber, when choosing which type of driver should be used, one must consider that the conical driver has a much smaller volume, which results in energy densities five times greater than with the cylindrical driver for the same energy source. Because of this, a larger pressure is obtained in the conical driver and hence bigger shock speeds are obtained [44]. By varying the type driver, the gas composition, capacity bank voltages, and the initial driver and driven pressures, a shock wave velocity range of 3.0-50.0 km/s can be obtained at EAST [38], where for the lower velocities the cylindrical driver is used, and for the greater velocities, the conical one is used instead.

Similar to EAST, Russia has an arc-driven shock-tube named ADST. This facility is located in TsAGI, Tsentralniy Aerogidrodinamicheskiy Institut, and there is little information about its activity, but it has been used to study ionization and radiation processes in the air behind shock waves with speeds between the range of 8-14 km/s [5].

Aforementioned, the test time of a shock tube is defined as the interval between the passage on the shock wave and the contact surface. In an arc-driven shock tube, the test times are shorter compared with the other facilities. Besides this, the driver's repeatability is poor, since the driver's conditions are hard to repeat in several shots due to the high variability of the phenomena. But since one of the requirements of the EAST facility was to be able to reproduce the aero-thermodynamics of a Jovian entry, the only driver capable of providing the necessary amount of energy to do so is the electric arc driver, with shock velocities up to 46 km/s [44]. The reached temperatures in this type of driver can also appear to be a limitation, but since the discharge time is very short, no melting or ablation of the surrounding occurs [38].

2.2.4 Combustion driver

In a combustion driver, as the name suggests, the driver gas is pressurized and heated using the constant volume combustion of the gas inside the closed chamber.

As it was discussed, to achieve high performance the driver gas must have a low molecular weight, high pressure, and high temperature. Taking this into account, the most suitable fuel for these requirements is hydrogen.

If the driver chamber was filled only with hydrogen and oxygen, a violent detonation would occur, an event that can lead to very low repeatability and high loads to the chamber. To avoid this, a third element must be added to partially absorb this energy and, instead of a detonation, the combustion proceeds as a deflagration. Since the purpose of the diluent is to only absorb energy, noble gases are used. Once again, if the goal is to reach higher performances, the most common gas used as a diluent is helium, the lightest noble gas.

This type of driver was the chosen configuration for the ESTHER shock tube, which operates with a mixture of $\mathrm{He/H_2/O_2}$ at initial pressures up to 100bar, and can reach final pressures of up to 600 bar. The chamber was designed considering existing combustion drivers designs, like the Convair shock tube and VUT-1 Shock-Tube from the Moscow Institute for Physics and technology [46]. The inner diameter is 200 mm it has a total length of 1.6 m. The length of the driver was calculated in [8] to avoid the scenario where the head of the expansion wave reflected from the end of the driver overtakes the primary shock wave before it reaches the test section.

One of the main innovations that came with ESTHER combustion driver development is the fact that the ignition of the combustible mixture is achieved using a laser. Usually, in a combustion driver, the ignition is achieved with spark plugs or a glowing wire system placed along the longitudinal axis, the case of the driver of Convair [19]. The glowing wire ignition was successfully tested in ESTHER scaled driver experimental campaign [46], and it was found that due to disintegration of the wire, residue started to build up inside the walls. As a result, this unwanted contamination could pollute the flow during the future operations of the shock tube. This configuration was later abandoned, and the laser ignition was successfully tested and demonstrated [20].

Although good performances can be achieved with a combustion driver, this type of configuration is limited by the adiabatic combustion temperature of the mixture, with further losses [5]. Another downside when considering high performances is the fact that adding oxygen to the mixture, so that combustion can occur, increases the average molecular weight [38].

2.3 The European Shock Tube for High Enthalpy Research

Since the 90's, the facility that provided support for European planetary exploration missions was TCM2, located in Marseilles, France. This facility maximum performance provided shock speeds of about 8-9 km/s. This range of speed was adequate for missions such as Huygens Titan entry (5.15km/s) or Mars exploration missions, however, it was not high enough to reproduce Earth super-orbital flows (11-12 km/s) [20]. When the shock tube TCM2 had its final stop, Europe did not possess similar experimental facilities and, as a consequence, ESA fostered the development of a new facility dedicated to such fundamental studies [5].

In the previous discussion about the different types of impulse facilities, it was shown that depending on the topic of study, each type of facility had an optimal range of applications. The shock tube is the best facility for investigating chemical kinetics and thermal relaxation after the shock since the flow is perfectly known. Hence, the main point is to obtain a pure shock wave with a clean environment, and avoid flow contamination, frozen flows, and minimize viscous effects [5]. As a consequence, if one is interested in scientific studies of chemical kinetics and radiation, a shock tube is the most suitable type of impulse facility. Subsequently, the European Space Agency has supported the development of the ESTHER shock-tube.

The European Shock Tube for High Enthalpy Research was designed and developed by an international consortium led by Instituto de Plasmas e Fusão Nuclear (IPFN), and built at Campus Tecnológico e Nuclear (CTN) in Instituto Superior Técnico (IST), under funding from the European Space Agency (ESA). This new Hypersonic research facility will provide Europe the ability to test flow conditions and the respective radiative environment to which the capsules of future missions are submitted during re-entry/entry.

During the development cycle of ESTHER, it was decided that the driver would be a combustion driver, contrary to the TCM2 piston driver. Therefore, a scaled driver was first tested, an operation that underwent from late 2012 to early 2017. With this experimental campaign, it was possible to implement laser ignition and improve the design of the driver and validate the driver performances predictions from the design phase. In 2019, the assembly operations were concluded and ESTHER was symbolically inaugurated [20]. Currently, ESTHER is under the qualification and testing phase, more precisely of the combustion driver.

2.3.1 Requirements

The main requirements of ESTHER facility are:

1. Reliability, repeatability, safety, and high performance.
2. Cleanliness.
3. Low-cost, high turnaround.

The first requirements are achieved mainly due to the design of the $\mathrm{He/H_2/O_2}$ combustion driver. When the driver is being operated in deflagration mode, it can provide reliability and repeatability to the operations, when compared with detonations or, for example, the electric arc type of driver previously presented. The operations of the shock tube are done remotely with an ATEX compliant control system, in a semi-buried building, and hence, safety is achieved. The high performance can be achieved with a driver that can reach pressures of up to 600 bar and also due to the addition of a second stage compression tube, and cross-area changes between every two consecutive sections.

The second requirement is of particular importance for good quality and clean test flows. With the use of low-carbon super-duplex steel and high-vacuum pumping, carbon pollution may be prevented. Besides this, the ignition of the driver mixture of gases is done with a laser, which avoids contamination like the one encountered if the ignition was carried with a hot wire as previously tested in the scaled driver campaign.

To fulfill the third requirement, the facility is automated in several ways, allowing it to be operated by two persons, and a range of 2-4 shots per days is expected. The diaphragms that separate the different sections will be produced on-site, reducing costs [20].

2.3.2 Design

In figure 2.13, a schematic view of the ESTHER shock tube is presented. This shock tube is composed of a driver followed by the compression tube and shock tube, and lastly, the dump tank. As it was mentioned, each of these sections has decreasing cross-section areas to increase the performance of the shock, discussed in section 2.1.3. The driver has a length of 1.6 m with an inner diameter of 200 mm. The compression tube has a length of 5 m and an inner diameter of 130 mm, followed by the shock tube with a length of 4 m, up to the test section, and an inner diameter of 80 mm.

The diaphragms between the different sections are located at the beginning of each convergent section since it was found that the best performance was gained with this configuration [47].

The compression tube is expected to be filled with helium between 0.01 bar and 1 bar, depending on the optimal intermediate pressure.

A dump tank recovers all the gases flowing in the wake of the shock wave. [8]

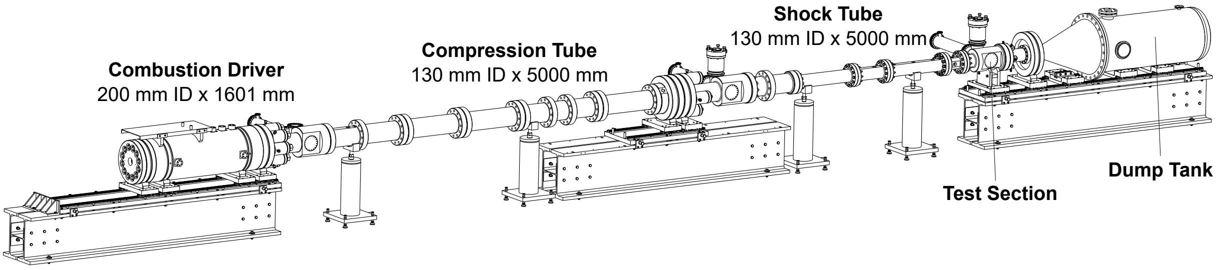

Figure 2.13: Schematic view of ESTHER shock tube

2.3.3 Performance

To calculate the performance of ESTHER, the software STAGG (Shock Tube And Gas Guns) was used. This software was developed by Fluid Gravity Engineering LTD and can model single or double diaphragm gas driven shock tubes with cross area reduction in the diaphragm sections. The models used to predict the performance are based on the work of Alpher and White [21], Walenta [48], and Mirels [22], discussed in sections 2.1.2, 2.1.3, and 2.1.4, respectively. For the parameter influence study, two atmospheres are plotted, Earth and Mars.

The calculations of shock speed and pressures at various points in the shock tube are based on the assumption of an isentropic, inviscid gas, conservation of mass and energy, and the sonic condition at the narrow points of convergent sections [49].

The performance is calculated taking into account the gas type, temperature, and pressure assigned to each section. The gases in the driver and test section can be modelled as ideal or taking into account high-temperature effects, the variation of C_p and γ, that are based on tables of Local Thermochemical Equilibrium (LTE).

The real gas properties tables were obtained with the NASA software named CEA (Chemical Equilibrium with Applications) which considers thermochemical equilibrium of the specified test and driver gas mixtures. Therefore, these flows are considered to be in chemical and thermodynamic equilibrium, which implies infinite chemical and vibrational rates, something that does not occur in practice.

The compression tube can only be modelled as an ideal gas, but since Helium will be the main gas used, this approximation is accurate since it is composed of a single atom gas which makes the van der Waals dispersion forces as low as possible.

On the next performance analysis, a special focus will be given to the driver gas mixture.

Firstly, the influence that the main initial parameters have on the performance will be discussed. Secondly, the influence that these parameters have on the test times will be analysed, followed by the performance envelope with a single and double configuration.

2.3.3.1 Driver Conditions

Some of the main parameters that will influence the shock tube performance will be the conditions of the driver. Aforementioned, for higher performances one wants the driver gas to be light, at high temperatures and pressures, and the opposite for lower performances. This can be achieved with a combustible mixture of H_2 with O_2 diluted with He and also N_2 to avoid detonations.

Since this is a combustion driver, a chamber is filled with a combustible gas mixture where a constant volume combustion occurs upon ignition, increasing the pressure and temperature of the gas.

In the experimental scaled driver laser campaign that took place in 2016 and 2017, several shots were performed to understand how to operate a combustion driver and the dynamic of high-pressure combustion. During this campaign, high-pressure combustion experiments of H_2 and O_2 diluted with He were done, and it was found that the optimal molar ratios of $He/H_2/O_2$ were found to be 8/2/1.2, enabling good repeatability, low acoustics phenomena, and good performance.

The performance and operation of the full-scale combustion driver are further discussed in chapter 3.

In table 2.1, the theoretical results of a constant volume and adiabatic combustion process are given for two different initial gas mixtures with an initial pressure of 50 bar, each with three molar ratios between elements. If instead of using He as the diluent N_2 is used, lower performances can be achieved. The subscript ad stands for adiabatic since these values are for an ideal and equilibrium combustion process and in reality losses will occur.

Table 2.1: Theoretical driver gas properties for adiabatic process at constant volume and initial pressure of 50 Bar

Mixture	Molar Ratios	R (J $kg^{-1}K^{-1}$)	$p_{11_{ad}}(Bar)$	$T_{11_{ad}}(K)$	$\gamma_{11_{ad}}$	$a_{11_{ad}}(m/s)$
$He/H_2/O_2$	9/2/1.2	1293	470	3036	1.35	2211
	8/2/1.2	1251	483	3140	1.3259	2185
	8/2/1.3	1210	479	3113	1.3282	2142
$N_2/H_2/O_2$	9/2/1.2	344	342	2222	1.2572	940
	8/2/1.2	349	358	2339	1.2499	965
	8/2/1.3	348	355	2322	1.2488	960

The adiabatic flame properties differences between the $He/H_2/O_2$ and $N_2/H_2/O_2$ initial mixtures are considerable in many aspects. First, the specific gas constant for each is much lower for the N_2 mixture, since the molar mass is bigger. Second, the adiabatic equilibrium pressure is much lower for the N_2 mixture, which will result in a higher initial amount of gas to reach a certain final pressure. This same behaviour occurs for the adiabatic flame temperature. These aspects, along with a lower heat capacity ratio for the N_2 mixture, will result in significant differences in the speed of sound and hence, performance.

To simulate the performance of ESTHER, lower flame temperatures were used, since heat losses at the driver walls will occur. For the mixtures with He as the diluent, a flame temperature of 2650 K was used, and for the mixtures, with N_2 as the diluent, a temperature of 1800 K was used.

In figure 2.14 the influence of the driver gas pressure and mixture on the mainshock speed is plotted, in (a) for the mixtures diluted with He and in (b) with N_2, with a test gas pressure of 10 Pa and the optimal pressure at the compression tube section.

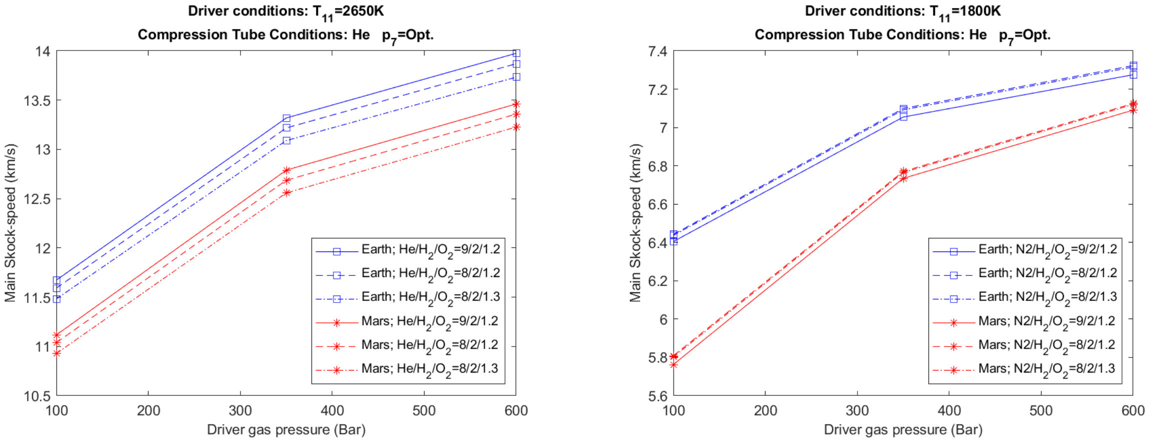

(a) (b)

Figure 2.14: Influence of the driver gas pressure and composition on the main shock speed for different test gases.

For the mixture with He, taking into account that in the simulations the flame temperature was the same for all of the mixtures, the one with the higher speed of sound will correspond to the mixture with the highest R and γ_{11}. From table 2.1, this mixture will correspond to the one with the molar ratio of $9/2/1.2$. Using the same order of thoughts to the mixture with $\mathrm{N_2}$, the one with the highest speed of sound will be $8/2/1.2$.

From the figure 2.14, the mixtures with the highest speed of sound offer a bigger performance, with the helium mixtures offering shock velocities with almost double of speed than the mixtures with $\mathrm{N_2}$. These performance differences will be a good thing since it will be possible to recreate test flows for a wide range of velocities as will be seen in the performance envelopes section.

In the $\mathrm{N_2}$ mixtures, the difference between the results of the main shock speed with the $8/2/1.2$ and $8/2/1.3$ is very slight when compared to the ones with Helium. This can be explained since the molar weight of oxygen is closer to the molar weight of $\mathrm{N_2}$ than He that is much lighter, and hence, a bigger molar ratio of $\mathrm{O_2}$ will impact the mixtures with He more.

Another aspect that can be confirmed from these plots is the increasing shock speed for higher driver gas pressures.

Besides the driver's final combustion pressure, it is also interesting to analyse the influence that the final combustion temperature (T_{11}) has on the shock tube performance. When considering the real performance of the driver, which will be further discussed in chapter 3, losses during the combustion process will occur, and the final temperature will depend on the combustion efficiency.

In figure 2.15, the influence that T_{11} has on the main shock speed is given for a He or $\mathrm{N_2}$ as the diluent, and with the conditions mentioned on the title. The temperature range used is considering a combustion efficiency from approximately 50% to 100%, and considering the adiabatic flame temperature for each mixture.

The post-combustion temperature has a significant influence on the shock tube performance, where for the mentioned initial conditions, it increases almost linearly with this parameter. As the temperature increases, the speed of sound of the mixture is also bigger. Like it was mentioned in section 2.1, the higher the speed of sound, the higher the performance of the facility, and the opposite behaviour the other way around.

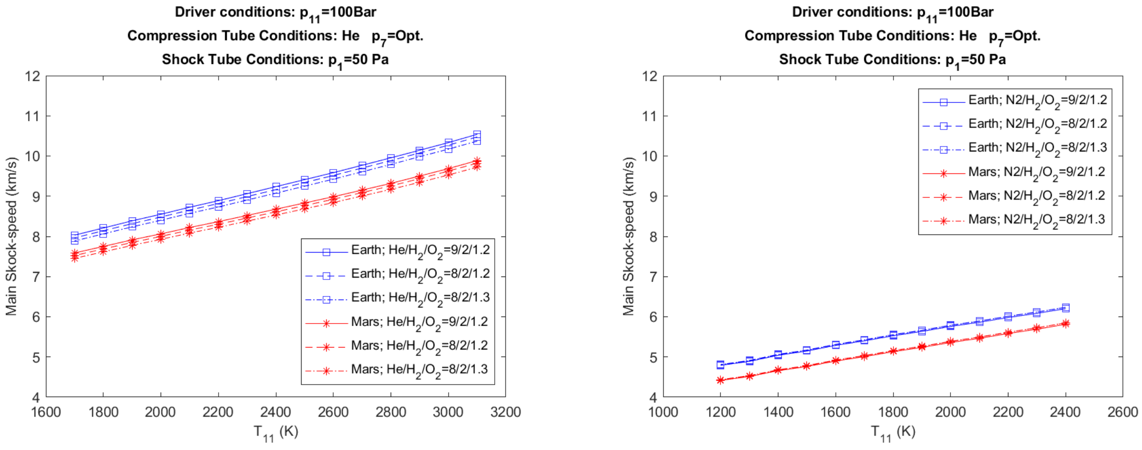

(a)

(b)

Figure 2.15: Influence of the post combustion temperature T_{11} on the sock-tube performance with double configuration.

With the knowledge and understanding of the combustion process that comes from the operation of the driver in chapter 3, this can be another parameter used to vary the performance of the shock tube.

2.3.3.2 Compression Tube Conditions

One of the aspects that has to be taken into account is the compression tube length of 5 m. As it was explained in section 2.1.3, from the work of Walenta, the wave generated at the intersection of the primary contact surface with the shock reflected from the second diaphragm must not overtake the main contact surface before the test section. This condition gives the minimum value of $(x_7/x_{test})_{min}$, and taking $x_{test} = 4m$ the minimal length of the compression tube can be calculated.

The value x_{7min} will be mainly influenced by the compression tube pressure and also test gas mixture and pressure. In figure 2.16 (a) the influence of the compression tube initial pressure on the value of x_{7min} is represented for a driver initial gas mixture of $\mathrm{He/H_2/O_2}$. Three different atmospheres were tested, excluding the gas giants atmosphere since it was not limited by x_7. For each atmosphere, four different test pressures were evaluated. As a reference, the design limit of $x_7 = 5m$ is also plotted.

From figure 2.16 (a), as the compression tube pressure decreases, the minimum length increases significantly. This analysis is of particular importance to study the lower performances of ESTHER that can be useful for test atmospheres of Mars, and Titan.

In figure 2.16 (b) a plot of the influence of the compression tube pressure on the main shock speed is presented. The crosses on each line represent the minimum pressure so that $x_{7min} > 5m$ for each test gas, and hence, they represent the minimum performance for this driver test conditions.

The same analysis was done with a driver gas mixture with $\mathrm{N_2}$ as the diluent. The same conditions are used, except for the driver gas temperature that is lower with $\mathrm{N_2}$ as the diluent. Only the atmospheres of Titan, and Mars are analysed since this driver gas mixture is used to achieve lower performances.

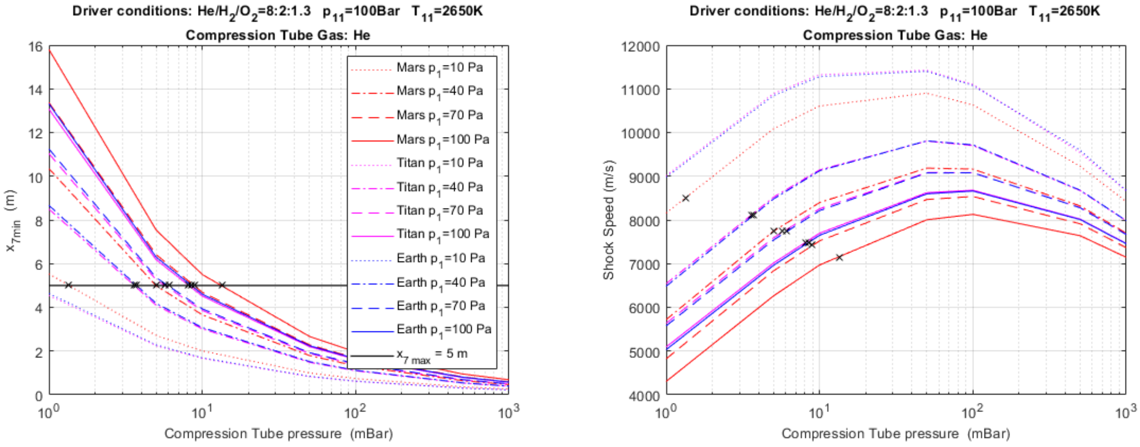

(a) (b)

Figure 2.16: Influence of the compression tube pressure on x_7 and main shock speed for different test gases.

In figure 2.17 (a) the value of x_{7min} versus the compression tube pressure is given for these new driver conditions. This parameter is weakly influenced by the driver conditions as shown by comparing this plot with 2.16 (a). In figure 2.17 (b) the shock speed versus the compression tube pressure is presented, where the crosses represent the lowest pressure and shock speed attainable for the mentioned conditions.

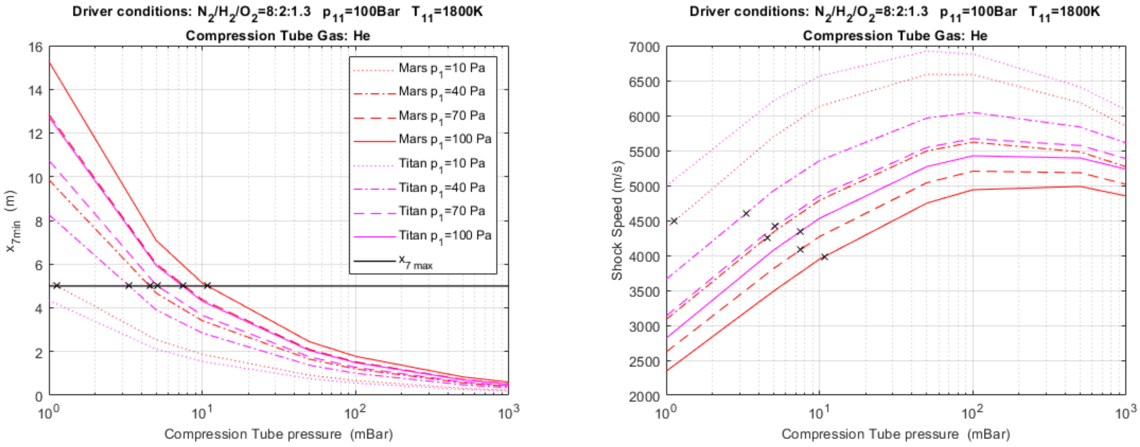

(a) (b)

Figure 2.17: Influence of the compression tube pressure on x_7 and main shock speed for different test gases.

2.3.3.3 Shock Tube Conditions

The shock tube conditions will depend mostly on the purpose of the experience, so there aren't many parameters that can be changed on this section without compromising the test flow purpose.

In figure 2.18 the influence that the test gas pressure has on the main shock speed is plotted. These results were obtained with a driver gas pressure of 100 bar, helium in the compression tube with optimal pressure. As the test gas pressure is increased, the shock speed decreases. This behaviour is expected since the pressure ratio p_{11}/p_1 decreases, and hence, the performance also decreases.

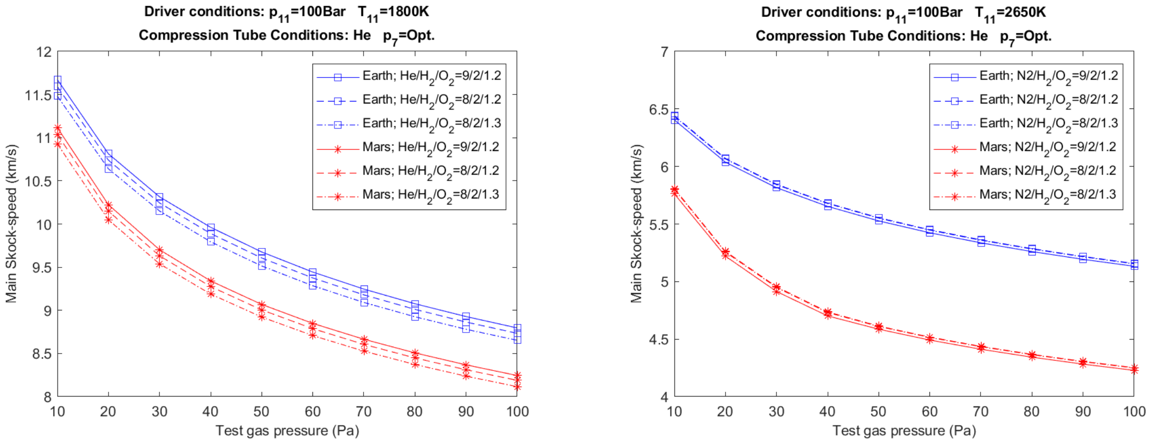

(a)

(b)

Figure 2.18: Influence of the test gas pressure on the performance.

For higher performances like the ones required by gas giants entry speeds, an aspect that can be varied in the shock tube section is the composition of the test gas, which can be diluted with noble gases like helium or neon.

Based on the work of Stalker and Edward [50], in blunt-body simulations for gas giants entry it was proposed to increase the molar percentage of Helium or substituting it with Neon to simulate create hotter shock layer at lower speeds than the atmospheric entry ones. This study was done in the work of Diana Luís [8]. It was found that when He was added with a molar percentage of 90%, to the $\mathrm{H_2/He}$ mixture, an increase of 3.8% on the shock speed was observed, and the post-shock temperature more than doubled when compared to the mixture with 10% of helium. When Neon was added instead of Helium, the shock speed decreased slightly and the post shock temperature increased around 42%.

2.3.3.4 Test times

Using the theory of Mirels [22], given in section 2.1.4, the test times for different initial conditions, for a test section location at 4m from the second diaphragm, are presented. It is assumed that the flow between the shock and contact surface is steady at each instant but also that the contact surface is moving away from the shock wave, which is not totally accurate however it gives qualitatively correct results.

Because of this, all of the presented results will be analysed in a qualitative approach, since these theories are more accurate once the model can be calibrated with ESTHER experimental results.

Similar to the previous performance results, the influence of the main initial parameters will be presented. In this analysis, the influence of the compression tube conditions will be excluded, and the considered pressure for this section is the optimal one computed by STAGG.

Firstly, the influence that the driver gas pressure (p_{11}) has on the test time is presented. This is shown in figure 2.19, with a p_{11} range from 100 bar to 600 bar, for Earth and Mars atmospheres, and with an initial driver gas composition diluted with He, (a), or $\mathrm{N_2}$, (b).

As the driver gas pressure increases, the test time decreases both for He and $\mathrm{N_2}$ as the diluents. When Helium is used as the diluent instead of nitrogen, the test times decrease more than two times for the atmosphere of Mars and more than three times for the atmosphere os Earth. Considering the composition differences, the mixture with higher He dilutions has bigger test times, and the same behaviour is observed but for lower $\mathrm{N_2}$ dilutions.

The test times will be highly dependent on the main shock speed, since it is defined as the useful flow at x_{test} between the arrival of the shock and the contact surface, and this is very visible on the obtained results, that have the exact opposite behaviour as the ones in figure 2.14. For higher shock speeds, the test times decrease, and the opposite for lower shock speeds.

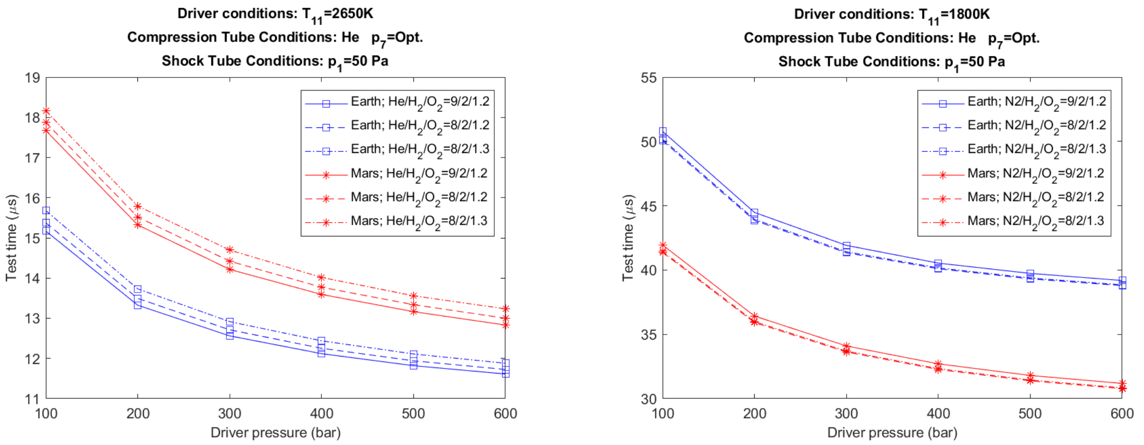

(a)

(b)

Figure 2.19: Influence of the driver's gas pressure on the test time.

Besides the influence of the driver gas pressure, the temperature also has a big impact on the test time. In figure 2.20, a plot of T_{11} versus the test time is given, in a temperature range that corresponds approximately to a combustion efficiency of 50% to 100%. Higher shock speeds seem to offer lower test times once again, excepting for the Mars atmosphere and He as the diluent when the temperature is below 2400 K.

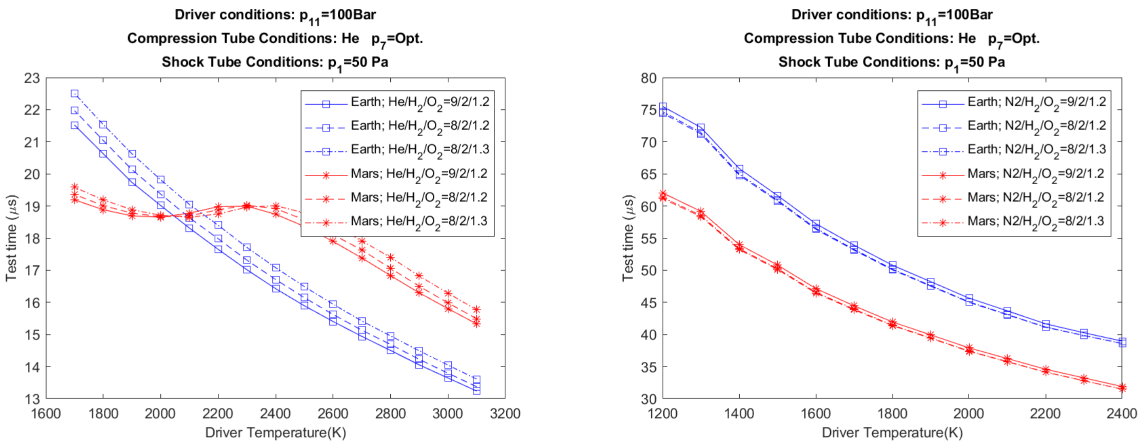

(a)

(b)

Figure 2.20: Influence of the driver's gas temperature on the test time.

Finally, the influence of the working gas pressure is presented in figure 2.21. For both dilutions, as the test gas pressure increases, the test time increases. This is mainly because the pressure ratio p_{11}/p_1 is decreasing with increasing p_1, and hence, the shock velocity decreases. For a test gas pressure of 10 Pa, the driver gas diluted with He presents a test time more than two times inferior when compared to the same $\mathrm{N_2}$ diluted mixture. For a test gas pressure of 100 Pa, this ratio increases to more than three times for the Earth atmosphere.

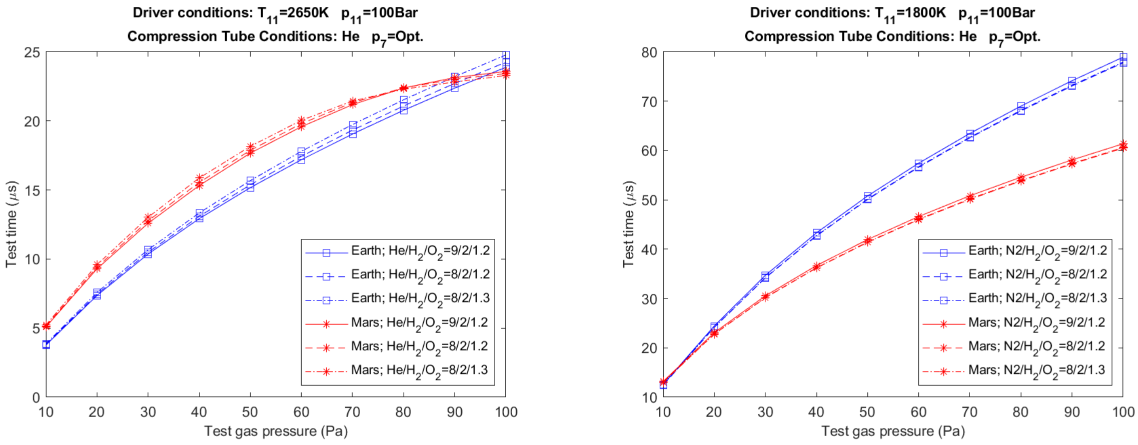

(a) (b)

Figure 2.21: Influence of the compression tube pressure on x_7 and main shock speed for different test gases.

2.3.3.5 Performance Envelopes

In this section, the performance envelopes for the initial driver mixtures of $\mathrm{N_2/H_2/O_2}$ and $\mathrm{He/H_2/O_2}$ with a ratio of 8/2/1.3, are given. The influence that the driver's initial gas composition has on the shock tube performance was already given in the previous sections, and the 8/2/1.3 mixture is one of the initial filling ratios that will be used during the driver operation, as it will be shown in chapter 3.

For a double configuration and a driver´s gas mixture of $\mathrm{He/H_2/O_2}$, the lossless performance envelope for Earth, Mars, Titan, and the Gas Giants is given in figure 2.22. This envelope is limited by four boundaries, being those the performance for the upper and lower test gas pressure, and the performance when the maximum driver pressure (600 bar) and an optimal intermediate pressure is used, and on the left side, the minimum performance for $x_7 > 5m$.

For the Earth atmosphere, the obtained performance is within some of the registered entry speeds, given in figure 1.1, and even with a heavier driver gas mixture, the obtained performance is suitable.

For Mars and Titan's atmosphere, the registered entry speeds during missions are much lower, within 4 km/s to 7 km/s, and for this envelope, these performances are not within the boundaries.

For lower performances, the initial driver gas mixture may be switched to $\mathrm{N_2/H_2/O_2}$. In figure 2.23, the performance envelope for this mixture and the same ratio as the previous one is given. Since the lower performances are more relevant to Mars and Venus atmosphere, only these two are provided.

With these initial conditions, the registered entry speeds in figure 1.1 are within the performance

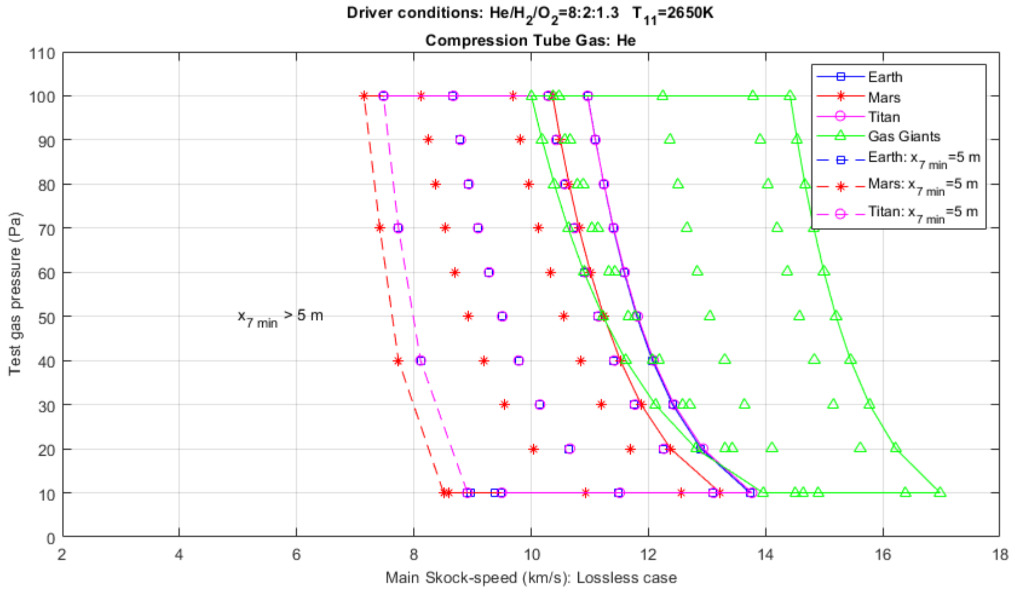

Figure 2.22: ESTHER performance envelope with double diaphragm configuration for a $\mathrm{He/H_2/O_2}$ initial gas driver mixture.

envelopes when $\mathrm{N_2}$ is used as the diluent. Furthermore, these performance envelopes don't include losses and for real scenarios, the shock velocity will be lower.

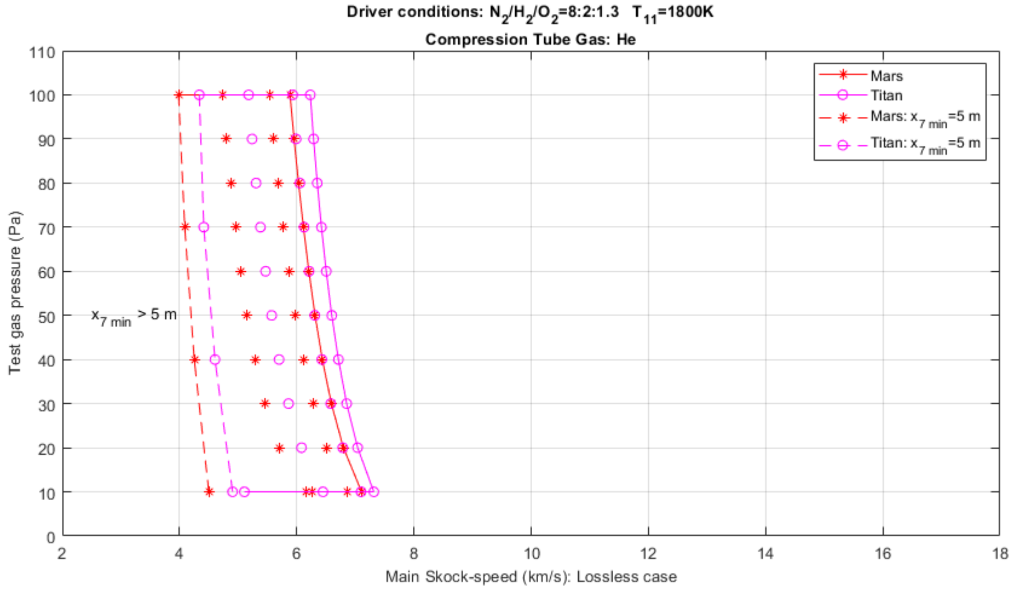

Figure 2.23: ESTHER performance envelope with double diaphragm configuration for a $\mathrm{N_2/H_2/O_2}$ initial gas driver mixture.

Besides the double configuration, it is possible to use ESTHER with a single diaphragm, where the driver is directly connected to the shock tube. With this configuration, the performance will be mainly influenced by the driver's conditions, and the shock velocity range will be more narrow since the absence of the compression tube reduces the possible span of performances. Nevertheless, it is interesting to observe that the obtainable performances with a single configuration are the lowest.

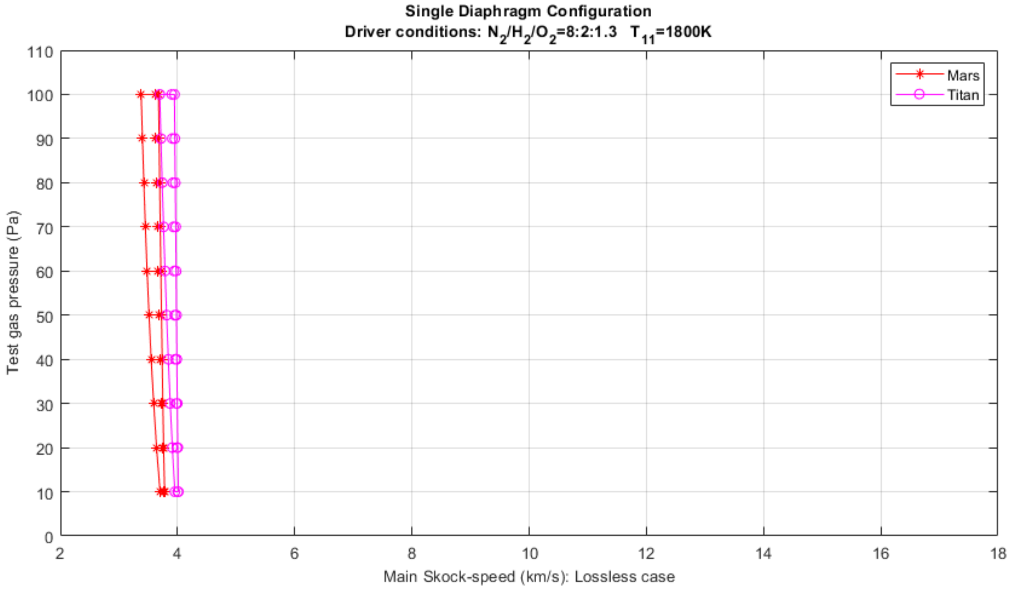

Figure 2.24: ESTHER performance envelope with single diaphragm configuration for a $\mathrm{N_2/H_2/O_2}$ initial gas driver mixture.

Chapter 3

ESTHER combustion driver: Background and operation

The performance of the driver is crucial to achieving the desired shock speeds mentioned in the previous chapter. Like it was discussed previously, parameters like the pressure and gas composition of the driver will influence the overall performance. On the other hand, the way to achieve these conditions needs to be studied and analysed to operate ESTHER in its full capacity.

In this chapter, the experimental campaign of ESTHER combustion driver is presented. Firstly, the necessary theoretical background regarding premixed combustion in confined places is presented, followed by a review of the operation of previous combustion drivers. Secondly, the results of the experimental campaign are presented and discussed.

3.1 Background: Premixed flames

The first thing that has to be acknowledged when studying the theory behind ESTHER's combustion driver is the fact that the combustible mixture inside the chamber is at rest, and pre-mixed before the ignition. When the mixture is ignited by the laser in a channel located inside the driver end tap, a flame is initiated and propagates towards the unburned mixture, forming a combustion wave. This phenomenon is categorized as premixed flame, and is a very fundamental phenomenon of combustion.

As it was discussed in section 1.2, one of the main requirements for ESTHER is repeatability. To accomplish this, the driver must be able to perform in a repeatable way, and hence, combustion should occur as a deflagration. Phenomena, like detonations, that have an unpredictable nature have to be avoided.

To understand these phenomena some parameters that characterize a combustible mixture have to be introduced.

3.1.1 Concepts and definitions

In equation (3.1), the so-called air-fuel equivalence ratio is given. This parameter gives a relation between the mixture ratio of the number of moles of oxidizer and fuel, divided by this same ratio for the stoichiometric molar numbers. If $\lambda > 1$ the mixture is denominated as fuel-lean or oxidizer rich, but if $\lambda < 1$, the mixture is denominated as fuel-rich or oxidizer lean.

$$\lambda = \frac{(n_{oxi}/n_{fuel})}{(n_{oxi}/n_{fuel})_{stoi}} \tag{3.1}$$

In combustion drivers such as the one present in ESTHER, the fuel that is used is hydrogen and oxygen as the oxidizer. Besides these two elements, a third one is used to dilute the mixture. The presence of this diluent influences the combustion of the mixture and hence, a dilution ratio is given in equation (3.2) to quantify the ratio between the number of moles of diluent and the stoichiometric number of moles of fuel. Besides this parameter, the molar fraction x_i will also be used to characterise the amount of diluent.

$$D = 2\frac{n_{dil}}{n_{\mathrm{H}_2}}. \tag{3.2}$$

Another aspect that strongly influences combustion is the underlying chemical processes. In many flow regimes, like deflagration, the chemical reaction rates have a very strong influence on the rate at which combustion occurs. For the fuel of interest in this work, H_2, the overall reaction that translates how many moles of fuel react with the oxidizer, O_2, to produce the stoichiometric amount of combustion products moles, is given by the chemical reaction (3.3).

$$2\mathrm{H}_2 + \mathrm{O}_2 \rightarrow 2\mathrm{H}_2\mathrm{O}. \tag{3.3}$$

However this chemical reaction is simply the summarized chemical process that occurs since in reality, many sequential elementary reactions with intermediate species occur before the formation of the final combustion product, $\mathrm{H}_2\mathrm{O}$.

From experimental measurements, the rate at which the fuel is consumed can be given by equation (3.4), where the notation $[X_i]$ expresses the molar concentration of the chemical species, and k_G is called the global rate coefficient, that is strongly influenced by temperature. The exponents a and b are related with the reaction order, where $(a+b) = \mathfrak{n}$ is called the overall reaction order. For global reactions, these values are derived from experimental data.

$$\frac{d\,[\mathrm{H}_2]}{dt} = -k_G\,[\mathrm{H}_2]^a\,[\mathrm{O}_2]^b\,. \tag{3.4}$$

In a deflagration regime, the propagation of the flame in the normal direction, relative to the unburnt gases, is mentioned as the local burning velocity, S_L^0. The velocity at which the flame moves is called the flame propagation velocity S, and these two velocities can be related through equation 3.5, where a local balance between, represented in figure 3.1 the flow velocity U and these velocities is done.

$$\boldsymbol{S} = \boldsymbol{U} + S_L^0 \boldsymbol{n}_f \tag{3.5}$$

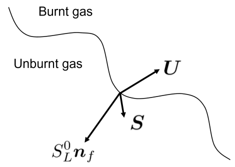

Figure 3.1: Scheme of the burning velocity S_L^0, flame propagation velocity $\boldsymbol{S}$, and flow velocity $\boldsymbol{U}$ at an iso-surface.

3.1.2 Regimes of flame propagation in tubes

The phenomenon behind the propagation of a flame inside closed tubes is a complex process that can be influenced by many aspects. The flame speed will depend on the regime of flame propagation, which can be classified as laminar flames, turbulent flames, both classified as deflagration, and finally, detonations. The lowest flame propagation velocity is given by the laminar regime, followed by a spectrum of turbulent flame velocities and an upper limit given by the Chapman Jouguet detonation velocity, known as the ideal detonation.

Represented in figure 3.2, the possible paths and steps of flame evolution inside a tube are given. Once the flame propagation starts, it can evolve in several ways depending on the conditions and even the source of ignition. If the ignition is weak, a laminar flame is produced, however this flame is prone to instabilities and it can evolve to a wrinkled/cellular flame, where the surface area increases. Once the surface area increases, the mass burning rate will also increase raising the burning velocity. Owing to this chain of events, turbulence can start to grow and a turbulent flame is generated. From the turbulent flame, further acceleration can take place, and depending on how strong this acceleration proceeds, the flow may transit to a detonation (DDT, Deflagration to Detonation Transition), or remain turbulent, subsonic, or supersonic.

In the next sections, these regimes of flame propagation and related phenomena are discussed.

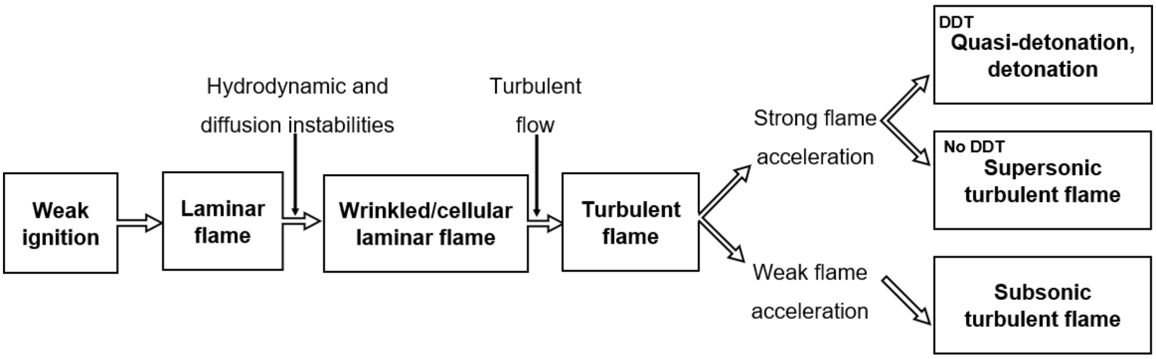

Figure 3.2: Sequence of flame propagation regimes inside chamber.

3.1.2.1 Laminar flames

In a deflagration, the flame propagates at subsonic velocities with a rate that is controlled by diffusion of heat and reactive species from the reaction zone to the unburnt gas. If the unburnt gas is stationary, the flame will proceed as laminar, however if the unburnt gas is turbulent, the burning velocity may increase and is then called the turbulent burning velocity.

The laminar flame properties like the structure and burning velocity, are very important to understand the propagation of these flames, not only in the laminar regime but also in turbulent flames. In both laminar and turbulent flames, the same physical processes are present, and many turbulent flame theories are based on an underlying laminar flame structure [51].

In figure 3.3, a simplified scheme of the structure of a steady-state one dimension laminar flame is shown. The flame can be divided into four zones, being those, the unburned gases, the preheating zone, the reaction zone, and the equilibrium zone. The unburned mixture zone is the combustible mixture that comprises the fuel and the oxidizer before combustion. This zone is followed by the preheat zone where the heat release from the chemical reactions is conducted towards the unburned zone, which has an enhancement effect on the chemical reaction of the unburned mixture. The reaction zone is where the combustion chemical reactions take place, and hence the reactants are consumed, producing the combustion products and releasing heat through exothermic reactions. In an unconfined space, the pressure difference across a subsonic flame is almost zero, and the density of the burnt mixture is much lower due to the expansion effect. The equilibrium zone is the region with the burnt mixture that will remain close to an equilibrium state.

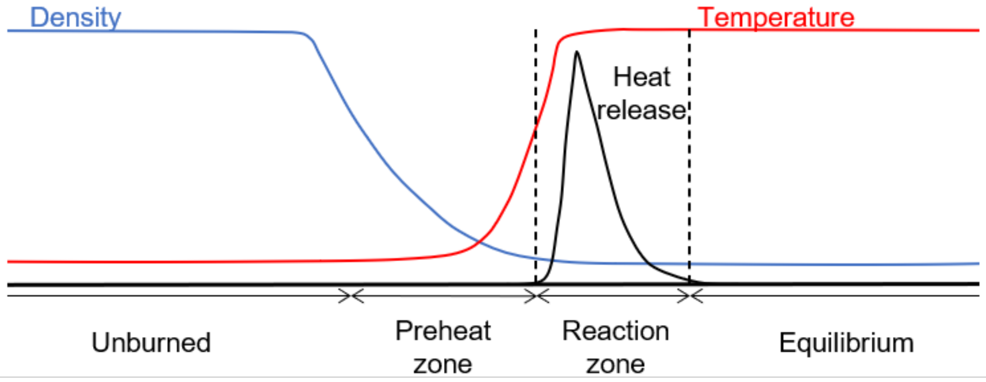

Figure 3.3: Simplified scheme of the laminar flame.

However in a confined tube, the pressure profile across the flame will not be constant as the one from an unconfined flame. For a constant volume combustion process, the pressure and temperature of the mixture will increase due to the compression that the combustion wave induces as it propagates.

One of the characteristic properties of these flames is the flame thickness, which consists of the reaction zone and the preheat zone. For a laminar premixed flame, δ_f can be given by equation 3.6a [52], where α is the thermal diffusivity of the unburned gas, and S_L^0 is the laminar flame speed. However this flame thickness, also mentioned as diffusion thickness, is much smaller than the thickness of a realistic flame. Another way to define δ_f is with equation 3.6b, where T_b is the flame temperature, and T_u is the unburned temperature.

$$\delta_f = \frac{\alpha}{S_L^0}. \qquad (3.6a) \qquad \delta_f = \frac{T_b - T_u}{\max(|\partial T/\partial x|)} \qquad (3.6b)$$

In the ESTHER combustion driver, high-pressure combustion will take place, since the filling pressures will vary from 5 bar up to 100 bar. There are several experiments and studies about atmospheric pressure combustion of $\mathrm{H_2}$, but for high pressure, very few experimental and computational studies can be found. Nevertheless, some mechanisms have been partially understood.

From the literature, the laminar flame speed of mixtures with a pressure range from 3 to 20 bar and several dilution ratios for He as the diluent, can be found.

With a heat and mass balance in the flame region, it is possible to conclude that the mass burning rate per unit area of the laminar flame, $\dot{m}_b^0$, is related to the global reaction rate k_G through $\dot{m}_b^0 \propto k_G^{\frac{1}{2}}$ [53].

The overall reaction rate of the mixture can be related as equation (3.7), where p is the mixture pressure, T_{ad} is the adiabatic flame temperature, $\mathfrak{n}$ and E_a the overall reaction order and activation energy respectively, that are determined empirically.

$$k_G \propto p^{\mathfrak{n}} \exp\left(-\frac{\mathrm{E}_a}{2R\,\mathrm{T_{ad}}}\right). \tag{3.7}$$

From this equation and since $\dot{m}_b^0 \propto k_G^{\frac{1}{2}}$, equation (3.7) can be written as equation (3.8).

$$\dot{m}_b^0 \propto p^{\frac{\mathfrak{n}}{2}} \exp\left(-\frac{\mathrm{E}_a}{2R\,\mathrm{T_{ad}}}\right). \tag{3.8}$$

The mass burning rate $\dot{m}_b^0$ indicates the burning intensity of the laminar flame, and this may be related to its velocity through equation (3.9), where ρ_u is the density of the unburned mixture. Hence, equation 3.8, may be expressed as (3.10), and the relation between the mixture pressure and laminar flame speed is obtained.

$$\dot{m}_b^0 = S_u^0 \rho_u. \tag{3.9}$$

$$S_L^0 \propto p^{\frac{n}{2}-1} \exp\left(-\frac{\mathrm{E}_a}{2R\,\mathrm{T_{ad}}}\right). \tag{3.10}$$

From equation (3.10), it is expected that the laminar flame speed increases with pressure when $\mathfrak{n} > 2$, but behaves oppositely when $\mathfrak{n} < 2$. It has been found that for combustion experiments of $\mathrm{H_2}$, with pressures above 10 atm, the reaction order is negative, and for pressures below 10 atm the reaction order is positive but below 2 [54]. Hence, it is expected that as the pressure increases, the laminar flame speed decreases.

In the work of Tse et al. [55], high-pressure combustion experiments were done, and the laminar flame speed for mixtures of up to 20 atm of $\mathrm{H_2/O_2/He}$ were calculated. In figure 3.4 the laminar flame speed relation with the equivalence ratio is given, for three different pressures and a dilution ratio of $D = 11.5$, obtained from [55]. The laminar flame speed is bigger for richer mixtures and decreases as the pressure increases, as it was expected of the previous analysis from equation (3.10).

Due to the highly diffusive nature of hydrogen, the peak value of flame propagation speed will shift to the fuel-rich side.

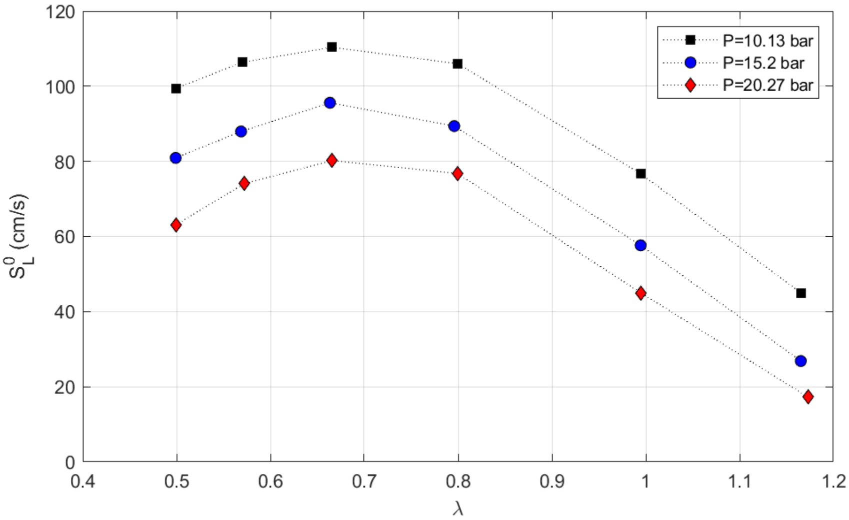

Figure 3.4: Laminar flame speed dependence on equivalence ratio (λ), with a dilution percentage of $\%He = 70 - 80$, and different pressures. Adapted from [55].

In the work of Burke et al. [54], more high pressure combustion experiments were performed, this time with a wider set of high pressures that could reach 25 atm. More than one type of diluent was used, but since helium is the main choice of diluent in ESTHER, only these results will be shown. In figure 3.5 three plots of the laminar flame speed dependence on pressure are given, for three equivalence ratios $\lambda = 1.176$, $\lambda = 1$, and $\lambda = 0.667$, where the first two plots were adapted from [54], and the last from [55].

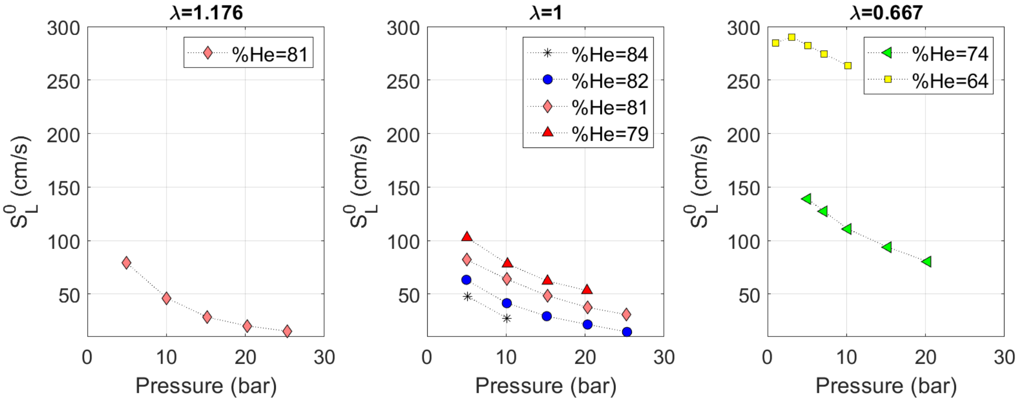

Figure 3.5: Laminar flame speed dependence on pressure for $\lambda = 1.176$, $\lambda = 1$, and $\lambda = 0.667$, for different dilution ratios. Adapted from [54], [54], and [55] respectively.

Once again, the influence that pressure has on the laminar flame speed of these mixtures is apparent: as pressure increases the speed decreases. Besides this, the influence of the dilution ratio may also be understood. From the second plot, as the dilution ratio decreases, and hence there are fewer moles of Helium to a fixed number of moles of Oxygen, the laminar flame speed increases.

3.1.2.2 Flame instabilities

As shown in figure 3.2, once the laminar flame develops, it can undergo instabilities that can have several types of physical nature and origins. After these instabilities develop, the flame can undergo a transition to a turbulent flame, which occurs when instabilities in a flow are not sufficiently damped by viscous action and the fluid velocity at each point in the flow exhibits random fluctuations.

The physical origins of these instabilities may have several sources. One of them is the hydrodynamic instability, also known as the Darrieus-Landau instability. A premixed planar flame will be intrinsically unstable due to the thermal expansion of the gas produced by the combustion process. If this plane is perturbed in any wavelength, the flame is disturbed and the streamlines will deflect, which will lead to a pressure gradient boosting the displacement of the flame front and increasing the initial curvature. This behaviour can be seen in figure 8 in the work of Ciccarelli and Dorofeev [56]. It can be identified visually on the flame surface, which will first develop a cracked look and later develop to smaller cells like observed in [55].

Another instability that will be present is the thermal-diffusive instability, which will occur if there is a difference in thermal conductivity and molecular diffusivity of the deficient reactant. For a combustible mixture of $\mathrm{O_2}$ and $\mathrm{H_2}$, the diffusivity of $\mathrm{H_2}$ is much larger than $\mathrm{O_2}$, and hence, fuel-lean mixtures of $\mathrm{H_2}$ and $\mathrm{O_2}$ will be very susceptible to this instability. Another aspect that can contribute to this effect is the mixing of the gases, that if poorly done (non-homogenous distribution of reactants), will boost this instability. This will also lead to flame wrinkling that can contribute to and enhance the Darrieus-Landau instability. If no stabilization occurs, the flame surface continues to grow due to the wrinkling effect, the burning velocity increases, and hence, a transition to a turbulent flame may occur.

A parameter that can characterize the mixture regarding the thermal and molecular diffusivity, and hence, help to analyse how susceptible a mixture is to thermal-diffusive instabilities, is the Lewis number given by equation (3.11), where α is the thermal diffusivity and $\mathscr{D}$ is the molecular diffusivity.

$$Le = \frac{\alpha}{\mathscr{D}}. \tag{3.11}$$

If $Le < 1$, the flame will be susceptible to these instabilities, but if $Le > 1$ the flame may actually be stabilized due to the thermal-diffusive effect, and even suppress Darrieus-Landau instability, keeping the flame surface smooth and stable [56]. Furthermore, thermal-diffusive cells can be moderated by the positive stretch of the outwardly propagating flame [57].

In the work of Tse et al. [55], with $\mathrm{O_2}$ and $\mathrm{H_2}$ mixtures, this instability was delayed by using He as the diluent that increases the Lewis number and also the flame thickness, which further delays the formation of cells. Besides He, $\mathrm{N_2}$ was also used as the diluent and it was observed that the suppression of the cells was harder to achieve with this diluent. It was also found that for the $\mathrm{N_2}$ mixture the flame was smooth for the rich mixture while instabilities developed for the lean mixture. For example, for 3 atm $\mathrm{H_2}/Air$ flames, only flames with λ smaller than 0.7 are not severely affected by thermal-diffusive instability [58].

Besides the mixture composition, another aspect that will influence the appearance of this instability is the mixture's initial pressure. As the pressure increases, the thermal-diffusive instability occurs over an increasing range of λ, spanning from the entire fuel-lean regime to part of the moderately fuel-rich regime [59].

Another source of flame instabilities that can occur in a confined chamber such as ESTHER's driver are acoustic waves. These waves can reflect on the walls and obstacles and will interact with the flame front. This phenomenon does not always result in the destabilization of the flame, it can actually act as a stabilizing agent, but it will influence the flame properties and the same happens the other way around, the flame can influence the properties of the acoustic wave. If the amount of energy acquired by the compression wave in the reaction zone when passing through flame exceeds that which it dissipates throughout the remaining propagation path, then the compression wave is amplified on the combustion zone [60].

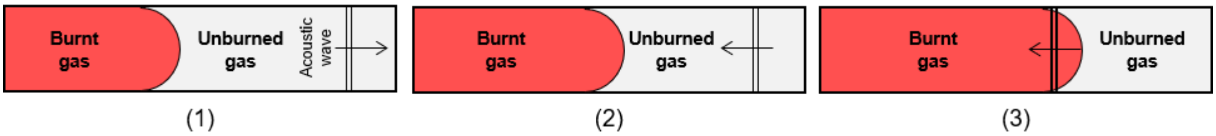

Figure 3.6: Accoustic wave and flame front interaction inside vessel.

In figure 3.6 a simple representation of a premixed flame propagating in a confined chamber is given. At instant (1), an acoustic wave is travelling towards the right end of the chamber and once it reaches the end tap, it reflects and starts to travel towards the flame as it can be seen at instant (2). Once the acoustic wave reaches the flame front, at instant (3), two things may happen:

- The acoustic wave can be amplified due to the high energy release of the reaction zone.
- The acoustic wave is not amplified in the reaction zone since the energy is dissipated throughout the remaining propagation path.

This acoustic wave will continue to propagate towards the burnt gas and will have a periodic motion from the left to the right of the chamber, and depending on the geometry and the gas initial conditions, this acoustic wave can pass through the combustion zone and disturb the flame more than once.

Acoustic waves interactions with flame fronts in confined vessels have been studied by Leyer and Manson [61], in vented enclosures by Tamani and Chaffee [62] and van Wingerden and Zeeuwen [63]. Usually, they are generated when the flame front reaches an obstacle, like walls, or due to ignition if the energy deposition is big. Acoustic instabilities may be important for relatively slow flames in enclosures that are free of obstacles [56], the case of ESTHER combustion driver.

On the work of Laderman et al. [64], an expression relating the acoustic waves pressure amplitude is given. This expression was obtained under the premise that a disturbance in the flame with a surface area of A_f changes the heat release rate by a δQ, and pressure waves are generated at the flame front increasing the pressure from p to $p + \delta p_{ac}$. This relation can be given by equation (3.12), where δQ

depends on the density of the unburned mixture (ρ_{unb}), the heat release per unit of mass (q), the normal relative flame speed (S_L^0), and the flame area (A_f).

$$\delta p_{ac} \sim \delta Q = \delta\left(\rho_u \cdot S_L^0 \cdot A_f \cdot q\right). \tag{3.12}$$

One solution to reduce and even eliminate such pressure waves is to use a special lining material on the inner surface of the chamber like it was shown in [65] and [62].

3.1.2.3 Turbulent flame

When the previous instabilities start to grow on the flame front, it can get wrinkled and develop into a cellular flame front, which can cause turbulent combustion.

The main effect that turbulence will have on the flame is the increase of the burning velocity, which is closely connected to the intensity of the turbulence.

In this type of flow, eddies will develop, and its distribution will have a stochastic nature [52]. The length scale of the largest eddy can be used to define the integral scale of the turbulent flow l_0, while the smallest scale of a turbulent flow is usually referred to as the Kolmogorov length scale, l_k.

The effects that turbulence has on premixed combustion can be described using the commonly called Borghi diagram [66]. In this diagram, there are five combustion zones, where the line $Re_t = 1$ separates the laminar ($Re_t < 1$) from the turbulent regime ($Re_t > 1$). Re_t is the turbulent Reynolds number, defined by equation 3.13, where u' is the turbulent fluctuation velocity.

$$Re_t = \left(\frac{u'}{S_L^0}\right)\left(\frac{l_0}{\delta_f}\right) \tag{3.13}$$

3.1.2.4 Deflagration to detonation transition

From figure 3.2, one of the possible sequences of events from a turbulent flame can lead to a deflagration to detonation transition. Although deflagrations will be the most probable mode of combustion, detonations can also occur depending on the initial conditions, vessel geometry, and fuel. A detonation is a supersonic combustion wave across which the pressure and density increase [67].

There is more than one mechanism responsible for this transition, but the substantial increase in the total burning rate associated with the flame-upstream flow interaction will have the biggest impact [67]. The motion produced in the unburned gas ahead of the flame will result in an unsteady and turbulent region, that once is reached by the flame, will cause major stretching and flame distortion. This distorted flame appearance and dynamics will depend mostly on the nature of the flame dynamics disturbances, like the length scales and intensity of the turbulence in the upstream flow [67]. This feedback process can set the stage for the transition to a detonation.

Summarizing, the sequence of events that can occur in a deflagration to detonation transition are:

- Smooth flame with a laminar flow upstream;
- Wrinkling of flame and instability of the upstream flow;

- Upstream flow becomes turbulent and a corrugated flame develops;
- Pressure waves ahead of the turbulent flame are generated;
- Local explosions of vortical structures within the flame occur;
- The flame transits from deflagration to a detonation.

One of the ways that was used to study DDT inside chambers without obstacles, was by analysing the run-up distance that the flame takes to transit to a detonation [68] [69] [70] [71] [72]. This data shows that the detonation run-up distance decreases with increasing pressure and temperature, and in some of these works, an increasing tube diameter seemed to increase the run-up distance. It was also registered that the onset of detonations occurred at the end of the tube, where the mixture is already pre-compressed. But although this transition will follow some patterns, a DDT is a stochastic event, so the transition point and time is not always the same for the same initial conditions.

Besides this set of events, another phenomenon that occurs in every DDT is a tulip flame. This type of flame is often observed in closed or semi-closed tubes, and its appearance can be attributed to viscosity, flame front interaction with pressure wave, hydrodynamic instabilities, vortices, or the Darius Landau instability [73]

3.2 Experimental Campaign

Now that the necessary background was introduced, this section presents the experimental campaign of ESTHER's combustion driver, that took place at the Hypersonic Plasmas Laboratory.

This experimental campaign's main goal is to prove the performance of the driver and understand if it fulfils the requirements of repeatability, reliability, and availability. Besides this, it is also possible to study high-pressure combustion in confined vessels and understand the influence that the initial fill parameters have on the compression ratio, flame velocity, acoustic waves amplitudes, and more.

First, a description of the experimental setup is given. This includes the driver and ignition system set-up, followed by the gas filling system, and the used instrumentation for data acquisition and measurements. After this, the used methodology is presented, followed by the obtained results and respective discussion.

A total of 57 shots were performed during this campaign.

3.2.1 Experimental Set-up

3.2.1.1 Driver and ignition system

In figure 3.7, a representation of the driver and ignition system set-up is given.

With the identifiers from (1) to (5), the main components of the driver are given. On the left side of the driver, the channel where the ignition occurs for focused ignition is presented, with a length of 144 mm and an inner diameter of 20 mm. This channel is sealed on the left by an optical sapphire window so that the laser beam can reach the combustible mixture inside the chamber.

The main combustion chamber has a cylindrical shape, with a length of 1601 mm, an inner diameter of 200 mm, and chamber walls with a thickness of 20 mm. On the right, the inlet and output gas ports are represented, followed by the Kistler gauge that will record the pressure evolution along time.

It can also be seen that the ignition channel is not perfectly centred. This was done to avoid pressure waves coalescing, which could result in strong stress and extra unnecessary acoustic effects that would influence the ideal operation of the driver.

On the left and with the identifiers from (a) to (i), the ignition system is depicted. It consists of a high-power Nd:YAG laser (a), with a pulse wavelength of 1064 nm, 5 ns, and 200 mJ. The alignment of the laser beam is done with the help of a red diode laser, depicted by (b). The Nd:YAG laser beam is reflected by two 45º mirrors, to change the beam height and azimuthal deviation, and passes through a half-wave plate, that polarizes the light, and a beam splitter cube, that will divide the beam as a function of the polarization. After this, it will enter the chamber via the sapphire window, and hence, ignition is possible. For focused ignition, a lens is positioned before the sapphire window to control the focal point.

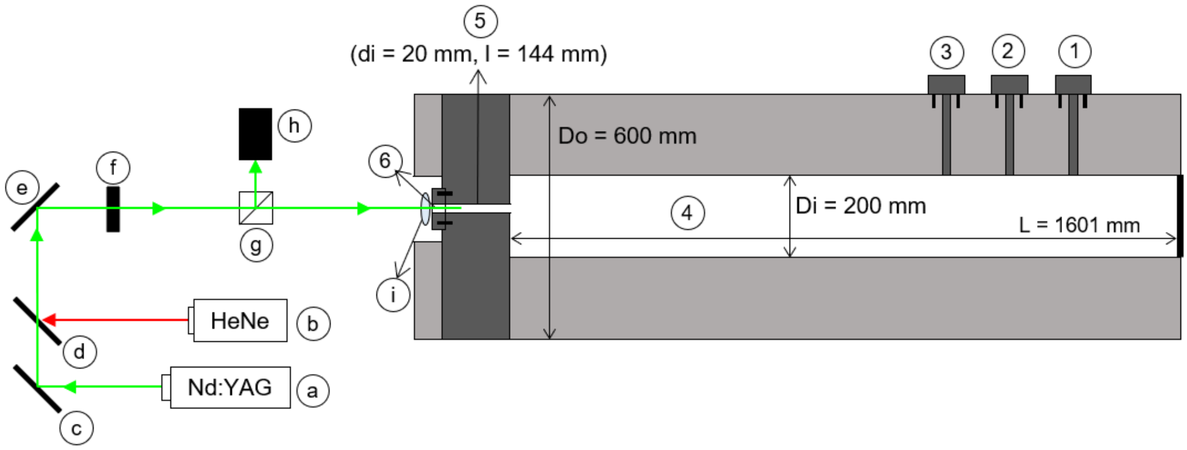

Figure 3.7: Ignition system and driver set-up. (1) Kistler gauge; (2) Gas output port; (3) Gas input port; (4) Combustion chamber; (5) Ignition channel; (6) Sapphire optical window; (a) High-power Nd:YAG laser 1064 nm 5 ns 200 mJ; (b) Red diode laser; (c-e) 45º mirror; (f) Half-wave plate; (g) Beam splitter cube; (h) Beam dump; (i) Bi-convex focusing lens 100 mm.

3.2.1.2 Gas filling system

The gas filling system was designed to supply an arbitrary mixture of $\mathrm{He/H_2/O_2}$ with a filling pressure of up to 100 bar [46]. This system represented in 3.8, has the following most important features:

- The filling is carried by 200bar gas bottles, sequentially. First $\mathrm{O_2}$, second He, third $\mathrm{H_2}$ and finally He. With this filling sequence it is possible to flush $\mathrm{O_2}$ and $\mathrm{H_2}$ with He from the gas lines, and also to minimize the time $\mathrm{H_2}$ is present outside in the gas filling system by injecting it at the end of the sequence and hence, minimizing liabilities.

- The H_2 lines are separated from the other gas lines and are controlled with the use of pneumatic valves.
- Besides H_2, He and O_2 gas lines, an independent gas supply line of N_2 is available for flushing and rinsing of the combustion chamber.
- Existence of a high-pressure zone, rated at 1.8kbar, with a system of valves that can block waves traveling up into the gas supply lines. These valves have a one-way system so that upstream reflux from gases near the combustion chamber does not reach the bottle storage zone.
- Individual mass flow controllers that allow the control to be done by filling volumes.
- High-pressure valves near the combustion chamber, that allow an alternative filling control scheme with partial pressure reading before the ignition.
- The control system is automated and can be done remotely in the control bunker with the use of a Programmable Logic Controller (PLC) with an additional layer using the EPICS control system.
- Gas leakage detection system for H_2, and O_2 reduction, in the experimental hall and gas bottle areas.

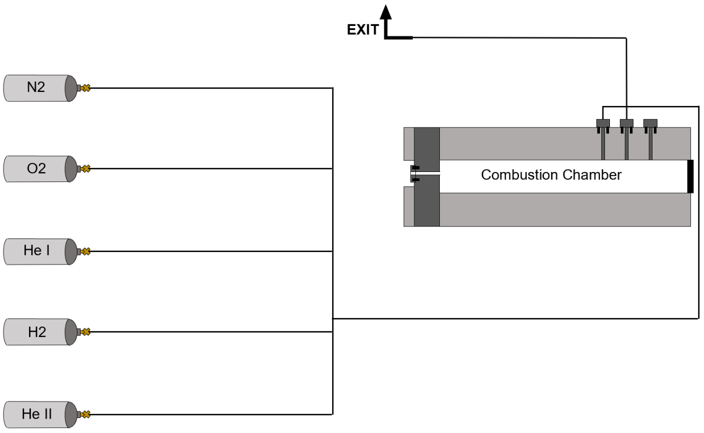

Figure 3.8: Simplified gas filling system layout.

3.2.1.3 Data acquisition

The combustion process can be characterized by the pressure evolution measured with a piezoelectric pressure transducer, a ballistic Kistler gauge. The sensor is located on the third port of the combustion chamber, represented in figure 3.7, and is protected with a heat shield system. The signal from the sensor is further amplified with a charge amplifier and recorded in a digital storage oscilloscope.

3.2.2 Methodology

With the previous experimental campaign of the scaled bombe [46], it was possible to obtain some data and experience to understand some important key points and cautions when dealing with hydrogen high-pressure combustion. Taking into account the necessary safety measures, a gradual methodology was implemented:

The first shots would be performed at lower filling pressures (10bar) and with the optimal mixture ratio to suppress instabilities obtained from the previous test campaign, being that 8:2:1.2 of $\mathrm{He/H_2/O_2}$.

If the obtained results showed that the combustion was stable, repeatability would be studied and other filling parameters(% He, λ), and laser focus, or waiting time, would be varied. If the results showed that the combustion was not stable, the concentration of $\mathrm{O_2}$ would be increased, since it was shown on the previous test campaign that increasing the amount of $\mathrm{O_2}$ would suppress the acoustic instabilities. The concentration of $\mathrm{O_2}$ would be increased until stable combustion was achieved.

In the scenarios where the combustion regime was stable and with satisfactory results, the filling pressure would be increased by 10 bar, and this process would be repeated until stable combustion for the new filling pressure would be achieved.

3.2.3 Results and discussion

A total of 57 shots have been performed to date. In figure 3.9, a representation of the initial fill parameters of the successful shots and a qualitative representation of the compression ratio is given. Each side of the triangle gives the molar fraction of He, $\mathrm{H_2}$, and $\mathrm{O_2}$. To properly read the data of each point, one has to follow the example given by the black dot and the respective reference line shaded in grey. Besides the molar fractions of each component of the initial gas mixture, the initial fill pressure is given by the colour of each shot circle, where the colour range and respective values are given by the bar on the right. The size of each circle is directly related to the compression ratio obtained on that shot.

The circles represent shots that had a deflagration, with compression ratios smaller than the theoretical values, and the diamonds represent shots where a transition to detonation occurred and the compression ratio reached the maximum values, bigger than 10.

To complement this plot, table 3.1 gives the quantitative range of the filling pressure (p_{fill}), equivalence ratio (λ), and the dilution ratio (D), followed by the compression ratio.

Table 3.1: Range of the initial parameters (p_{fill}, λ, $\%\mathrm{He}$) and obtained compression ratio

	Minimum	Maximum
p_{fill} (bar)	5	100
λ	0.75	2.04
Dilution ratio (D)	3.39	9.02
Compression Ratio	4.97	27.13

The observed distribution of the initial parameters of the performed shots is a direct consequence of the used methodology, where safety was one of the main concerns.

From figure 3.9, the Helium molar percentage is restricted to a range between 54% and 75%. The lower limit is a consequence of the safety precautions, since as the dilution of Helium decreases, the detonation onset increases significantly, as it can be confirmed from the figure, where all of the detonations occurred for the lower Helium dilutions. Lower Helium dilutions were further only used with lower filling pressures, also to avoid stronger detonations.

Besides this, the majority of shots were done with an oxidizer-rich mixture ($\lambda > 1$), since for an oxidizer lean mixture, the final combustion products would still contain hydrogen and the safety of the chamber purge process would decrease.

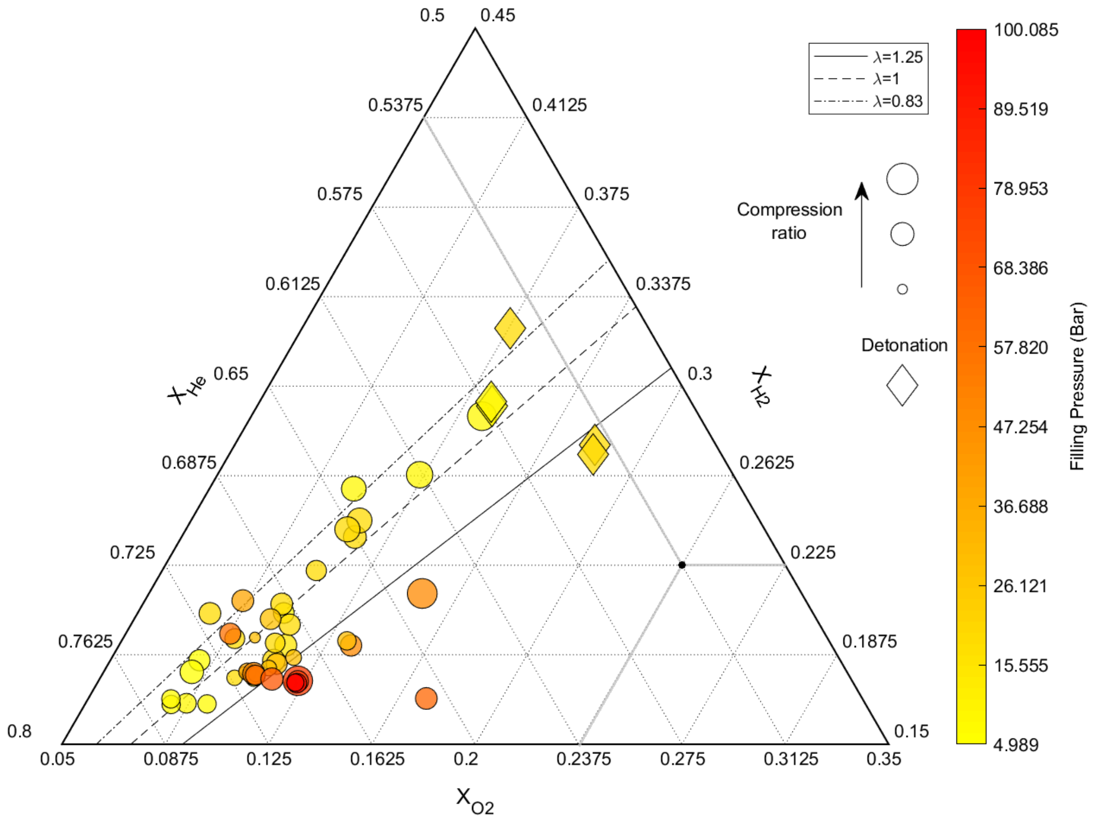

Figure 3.9: Initial filling parameters and qualitative compression ratio of the performed shots.

On these experiences, 3 main input variables can be varied, being that the filling pressure, the equivalence ratio (λ), and the helium percentage. Besides this, it was also possible to choose between focused ignition, or unfocused ignition, which will change the length that the flame needs to travel until it reaches a wall. For these input variables, there is one observable output that is the pressure evolution on the end of the driver. Although only one observable variable is possible, it is a very rich property that can tell a lot about the flow inside the chamber and the phenomena that occur.

3.2.3.1 Deflagration

In figure 3.10, an example of the typical pressure evolution that occurs in a deflagration regime is given.

Besides the pressure evolution, a plot of the mass burning rate ($\dot{m_b}$) is also given. The mass burning rate was obtained from the pressure signal using equation 3.15, taken from [74], that was derived from Lewis and von Elbe [75]. The variables m_{init}, p_{ad}, and p, are the initial mass of gas inside the chamber, the equilibrium adiabatic post-combustion pressure, and p is the instant pressure.

$$m_{\mathrm{b}}(t) = \frac{p(t) - p_{\mathrm{fill}}}{p_{ad} - p_{\mathrm{fill}}} m_{init}. \tag{3.14}$$

$$\frac{1}{m_{init}} \frac{\mathrm{d}m_{\mathrm{b}}}{\mathrm{dt}} = \frac{1}{p_{ad} - p_{fill}} \frac{\mathrm{dp}}{\mathrm{dt}}. \tag{3.15}$$

The shot starts with the laser pulse, which gets registered on the pressure evolution signal because a very powerful electric charge occurs, and it interacts with the Kistler amplifier, registering this perturbation on the pressure signal. The laser pulse moment is denoted as t_0. After the laser pulse, a plasma is formed which further develops into the flame kernel and combustion initiates. Once the flame front travels through the ignition channel and starts entering the main chamber, it will adopt a convex shape, and this can be seen from t_1. This behaviour is translated to the pressure signal, which has an exponential growth at the beginning of the signal. This can also be inferred in the mass burning rate plot. Since the flame surface area continues to increase exponentially, the rate at which the gases are burnt will inevitably increase as well.

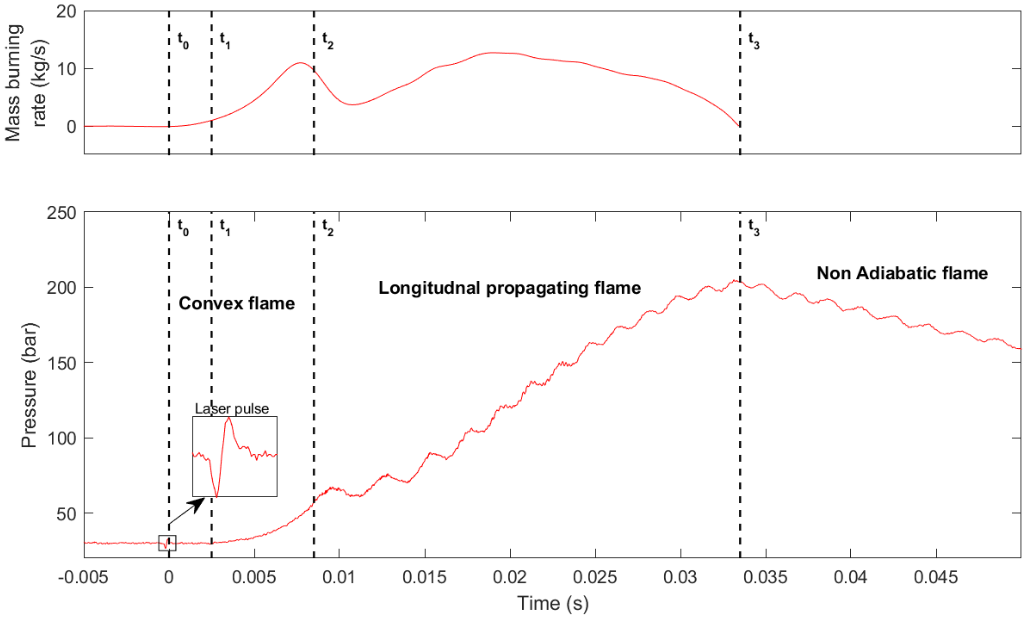

Figure 3.10: Pressure signal and mass burning rate of a deflagration regime flame.

Once the flame reaches the cylindrical walls of the chamber, a sudden decrease of the mass burning rate occurs, a moment is marked by t_2. This occurs once the flame reaches the walls, as the flame surface area is rapidly reduced to the region facing the other end of the chamber. It is also at this moment when the flame reaches the walls, that an acoustic wave is formed. This same behaviour and acoustic wave source has been mentioned several times in the literature [76] [60] [61] [62].

From t_2 to t_3, the flame continues to propagate towards the end of the chamber. From t_2, it is possible to observe that the acoustic wave that was generated when the flame reached the walls, continues to travel back and forth during the entire duration of the combustion process. In section 3.2.3.3 it will be shown that this wave does correspond to an acoustic sound wave travelling along the longitudinal axis of the chamber. Although it is not possible to observe the actual shape of the flame and its dynamics, it is assumed that after the convex shape and likely finger shape, the flame acquires a planar/quasi planar front like it was shown in experimental campaigns from the literature. However most of these experimental campaigns were performed at atmospheric or sub-atmospheric pressures, therefore it is not known if the flame dynamics phenomena at high pressures will remain homogeneous. Nevertheless, an effort was made to interpret the obtained data.

The mass burning rate from t_2 to t_3, starts to decrease at first since the flame surface also decreases. But at some point, starts to increase again. This can be due to the fact that the flame area increases significantly due to many instabilities and be in a turbulent regime.

Once the flame front reaches the end of the chamber, the maximum value is registered. Afterwards, the pressure starts to drop due to energy losses on the walls of the chamber, and hence, the process is non-adiabatic.

3.2.3.2 Deflagration to Detonation Transition

Another type of propagation regime that occurred was a deflagration to detonation transition. In figure 3.11 an example of a DDT is given. The initial conditions are an initial filling pressure of 20 bar, a fuel-rich mixture with $\lambda = 0.77$, and a Helium dilution in volume of 54%, one of the lowest of the performed shots.

For this pressure signal, it is not clear how the flame evolution occurs. At t_0, the laser pulse occurs, and approximately 2 ms afterwards, the pressure signal starts to increase, similarly to the deflagration example. From t_1, combustion starts to occur at a very fast pace, and after t_2 a shock wave is formed, marking the transition to a detonation. This is clearly a shock since the compression ratio was around 27. Although it is not possible to know the exact sequence of events that led to this detonation, it was a consequence of the lower helium concentration.

Besides this example, more detonations and on-set of detonations occurred, mainly due to lower Helium dilutions, in figure 3.9.

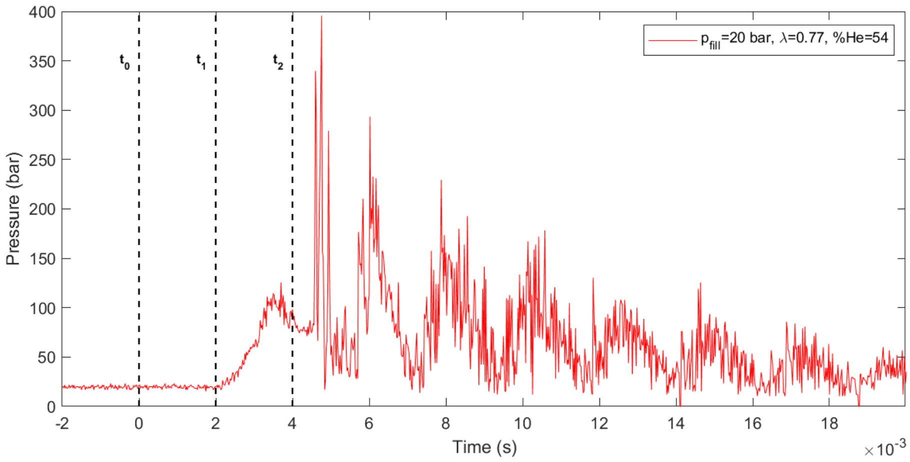

Figure 3.11: Pressure signal of a shot with a DDT.

3.2.3.3 Accoustic analysis

One way to process the results and have a clearer view of the accoustic phenomena that occur inside the chamber is by using the Fast Fourier Transform (FFT) on the pressure signal, a way to convert it into the frequency domain.

Let's consider the shot from figure 3.10. Like it was mentioned, there is an accoustic wave that is born when the flame reaches the cylindrical walls. This accoustic wave frequency may be evidenced using an FFT.

In figure 3.12 the single-sided amplitudes spectrum of the pressure signal in figure 3.10 is presented, where the frequencies that have a bigger representation are between 400Hz and 600Hz.

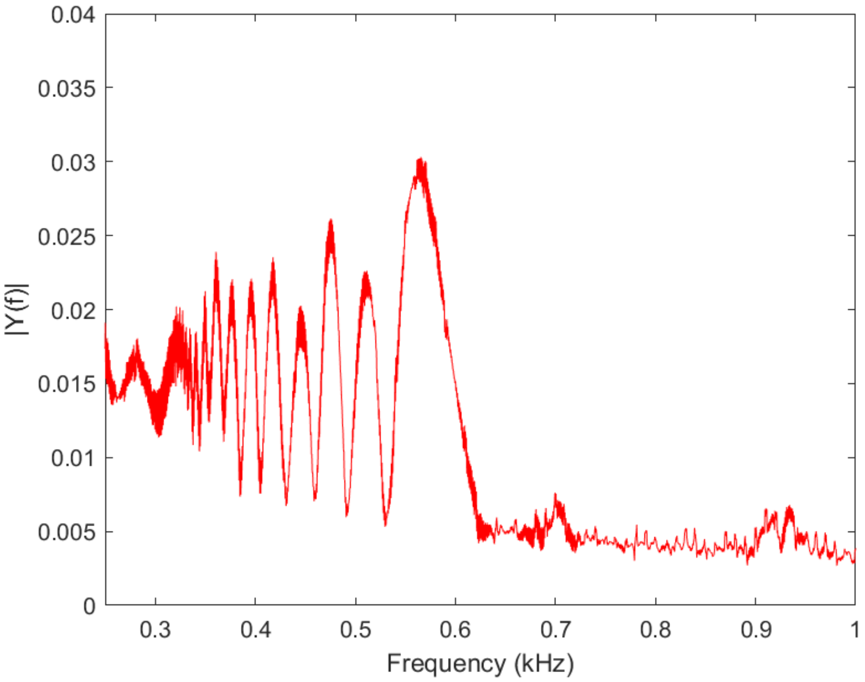

Figure 3.12: Single sided amplitudes spectrum of deflagration shot.

Considering that the efficiency of this shot in terms of compression ratio was around 70% if we multiply this efficiency by the adiabatic flame temperature (3244 K) we get the expected combusted gas temperature (2270 K). Using the heat capacity ratio from the adiabatic combustion ($\gamma_b = 1.2857$) and the specific gas constant of this mixture ($R = 1302 Jkg^{-1}K^{-1}$), the velocity of sound of the burnt gas is $a_b = 1949 m/s$.

The natural frequencies of cylindrical chambers are given by equation 3.16 and were derived by Draper in [77], where n denotes different modes or harmonics. The term $\beta^2/\pi d_i^2$ is related to the radial modes and can be ignored since for ESTHER's combustion chamber $L >> d_i$ and the longitudinal modes will be predominant.

$$f = a\sqrt{\frac{\beta^2}{(\pi d)^2} + \frac{n^2}{(2L_{chamber})^2}} = \frac{a}{2L_{chamber}}n \qquad , n = 1, 2, ... \tag{3.16}$$

Taking equation 3.16, the mentioned values, and the lenght of the chamber ($L = 1.601m$) into account, we obtain a fundamental frequency ($n = 1$) of $608Hz$. Looking at the Fourier transform in figure 3.12, the fundamental frequency obtained is indeed one with the highest amplitudes.

The fact that lower frequencies also have big amplitudes is due to the fact that when combustion is still occurring, the gas will be composed by the burnt gas and the unburned gas that will have a lower speed of sound, and hence, the frequency of the waves that travel through the chamber when the gas is not completely burnt will have lower frequencies.

Another way to calculate the frequency of the accoustic waves is by using the short-time Fourier transform, where the signal is divided by sections in the time domain, and the Fourier transform of each section is calculated. Using this method is possible to see the frequency evolution over time.

In figure 3.13, another example of a shot is given, with $p_{fill} = 80bar$, $\lambda = 1.39$, and $\%\text{He} = 70$, with unfocused ignition. With the focused ignition, the experimental set-up would include a lens like the one on figure 3.7, and for the unfocused, the lens would be removed. This would change the ignition source from a single point high energy point to a beam that would cross the chamber, something proven in [78], making the flame front radial instead of longitudinal.

With this type of ignition, the longitudinal accoustic waves are also present, but the location and time at which they appear are not clear since the flame shape is unknown. Nevertheless, it is assumed that it is when the flame reaches the end taps.

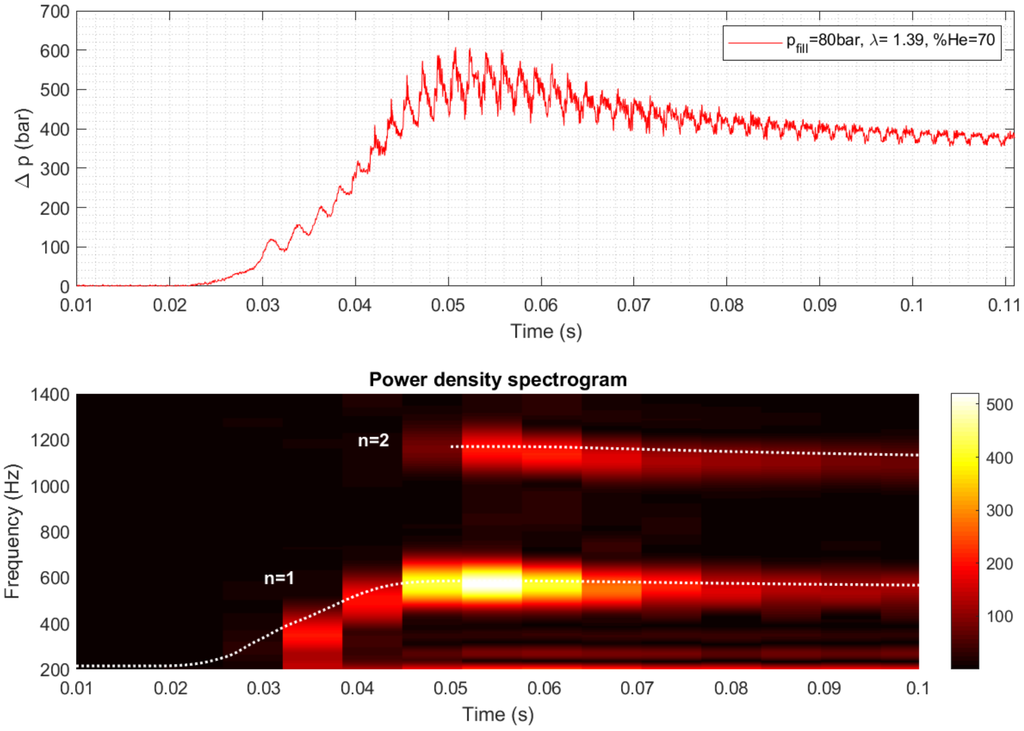

Figure 3.13: Short time Fourier transform of deflagration shot.

Bellow the pressure profile, the short-time Fourier transform is given. On top of it, two lines are presented. These lines are the fundamental and first harmonic frequencies of the chamber. To calculate these frequencies, the average speed of sound of the gas was calculated.

To do so, equation 3.14 was used to obtain the time evolution of the burnt mass ($m_b(t)$), using a filtered signal from the pressure ($p(t)$). With the evolution of the burnt mass, it was possible to obtain the evolution of the burnt volume by employing the perfect gas equation of state ($pV = mRT$). It was assumed that the gas density is homogeneous inside the chamber, and a flame temperature of 96% of the adiabatic flame temperature ($T_{ad} = 3109$ and $T_b = 2985K$), to consider the efficiency of the shot.

With the burnt volume, the unburned was calculated by simply subtracting it from the chamber volume.

With the volume ratio of the burnt and unburned gas, it is possible to obtain an average speed of sound. To calculate a_b, $T_b = 2985K$ and $\gamma_b = 1.34$ were used, and for a_{unb}, $\gamma_{unb} = 1.4318$ and the temperature evolution was obtained from the pressure signal.

Knowing the volume ratios and each speed of sound, the average speed of sound was calculated, and the frequency of the longitudinal modes was obtained by using equation 3.16.

The calculated fundamental frequency follows relatively close to the power density spectrum, where the growing wave frequency is very visible.

3.2.3.4 Parameter study

In this section, a comparison between the obtained results of different shots is discussed, and the observed influence of each initial parameter is analysed.

As it has been mentioned, the initial parameters that can be controlled are the molar fractions of each gas mixture component, the filling pressure, the laser mode (focused or unfocused), and besides this, the waiting time before the ignition and after the chamber has been filled. The results that will be analysed are the compression ratio ($C.R.$), average flame speed ($\overline{S}$), average mass burning rate ($\overline{\dot{m_b}}$), and average acoustic wave amplitude ($\overline{p_{ac}}$).

These results were obtained by interpretation of the pressure profile.

The compression ratio ($C.R.$), like it was previously mentioned, corresponds to the division between the peak pressure and the filling pressure.

For $\overline{S}$, the flame path distance divided by the combustion time was used. The considered combustion time corresponds to $t_3 - t_1$ from figure figure 3.10. The time instant after the laser pulse is not considered since it also includes the induction time it takes for the flame kernel to completely develop. Taking into account the mentioned combustion time, for the focused ignition flame path, the length of the ignition channel is ignored since such a small amount of volume, compared to the chamber, does not strongly influence the pressure rise. Hence, the length considered corresponds to the length from the end of the channel until the pressure sensor location.

The average mass burning rates were calculated using the initial mass inside the chamber (m_i), divided by the same combustion time mentioned previously.

For the average acoustic wave amplitude ($\overline{p_{ac}}$), the pressure signal was filtered to smooth all of the accoustic waves, and this new signal was subtracted from the original one, leaving only the acoustic wave amplitude. From here, the local maximums of the absolute value of the processed signal were obtained. The considered time interval was from the start of the combustion time plus three times this value, as it includes the pressure rise plus two times the value it takes to achieve the peak pressure.

Although these calculations are not extremely precise, they provide good values for qualitative analysis.

Firstly, the influence of the Helium percentage is given. In figure 3.14 two shots are compared, both with an initial filling pressure of 50 bar, and an equivalence ratio of 1.4. With a 4% difference of Helium molar fraction, the obtained results are very distinct. The shot with the lowest Helium percentage has a much steeper pressure rise, accompanied by high amplitude acoustic waves that even tend to increase when passing through the region of the flame front as it can be depicted on the peak region. Besides this, the combustion time is much smaller, and hence, the burning velocity is bigger.

The highest diluted shot has a much slower pressure rise, and most likely because of this, the wall losses are greater, and the combustion efficiency is lower compared to the other shot.

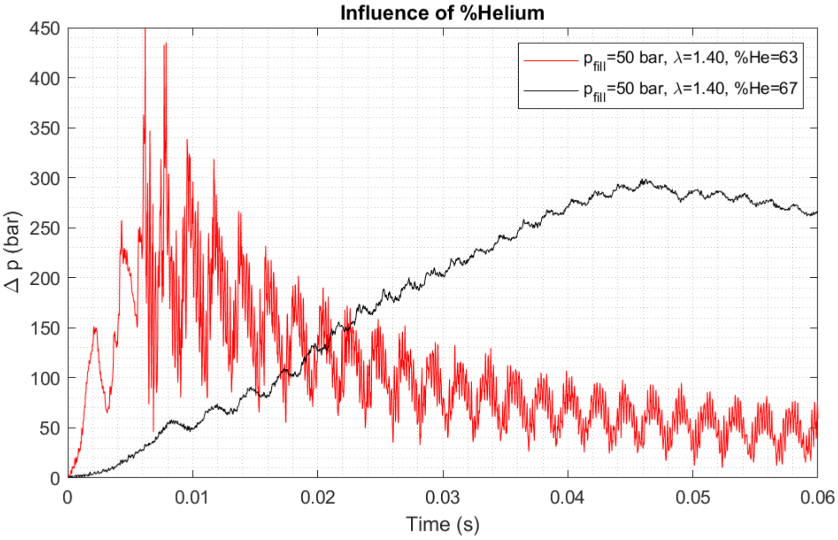

Figure 3.14: Shots comparison varying %He.

Looking at table 3.2, the values for these parameters are given. As predicted, the compression ratio obtained with the lower Helium percentage is higher. This happens since the specific heat of the diluent gas per unit of oxygen concentration increases, and hence the flame propagation decreases as Helium is added [74], resulting in a lower pressure rise with increasing dilution.

After the compression ratio, the average flame velocity is given, and the values obtained have a difference of one order of magnitude, with 259 m/s for the lowest dilution, and 35 m/s for the highest dilution.

The mass burning rate will depend on the burning velocity and flame surface area, but also on the unburned gas density. If the flame velocity is high, the mass burning rate will follow the same behaviour. For the higher diluted mixture, the mass burning rate is around 17 kg/s, and for the other shot, around 131 kg/s. The difference in the order of magnitude is also about one.

Now, analysing the average wave amplitude, with the 4% decrease of Helium dilution, the average acoustic wave amplitude increases approximately 16 times, from 7 to 111 bar. From equation 3.12, we know that the acoustic wave amplitude depends on the heat release. So, as the dilution increases, the total heat release also decreases, and hence, the amplitude of the acoustic waves follows the same behaviour. Besides this, with increasing Helium dilution, some flame instabilities that increase the flame area and consequently the heat release, can be suppressed [55].

Table 3.2: Initial filling parameters and obtained results.

	$p_{fill}(bar)$	λ	D	% He	$C.R.$	$\overline{S}$ (m/s)	$\overline{\dot{m}_b}$ (kg/s)	$\overline{p_{ac}}$ (bar)
Shot 34	50	1.40	5.98	63	9.5	259	131	111
Shot 35	50	1.40	7.05	67	7.1	35	17	7

In figure a new 3.15, a new set of shots is given. This time, the influence that the equivalence ratio has can be analysed. The initial conditions are a filling pressure of 30 bar, a helium dilution around 70%, and three different equivalence ratios, 0.98, very close to the stoichiometric mixture, and two oxygen rich mixtures with 1.20 and 1.24.

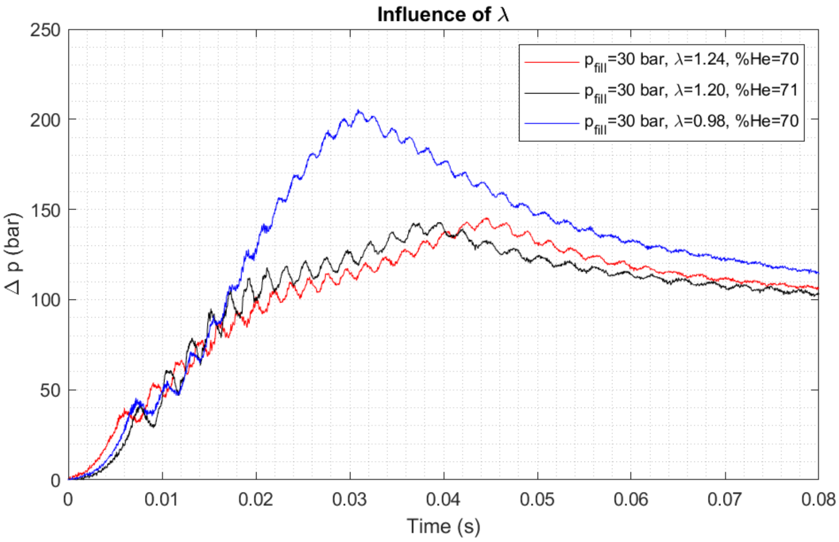

Figure 3.15: Shots comparison varing λ.

The first outcome that pops out is that the mixture that had the highest compression ratio was the one closest to the stoichiometric conditions. For the stoichiometric mixture, the adiabatic flame temperature is the highest, since the energy release is also maximized. The obtained compression ratio was 6.9, and for the fuel-lean mixtures, around 7.75, considering the values from table 3.3.

The average flame velocity was also higher for the mixture with $\lambda = 0.98$, comparing to the two fuel-lean shots. Going back to figure 3.5, this behaviour goes according to previous experiments. If there was a shot with $\lambda < 1$, and hence, fuel-rich, it would be expected that the average flame velocity increased due to the highly diffusive nature of hydrogen. The mass burning rate follows the same behaviour as $\overline{S}$.

Although the mixture with $\lambda = 0.98$ has the highest heat release, it does not seem to have the most energetic acoustic waves. The obtained values for the amplitude of the acoustic waves were relatively similar, and hence, for this set of shots, at 30 bar, the equivalence ratio does not seem to have a great impact on the energy of these waves.

Table 3.3: Initial filling parameters and obtained results.

	$p_{fill}(bar)$	λ	D	% He	$C.R.$	$\overline{S}$ (m/s)	$\overline{\dot{m}_b}$ (kg/s)	$\overline{p_{ac}}$ (bar)
Shot 18	30	1.24	7.49	70	5.9	36	10	4
Shot 17	30	1.20	7.79	71	5.8	44	11	5
Shot 20	30	0.98	6.90	70	6.9	52	13	4

As the pressure increases, λ does have a big influence on the amplitude of the acoustic waves. In figure 3.16, the pressure profiles of two shots with $p_{fill} = 70bar$ and $\%\mathrm{He} = 71$ are given, and in table 3.4 the obtained results.

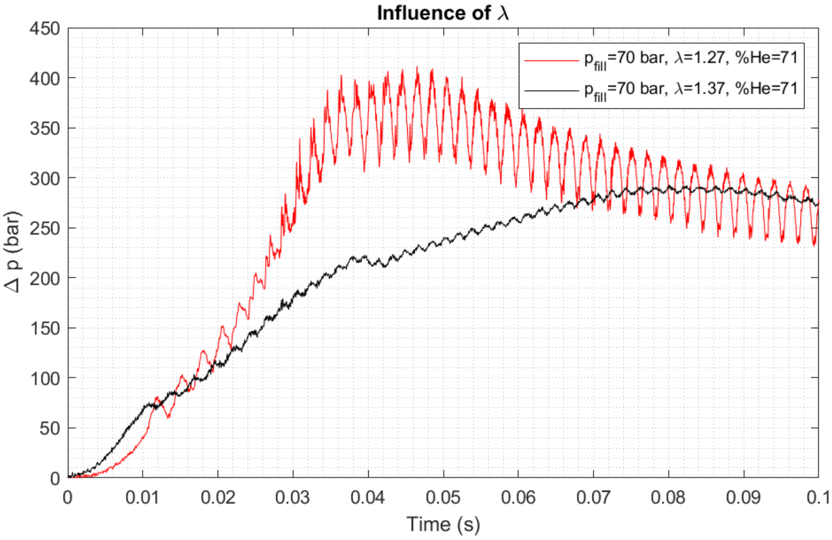

Figure 3.16: Shots comparison varying λ.

The equivalence ratios of the two shots are $\lambda = 1.27$ and $\lambda = 1.37$, both fuel-lean. By looking at the pressure profiles, it is clear that for the highest equivalence ratio, the wave amplitude decreases significantly. The mechanism that promotes this behaviour is not well understood since it can be from the higher energy release rates due to the higher amount of reactants that come with higher pressure, and hence, higher densities. Nevertheless, at high-pressure filling pressures, this behaviour was always observed, and because of that, higher equivalence ratios were used to avoid these high-energy acoustic waves that could transit to detonations. By increasing the amount of $\mathrm{O_2}$, the energy release on the flame front decreased. Besides this, $\mathrm{O_2}$ is a molecule that can store energy efficiently due to the internal vibrational and rotational modes.

With increasing λ, the compression ratio, the average flame speed, and the mass burning speed decrease, for the same reasons mentioned previously.

In figure 3.17, the results of 4 different shots with increasing pressures are presented. The dilution of Helium is 71-72% and the equivalence ratio increases with pressure as a consequence of the considered methodology. From table 3.5, the initial filling parameters and the results are given, with λ starting at 1.11 and going to 1.27 for filling pressures of 20 bar to 70 bar. Nevertheless, even with the increased λ, that was proven to decrease the acoustic wave amplitude, $\overline{p_{ac}}$ increases with p_{fill}, as seen from the

Table 3.4: Initial filling parameters and obtained results.

	$p_{fill}(bar)$	λ	D	% He	$C.R.$	$\overline{S}$ (m/s)	$\overline{\dot{m}_b}$ (kg/s)	$\overline{p_{ac}}$ (bar)
Shot 33	70	1.37	8.01	71	5.2	34.41	13	7.68
Shot 32	70	1.27	8.01	71	7.3	20	21	42

plot and the values of $\overline{p_{ac}}$ on the table. If the equivalence ratios were all similar, the differences in these values would be more accentuated.

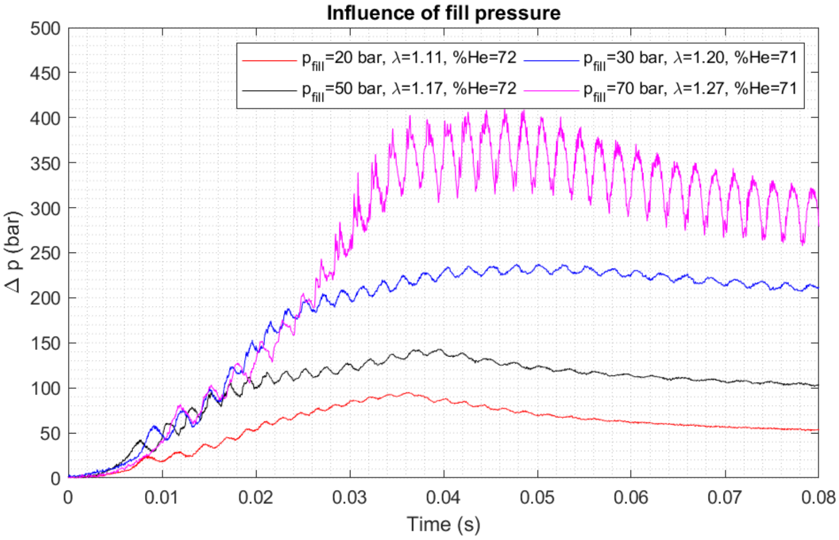

Figure 3.17: Shots comparison varying filling pressure.

Table 3.5: Initial filling parameters and obtained results.

	$p_{fill}(bar)$	λ	D	% He	$C.R.$	$\overline{S}$ (m/s)	$\overline{\dot{m}_b}$ (kg/s)	$\overline{p_{ac}}$ (bar)
Shot 23	20	1.11	8.14	72	5.8	44	7	3
Shot 17	30	1.20	7.79	71	5.8	44	11	5
Shot 29	50	1.17	7.97	72	5.8	32	14	8
Shot 32	70	1.27	8.01	71	7.3	34	21	42

Besides the initial gas conditions, it was possible to change the ignition source from focused ignition, to unfocused. With the focused ignition, the experimental set-up would include a lens like the one on figure 3.7, and for the unfocused, the lens would be removed. This would change the ignition source from a single high energy point source, to a beam that would cross the chamber, something that was evidenced in [78], making the flame front probably radial instead of longitudinal.

Because of this, is expected that the flame propagates mostly radially, and the flame path will be closer to the chamber's inner radius. In figure 3.18 the pressure profile of two shots are given, one for focused ignition and the other for unfocused. For both shots, the initial filling conditions are $p_{fill} = 50bar$, $\lambda = 1.17$, and $\%He = 72$.

The pressure evolution behaviour for the unfocused ignition is clearly different when compared with

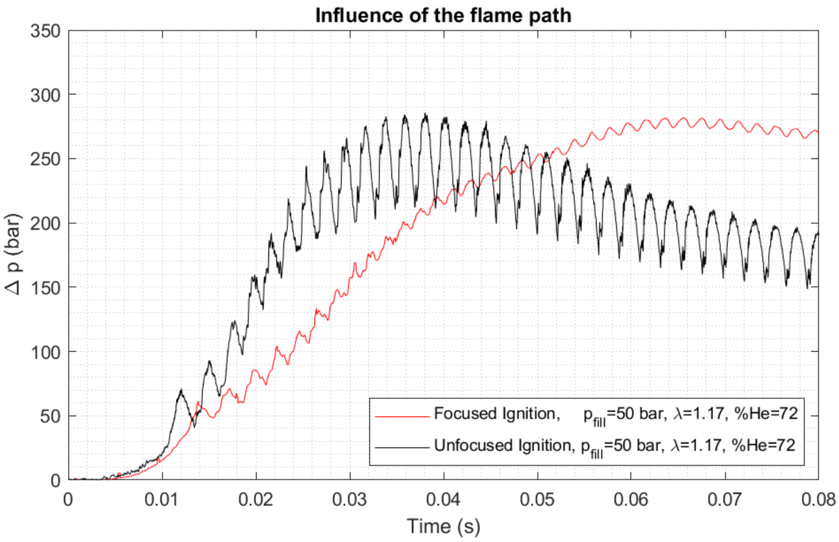

Figure 3.18: Shots comparison varying flame path.

the previous examples, with a more constant rising slope.

The obtained compression ratios are very similar, but that does not apply to the average accoustic wave amplitude.

Although the filling conditions are the same, the resulting accoustic waves have very different amplitudes. The total amount of heat release will be the same, but since the combustion with the unfocused ignition takes less time, the heat release rate for this situation will be greater, contributing to a higher amplitude of the waves, if we consider equation 3.12. Besides this, with the assumed flame shape that will be most likely mainly radial, when the longitudinal wave is travelling back and forth on the chamber, it is always passing through a flame, in contrast with the previous examples where the wave would travel between the burnt and the unburnt gas, and it would only cross the flame front on the interface of these two states, like how it is depicted in figure 3.6.

This example shows that the heat release rate and the flame dynamics play a significant role in the value of $\overline{p_{ac}}$.

Table 3.6: Initial filling parameters and obtained results for different flame paths. (*the flame speed for unfocused ignition was calculated with the chamber radius)

	$p_{fill}(bar)$	λ	D	% He	$C.R.$	$\overline{S}$ (m/s)	$\overline{\dot{m}_b}$ (kg/s)	$\overline{p_{ac}}$ (bar)
Shot 28	50	1.17	7.99	72	6.7	26	11	6
Shot 30	50	1.17	7.97	72	7.3	3*	20	37

3.3 Driver Operability

3.3.1 Performance

One of the main requirements for ESTHER's combustion driver was the ability to have a high performance and achieve high post-combustion pressures, up to 600 bar. This goal was achieved during this experimental campaign and ESTHER's combustion driver performance was proven.

In figure 3.19, the performance range from the highest to one of the lowest-performing shots is given. With the highest performance achieved, it was possible to obtain a post-combustion pressure of 659 bar, slightly higher than the initial requirements. Besides this, it is also possible to operate the driver with pressures below 100 bar if necessary.

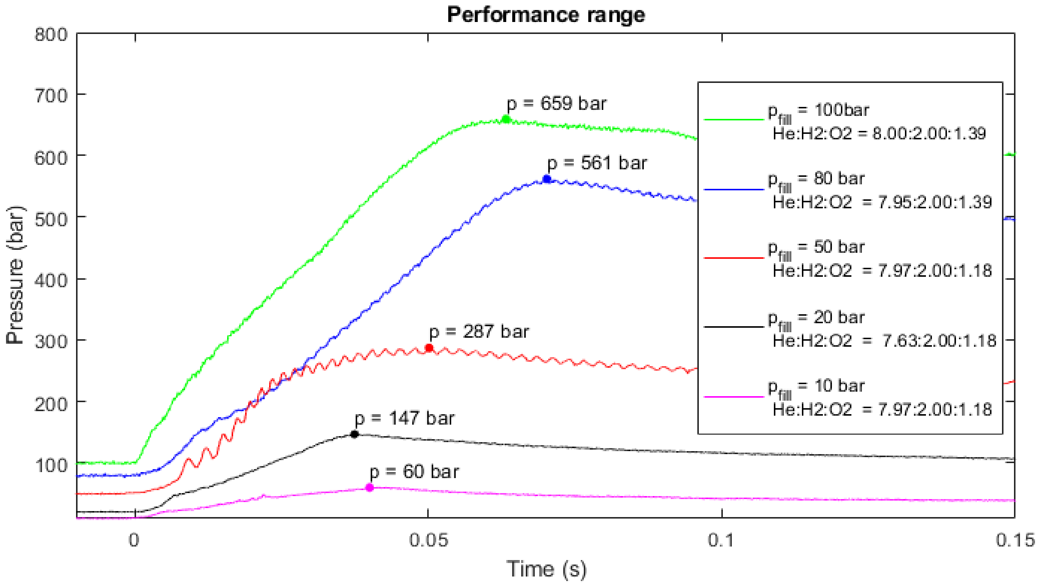

Figure 3.19: ESTHER combustion driver performance range.

The absence of strong accoustic waves, and a variety of performances, makes this set of shots a good representation of the ideal initial conditions for future shock tube operation, where the dilution ratio is around 8, and with increasing pressure, the equivalence ratio has to be increased.

3.3.2 Repeatability

To test the repeatability of the combustion process that took place inside the chamber, some shots were repeated and their signals overlapped to compare the results.

In figure 3.20, an example of this with three shots is given. The initial conditions were $p_{fill} = 10bar$, $\lambda = 0.92 - 0.93$, and $\%\mathrm{He} = 57 - 58$. With a Helium dilution so low, strong accoustic waves were formed, with amplitudes bigger than the filling pressure at some point. By analysing the overlapping of these three shots, it is possible to obverse that even these very strong accoustic waves are repeatable. Besides the accoustic phenomena, the compression ratio is also very close. The values when the pressure is decreasing differ, but because the piezoelectric Kistler gauge is not tailored for accurately measuring decreasing pressures.

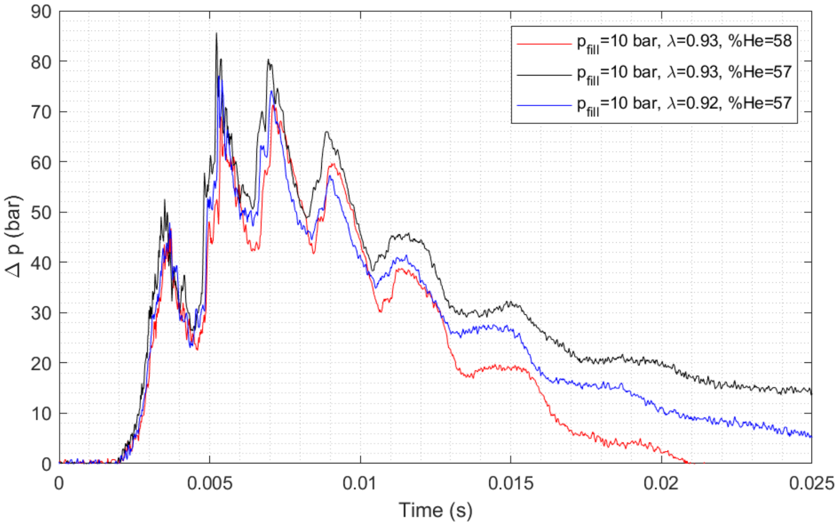

Figure 3.20: Shots repeatability.

Chapter 4

High pressure combustion: Numerical study

In this chapter, a numerical study of high-pressure combustion is given. Using the spark code, 2D axisymmetric simulations with $\mathrm{He/H_2/O_2}$ combustion of a freely expanding flame will be studied. The main focus of this study will be the laminar premixed flame regime and the respective laminar flame speed. Nevertheless, turbulence will also be discussed.

Firstly, the governing equations that are used in the numerical study will be presented. These are followed by the numerical setup employed on the simulations, which includes the description of the CFD solver, the flow initialization, a mesh independence study, and a brief discussion of some numerical issues.

To finalise the chapter, the obtained results are given and discussed.

4.1 Governing equations

4.1.1 Conservation equations

In a reacting flow like the case of combustion, the process can be described through the conservation equations of fluid dynamics coupled to a kinetic model.

Non-reacting flows are described by three main conservation equations of mass, momentum, and energy. In a two-dimensional compressible flow, these equations contain four primitive variables which are density, the velocities in the two directions, and the energy or temperate. To model a chemically reacting flow, the mass conservation equation has to be solved for every chemical species involved to obtain each mass fraction.

These partial differential equations are an extension of classical Navier Stokes equation and can be generically given by equation 4.1, where ρ is the total gas density, **U** the gas velocity vector, E the gas total energy, and c_i each chemical species mass fraction. On the left-hand side, the first term of the equation corresponds to the transient term of $\rho\Phi$, while the second is the convective term flux. On the right-hand side, J_Φ is the dissipative flux of Φ, and Ω_Φ is the contribution of source terms that can result in the production or destruction of the conservative quantity Φ.

$$\frac{\partial}{\partial t}(\rho\Phi) + \nabla \cdot (\rho\Phi\mathbf{U}) = \nabla \cdot J_\Phi + \Omega_\Phi \quad \text{with} \quad \Phi = \{c_i, \mathbf{U}, E\} \tag{4.1}$$

The general conservative equations for mass, chemical composition, momentum, and energy are presented in the following sections. In these conservative equations, the enthalpy and pressure are dependent on the primitive variables through two state equations, which are presented in appendix B.3 and B.2.

4.1.1.1 Mass conservation

Starting with the mass conservation of each species, the primitive variable considered is c_i, and hence, equation 4.1 can be rewritten as equation 4.2, where the diffusion flux $\boldsymbol{J}_i$ of the species i due to mass fraction gradients can be given by Fick's Law that will be presented in section 4.1.2. Besides this term, $\dot{\omega}_i$ stands for the production or consumption rate of the species i due to chemical processes.

$$\frac{\partial\left(\rho c_i\right)}{\partial t} + \boldsymbol{\nabla} \cdot \left(\rho c_i \boldsymbol{U}\right) = -\boldsymbol{\nabla} \cdot \boldsymbol{J}_i + \dot{\omega}_i \tag{4.2}$$

Although the unburned gas ahead of the flame is in chemical equilibrium and its composition remains constant, once the flame front reaches this gas, the fuel will react with the oxidizer and chemical non-equilibrium will be present since the gas composition is no longer uniquely defined with two thermodynamic properties, and will depend also on time and the chemical reactions time scales. This process can be modelled via the source term $\dot{\omega}_i$.

A general chemical reaction expression can be given by equation 4.3, where ν_i' and ν_i'' represent the stoichiometric coefficients of the reactants and products X_i, respectively, k_f and k_b represent the rate constant for the forward and backward process of the reaction rate.

$$\sum_i \nu_i' X_i \underset{k_b}{\overset{\mathrm{k}_f}{\rightleftharpoons}} \mathrm{w} \sum_i \nu_i'' X_i . \tag{4.3}$$

In equation 4.4, the net rate of formation of species i is given, where $[X_i]$ is the number of moles of species i per unit of volume of the mixture.

$$\frac{\mathrm{d}\left[X_i\right]}{\mathrm{d}t} = \sum_r \left(\nu_{ir}'' - \nu_{ir}'\right) \left[k_{f_r} \prod \left[X_i\right]^{\nu_{ir}'} - k_{b_r} \prod \left[X_i\right]^{\nu_{ir}''}\right] . \tag{4.4}$$

Considering the previous equations, the rate of creation or consumption of each chemical species $\dot{\omega}_i$ can be given by equation 4.5, where M_i is the molar mass of species i.

$$\dot{\omega}_i = M_i \frac{\mathrm{d}\left[X_i\right]}{\mathrm{d}t} = M_i \sum_r \left(\nu_{ir}'' - \nu_{ir}'\right) \left[k_{f_r} \prod \left[X_i\right]^{\nu_{ir}'} - k_{br} \prod \left[X_i\right]^{\nu_{ir}''}\right] \tag{4.5}$$

In Appendix C, models for the chemical rate constants are presented.

Although the mass of each species may change, the total mass of the system remains constant. This is ensured by the global continuity equation given by 4.6, where we need to account that ρ is equal to the sum of each partial density (ρ_i) of all species. From ρ_i it is possible to obtain c_i by dividing it by the total gas density ρ.

$$\frac{\partial \rho}{\partial t} + \nabla \cdot (\rho v) = 0 \tag{4.6}$$

4.1.1.2 Momentum conservation

For the momentum conservation equation, Φ will be $\boldsymbol{U}$, the velocity vector, and we get equation 4.7, where $[\boldsymbol{\tau}]$ is the viscous stress tensor.

$$\frac{\partial (\rho \boldsymbol{U})}{\partial t} + \boldsymbol{\nabla} \cdot (\rho \boldsymbol{U} \otimes \boldsymbol{U}) = \boldsymbol{\nabla} \cdot [\boldsymbol{\tau}] - \boldsymbol{\nabla} p \tag{4.7}$$

With this equation, it is assumed that the flow moves with a global velocity $\boldsymbol{U}$, instead of using a velocity vector for each species that would increase greatly the computational cost. This assumption is valid for mixtures which contain species with similar mass.

4.1.1.3 Energy conservation

For the total energy conservation equation, the primitive variable of interest is E. In equation 4.8, the resulting expression is given, where $\boldsymbol{\nabla} \cdot (\boldsymbol{U} \cdot [\boldsymbol{\tau}])$ is the viscous forces work, $\boldsymbol{\nabla} \cdot (p\boldsymbol{U})$ the work done by pressure forces, and Ω_{tot} the energy source term.

$$\frac{\partial (\rho E)}{\partial t} + \nabla \cdot (\rho E \boldsymbol{U}) = \boldsymbol{\nabla} \cdot (\boldsymbol{U} \cdot [\boldsymbol{\tau}]) - \boldsymbol{\nabla} \cdot \boldsymbol{q} - \boldsymbol{\nabla} \cdot (p\boldsymbol{U}) + \Omega_{\text{tot}} \tag{4.8}$$

The heat flux vector $\boldsymbol{q}$ is given by equation 4.9, where $\boldsymbol{q}_C$ is the conduction heat flux, and $\boldsymbol{q}_D$ accounts for transport of energy by diffusion, where h_i is the enthalpy of species i.

$$\begin{aligned} \boldsymbol{q} &= \boldsymbol{q}_C + \boldsymbol{q}_D \\ &= \boldsymbol{q}_C + \sum_i J_i h_i \end{aligned} \tag{4.9}$$

4.1.2 Transport

For each conservation equation, there is one dissipative flux term, each associated with transport phenomena. These fluxes are essential to model the transport of mass, momentum, and energy through the gas.

For the mass conservation equation, Fick's Law can model the diffusion flux of species i due to mass fraction gradients, and it is given by 4.10, where $\mathscr{D}_i$ is the diffusion coefficient of species i, and it will be given by the transport model used.

$$\boldsymbol{J}_i \equiv \rho_i \boldsymbol{U}_i = -\rho \mathscr{D}_i \boldsymbol{\nabla} c_i \tag{4.10}$$

When considering the momentum conservation equation, the viscous stress sensor $[\tau]$ is the dissipative flux term. If we consider the gas mixture to behave as a Newtonian fluid, $[\tau]$ in 4.7 can be modeled with Stokes' law of friction, given by 4.11, with μ being the dynamic viscosity of the mixture, and $[\mathbf{I}]$ the identity matrix.

$$[\tau] = \mu\left(\nabla\mathbf{U} + (\nabla\mathbf{U})^{\mathrm{T}}\right) - \frac{3}{2}\mu(\nabla\mathbf{U})[\mathbf{I}] \tag{4.11}$$

For the energy equation, the conduction heat flux term is $\boldsymbol{q}_C$, and it can be calculated using Fourier's Law of heat conduction, given by 4.12, and where the parameter κ is the thermal conductivity coefficient.

$$\boldsymbol{q}_c = -\kappa\boldsymbol{\nabla}T \tag{4.12}$$

4.1.3 Wilke transport model

In this work, the transport model developed by Wilke [79] will be used to model the transport coefficients from the diffuse terms of each conservation equation. This study consists on the application of kinetic theory to the first order Chapman-Enskog relation, a computationally expensive model derived from the Boltzmann equation. In this approximation, it is assumed that all interactions have the same cross-section and inter-species interactions are omitted.

A general equation for viscosity, μ, and thermal conductivity, κ, as a function of mole fractions, is given by Wilke's semi-empirical mixing rule of a weighted sum of the species individual μ and κ, given by equations 4.13, where ϕ_{ij} is named scaled factor and x_i is the mole fraction of species i.

$$\mu = \sum_i \frac{x_i\mu_i}{\phi_{ij}} \quad \text{and} \quad \kappa = \sum_i \frac{x_i\kappa_i}{\phi_{ij}} \tag{4.13}$$

The weight factor ϕ_{ij} is given by equation 4.14, where $\mathcal{M}_i/j$ corresponds to the species molar mass.

$$\phi_{ij} = \sum_j \frac{x_j\left[1 + \sqrt{\frac{\mu_i}{\mu_j}}\left(\frac{M_j}{M_i}\right)^{\frac{1}{4}}\right]^2}{\sqrt{8\left(1 + \frac{M_i}{M_j}\right)}} \tag{4.14}$$

To compute each species viscosity, Blottner´s curve fitting model is used [80]. This expression is given by equation 4.15, where A_i, B_i, and C_i are curve fit coefficients for each chemical species, and T is the translational temperature of species i.

$$\mu_i\left(T\right) = 0.1\exp\left(C_i\right)T\left(A_i\ln T + B_i\right) \tag{4.15}$$

To obtain the thermal conductivity of each species, κ is determined using the generalized Eucken's relation [81], given in equation 4.16 for the translational energy mode, where c_{v_i} is the specific heat at constant volume of species i.

$$\kappa_i = \frac{5}{2}\mu_i c_{v_i} \tag{4.16}$$

The diffusion coefficient is assumed to be constant for all species and it is given by equation 4.17, where ρ is the mixture's density, C_p is the mixture total specific heat, and Le is the Lewis number, also assumed to be constant for all species.

$$\mathscr{D}_i = \mathscr{D} = \frac{Le\kappa}{\rho c_p} \tag{4.17}$$

4.2 Numerical Set-up

In this section, a description of the numerical setup is provided.

4.2.1 CFD Solver

The software used to develop this work is SPARK, the Software Package for Aerothermodynamics, Radiation and Kinetics [82], a CFD code maintained at the University of Illinois at Urbana-Champaign and Instituto de Plasmas e Fusão Nuclear (IPFN).

SPARK is coded in Fortran 03/08, using object-oriented programming. The software is capable of performing simulations in Euler or Navier-Stokes compressible flows in 0D (temporal relaxation), 1D (post-shock relaxation), or 2D (cylindrical or axisymmetric). To model the gas, it is possible to use frozen or perfect gas, or a chemical reacting mixture, that employs chemical reaction models like the ones presented in appendix C.

The solver uses a second-order cell-centered finite volume formulation, where the employed mesh is structured. For the temporal discretization, both explicit and implicit second-order schemes are available.

This code has been mostly used to simulate high temperature and velocity flows. Nevertheless, it is also suitable to simulate chemical reacting flows like the present case of combustion. The SPARK software does not have a turbulence model.

4.2.2 Simulation Set-up

In the following simulations, the flow is 2D axisymmetric. The chemically reacting gas is employed with the kinetic scheme from Burke [83], given in Appendix C, that has been validated for high-pressure combustion applications. The time scheme is implicit.

The considered domain is a square with a 4 mm side length. Since the simulation is modelled as 2D axisymmetric, the domain represented in figure 4.1 (a) only has one-quarter of the total domain.

Besides the domain limits, the boundary conditions used are represented, being those two symmetry axes, at y=0 mm and x=0 mm, and on the outer region, two subsonic outlets where the static pressure is assigned according to the initial pressure.

To ignite the mixture, a Gaussian heat source is employed during the initialization of the field. In figure 4.1, the initial temperature field is presented, with a plot of the 1D temperature profile across y=0. The pressure profile on the Gaussian is constant, and the density profile obeys the perfect gas equation considering the constant field pressure, and temperature distribution.

The centre region temperature of the Gaussian was chosen to be slightly below the adiabatic flame temperature of the mixture.

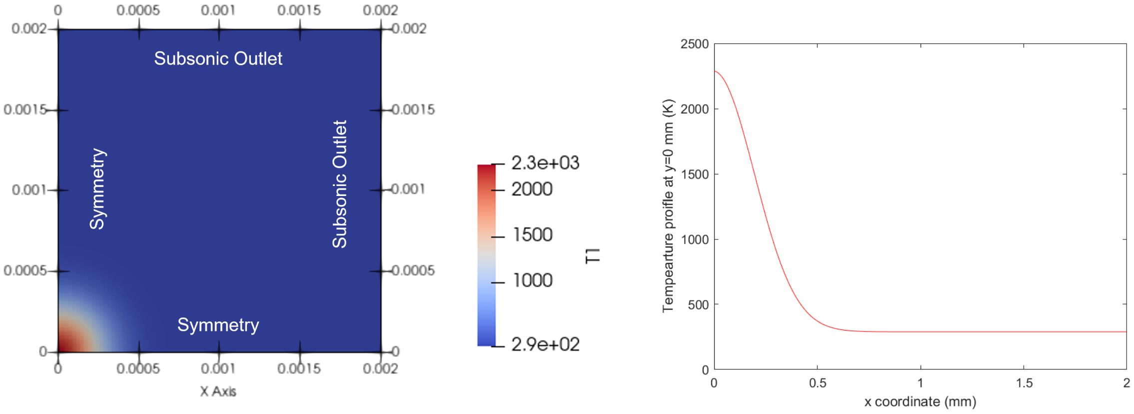

(a) (b)

Figure 4.1: Boundary conditions (a) and Gaussian temperature field initialization (b).

4.2.2.1 Simulations Initial Conditions

The main goal was to study the influence that the filling parameters have on the burning velocity (S), and hence, the dilution ratio (D) and the equivalence ratio (λ) were varied. Besides these parameters, the Lewis number was also varied to understand how the ratio of thermal to mass diffusivity influence S and the flame instabilities.

The initial conditions used for the simulations are summarized in table 4.1.

Table 4.1: Initial filling conditions for each simulation.

	Le	$p_{fill}(bar)$	T (K)	He/ H_2/O_2	λ	% He
Simulation 1	1	5	290	8 / 2 / 0.8	0.8	74%
Simulation 2	1	5	290	8 / 2 / 1.0	1	73%
Simulation 3	1	5	290	8 / 2 / 1.2	1.2	71%
Simulation 4	1	5	290	4 / 2 / 0.8	0.8	59%
Simulation 5	1	5	290	4 / 2 / 1.0	1	57%
Simulation 6	1	5	290	4 / 2 / 1.2	1.2	55%
Simulation 7	1.4	5	290	4 / 2 / 1.0	1.0	57%
Simulation 8	0.8	5	290	4 / 2 / 1.0	1.0	57%

4.2.3 Mesh independence study

To correctly understand the dynamics of the proposed simulations, a suitable mesh must be chosen. One of the main factors that will influence the minimum mesh size for premixed flames is the flame thickness, given in equation 3.6b, and also the chemistry of the preheating zone, where chemical non-equilibrium is present.

The criteria used to choose the mesh was based on the final velocity obtained. Three meshes were tested, with the cell size equal to $20\mu m$, $10\mu m$, $5\mu m$. For this mesh independence study, a 1D approach was used to reduce the computational costs. For this, the simulations were launched as 2D, but with a mesh that only had cells along one axis.

In figure 4.2 the obtained results for the normalized flame propagation velocity are given. The normalization was done with the final velocity value of the finest mesh.

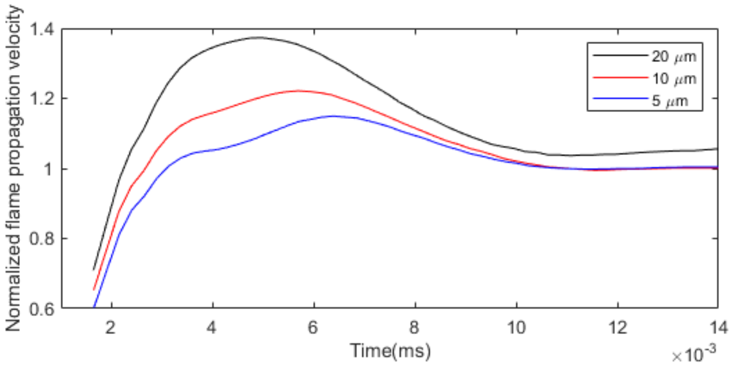

Figure 4.2: Normalized flame propagation velocity for different meshes.

Although the profiles do not match exactly, the value of interest is the final flame velocity. Considering the obtained results, the mesh with $10\mu m$ was chosen for the 2D simulations. This cell size is used for both directions since the modelled phenomenon does not have a preferential direction of propagation.

4.2.4 Numerical Issues

Previously to this study, the first goal with the simulations using the SPARK code was to reproduce the combustion inside ESTHER's combustion driver. The deployed models were the same, but the domain partially considered the dimension of the driver.

The gas was ignited inside the ignition channel, and once the ignition started, a transition to a detonation occurred right after, where it was possible to observe the formation of a shock wave that would ignite the gas immediately behind it. Because of the physical nature of the flow, the mesh size that was found to be suitable $(200\mu m)$ was coarser since it was not limited by the flame thickness in typical deflagrations.

To overcome this unwanted detonation, since it did not represent the physics of the experiments, the ignition source energy was reduced until a deflagration occurred. But with this approach, it was not computationally feasible to simulate the combustion phenomena inside the entire driver without a flame thickening model that would help to increase the flame thickness, and hence, the required mesh size. Besides the computational limitation, the flow inside ESTHER's combustion chamber is mostly turbulent, and to recreate it would be necessary to have a turbulence model like LES (Large Eddy Simulation), or RANS (Reynolds-averaged Navier–Stokes equations), or launch the simulation as a DNS, but the same problem with extremely high computational arises.

Owing to this, the initial CFD case study had to be set aside, nevertheless, some snapshots of the obtained results with the detonation wave are presented in Appendix D.

4.2.5 Results and discussion

4.2.5.1 Flame shape

In figure 4.3, four time instants of the freely propagating spherical flame of simulation 4 are shown. This flame is propagating in a laminar regime, and from the H_2O mass fraction field, it is visible that the equilibrium chemical composition is not reached instantly.

The flame propagates freely without any disturbances until the fourth time instant. However this behaviour of a perfect spherical flame does not last during the entire simulation time and domain, as it will be shown next.

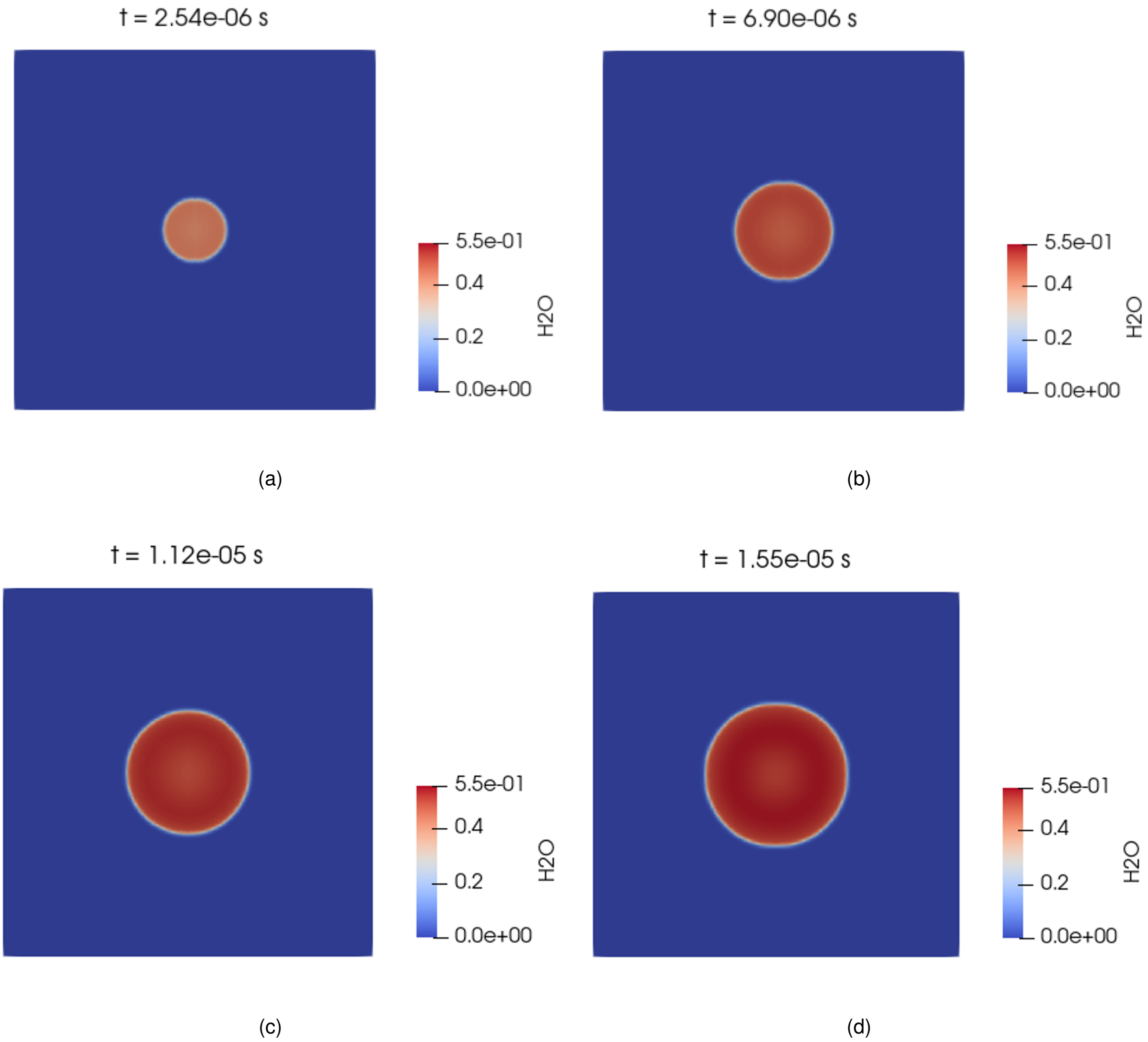

(a) (b)

(c) (d)

Figure 4.3: H_2O mass fraction evolution of simulation 4 ($He/H_2/O_2$ ratio of 4:2:0.8).

4.2.5.2 Flame Radius

The simulations 1 to 3 and 4 to 6 have a constant dilution ratio, $D = 8$ and $D = 4$, respectively, with λ varying from 0.8 to 1.2.

In figures 4.4, the evolution of the flame radius along the simulation time is given for the three different λ mixtures, for $D = 8$ (a) and for $D = 4$ (b).

To obtain the flame radius, the considered reference was the temperature iso-line at 1000K for every simulation. From this value, the flame surface area was obtained.

For both sets of simulations, with different dilutions, the flame radius has a steeper value increase in the first period of time, due to the Gaussian heat source, but the slope tends to a constant value. This slope will be the considered flame propagation velocity, which will be shown next.

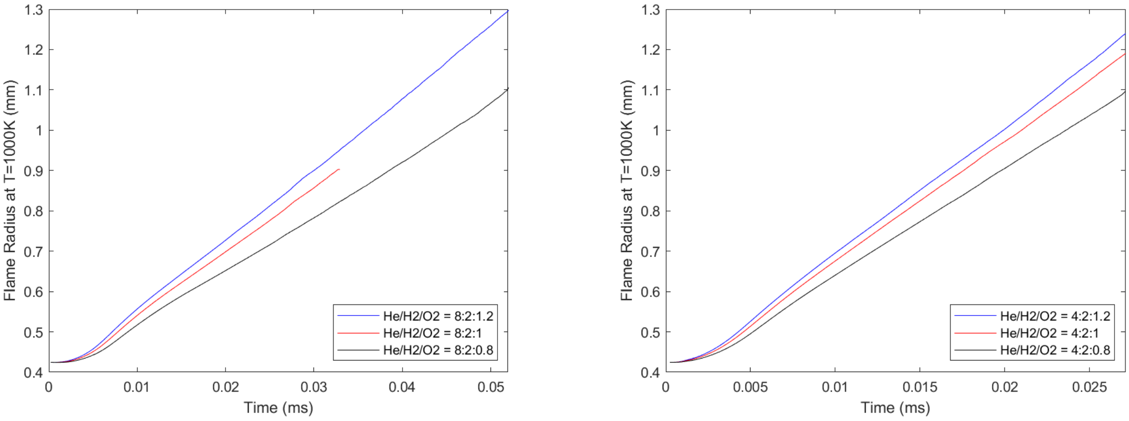

(a) (b)

Figure 4.4: Flame radius evolution for $D = 8$ (a) and for $D = 4$ (b).

4.2.5.3 Laminar flame speed

To obtain the laminar flame speed, the flow ahead the flame may not be disturbed, and hence, only the values before these instabilities start occurring will be considered for the analysis.

In figure 4.5, the flame propagation speeds for simulations 1 to 6 are given. The flame propagation velocity has to be distinguished from the laminar flame speed since once the flame front is disturbed, the flame propagation velocity is not simply the laminar flame speed but a sum of this velocity and the local flow velocity, as shown in equation 3.5.

The behaviour of the velocity plot is the same for all simulations, firstly the velocity increases constantly until it reaches the maximum value, and afterwards, it decreases and ends converging to a value for most of the simulations. The initial behaviour is still under the influence of the Gaussian used to ignite the gas. It is considered that the Gaussian does not influence the results from a radius $> 0.5mm$, as seen in 4.1.

The obtained laminar flame speed values, taken from the stable region of the plot, are the following:

- Simulation 1 ($\mathrm{He/H_2/O_2}$ = 8:2:0.8): $S_L \approx 12.6m/s$
- Simulation 2 ($\mathrm{He/H_2/O_2}$ = 8:2:1): $S_L \approx 15.3m/s$
- Simulation 3 ($\mathrm{He/H_2/O_2}$ = 8:2:1.2): $S_L \approx 16.5m/s$

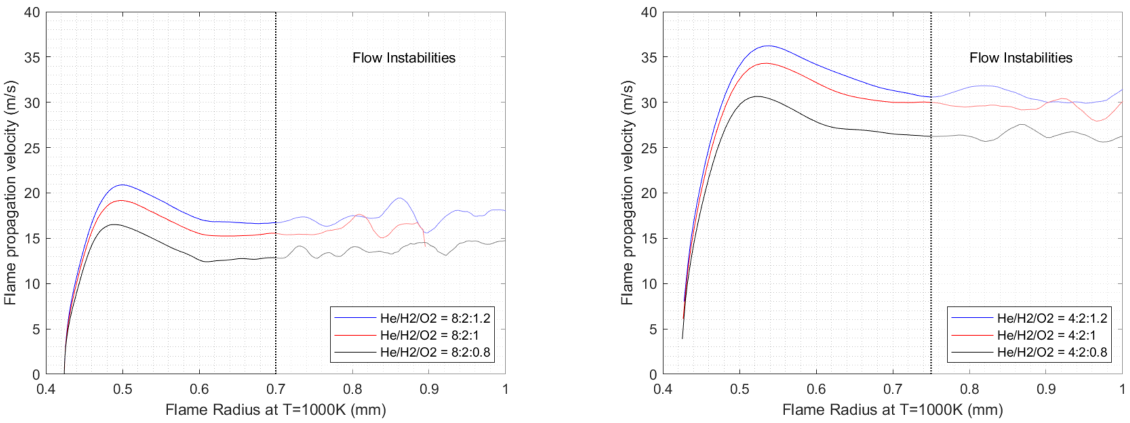

(a) (b)

Figure 4.5: Flame speed versus flame radius for simulations 1 to 3 (a) and 4 to 6 (b).

- Simulation 4 ($\mathrm{He/H_2/O_2}$ = 4:2:0.8): $S_L \approx 27m/s$
- Simulation 5 ($\mathrm{He/H_2/O_2}$ = 4:2:1): $S_L \approx 30m/s$
- Simulation 6 ($\mathrm{He/H_2/O_2}$ = 4:2:1.2): $S_L \approx 31m/s$

The obtained values are much higher than the experimental unstretched laminar flame speeds obtained in the experiments from figure 3.5, where the obtained results differ with two orders of magnitude.

During the simulations, as the flame front started to propagate outside the Gaussian heat source, a ”temperature shock” developed in front of the flame, increasing the temperature to around 500 K. This phenomenon was observed for every simulation, using different solvers, and in Euler as well. Because of this, instead of burning a mixture around 290K, the flame was consuming a gas with a higher temperature, and with increasing temperature, the flame speed will increase. This can be seen in the work of X. Lu in [84]. It is assumed that this numerical phenomenon was the main contributor to the discrepancies.

Comparing the results from simulations 2 and 5, for example, the influence that the dilution ratio has on the obtained flame speed is very clear. The S_L value for the lower dilution is almost twice the one from the higher dilution. It is expected that as the dilution decreases, the flame burning speed decreases, and hence, these results are qualitatively correct.

According to what was physically expected, the flame speed should increase with decreasing λ, but what is observed is the exact opposite behaviour for both sets of simulations. This can be due to the fact that the used transport model assumes that all species have the same diffusion coefficient, and hence, hydrogen diffusion will not play a distinct role in these numerical simulations like what is observed in reality. Besides the diffusion coefficients, the Lewis number is also assumed to be the same for all species, something that can lead to errors especially with light molecules like $\mathrm{H_2}$ [52].

But even when considering the transport model, it was expected that the mixture with $\lambda = 1$ would reach the highest flame speed and not the mixture with $\lambda = 1.2$. This can be explained by the fact that although the dilution ratio and hence, the ratio of He moles per 2 of $\mathrm{H_2}$, is constant, the molar fraction of He is higher for the mixture with $\lambda = 1$, and hence, this can decrease the flame velocity.

On the right side of the plots, the velocity starts to oscillate considerably. This is due to the fact that in that region, the flow ahead of the flame starts to get turbulent. This can be seen by estimating the turbulent Reynolds number from equation 3.13, that for $Re_t > 1$ the flow is considered to be turbulent. Assuming a characteristic length scale equal to the flame thickness, the Re_t is given by the ratio between the fluctuation velocity (u') and the unstretched laminar flame speed (S_L^0). Hence, for $u' < S_L^0$, the flame front is considered laminar. In figure 4.6, the plot of the mean fluctuation velocity ahead of the flame front versus the flame radius from simulation 4 , from figure 4.3, is given. As a reference line, the obtained approximate laminar flame speed (S_L) is plotted. This velocity differs from the unstretched laminar flame speed (S_L^0), but the values will be similar and S_L is used as the reference value.

The velocity fluctuations start to get very close to S_L from the flame radius value of 0.8 mm. From this point, u' continues to grow and it is assumed that from this point, the flame front starts to get turbulent. This goes according to the velocity behaviour in figure 4.5, whereas for the black plot, the values start to get oscillations from approximately 0.8 mm.

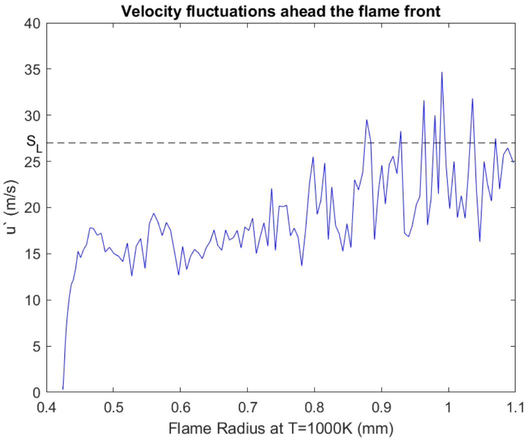

Figure 4.6: Velocity fluctuation vs flame radius.

From this point, the flame starts to get disturbed and the results are not a real representation of a turbulent flame, since turbulence will mainly be a 3D phenomenon. Nevertheless, 2D DNS turbulent flames simulations may also provide a good insight into this phenomena, since for premixed combustion Cant et al. [85] showed that it is more likely to find locally cylindrical (2D) flame sheets, than finding 3D spheroidal flame surfaces.

To simulate a turbulent flame using the SPARK code, since there is no 3D simulation type, a 2D approach would have to be used via DNS. However, the boundary conditions could not include symmetry axis like the ones used in this work since the distribution of eddies is stochastic.

4.2.5.4 Lewis number influence

Another set of simulations was done, but varying the lewis number. In the previous simulations, a unitary Lewis number was employed. For simulations 7 and 8, the same initial conditions from simulation 5 were used, but with different Lewis numbers, equal to 1.4 and 0.8, respectively.

Considering the models used, with a non-unitary Lewis number, the thermal diffusivity will differ from the mass diffusivity, but will still be the same for every species. With $Le < 1$, the mass diffusivity will be greater than the thermal diffusivity, and of $Le > 1$, the opposite.

In figure 4.7, the results of stimulations 5, 7, and 8 are given, with the flame radius versus time (a), and the flame propagation velocity versus the flame radius (b).

For the highest lewis number, the flame burning speed increased, when compared with the unitary Lewis number. For the lowest Lewis number it decreased instead.

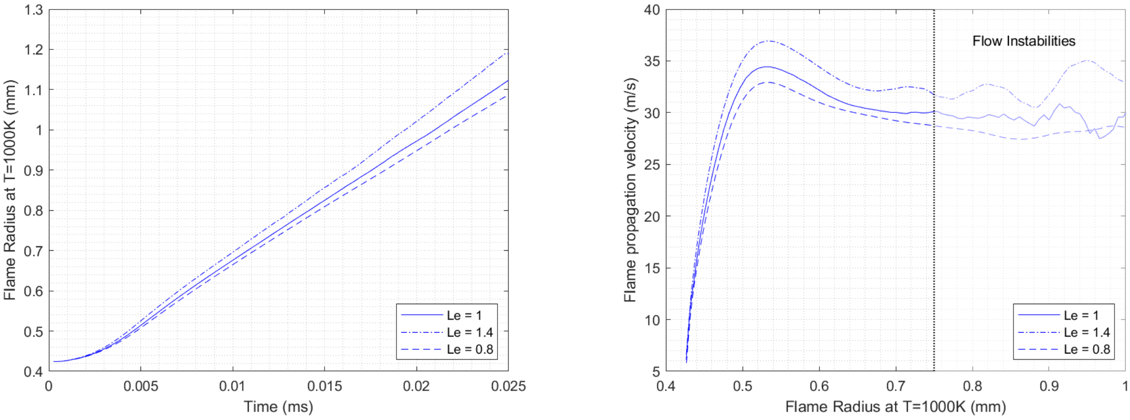

(a) (b)

Figure 4.7: Flame radius evolution (a) and flame speed versus flame radius (b) for simulations 5,7,and 8.

Chapter 5

Conclusions

This final chapter gives a summarized review of the obtained results and achievements, followed by recommendations for future work.

5.1 Achievements

The major goal of this thesis was to study the high-performance combustion driver of the ESTHER shock tube. This was mainly done in two parts, firstly by studying ESTHER's performance and the influence that the driver has, followed by the qualification campaign of the combustion driver, where its performance was studied and proven.

Firstly, the influence that the driver gas composition has on the performance was shown. Two sets of compositions were tested, one with Helium as the bath gas, and the other with Nitrogen. Considering the same combustion temperature, it was shown that for the mixtures with Helium as the bath gas, an increased ratio of Oxygen would decrease the performance slightly, and the opposite would happen if the dilution ratio increased. For the mixtures with $\mathrm{N_2}$ as the bath gas, the same would happen for an increased Oxygen ratio, and the performance would decrease for an increasing dilution ratio with $\mathrm{N_2}$. The main performance difference was between the two mixtures with $\mathrm{N_2}$ or He as the diluent, where the main shock speed with He was close to double of the performance obtained with $\mathrm{N_2}$.

One of the driver conditions that has the greatest impact on the performance is the post-combustion pressure (100 bar to 600 bar). Highest post-combustion pressures lead to higher shock speeds. Besides the pressure variation, the combustion temperature was also studied, a parameter which depends mostly on the initial mixture and also combustion efficiency. Considering a temperature range from half to the full adiabatic temperature, it was shown that this parameter also has a significant influence on the performance. For the mixture with Nitrogen as the diluent gas, the flame temperature is significantly lower, and hence, the performances are also lower.

Besides the driver initial parameters, the influence that the compression gas and test gas conditions have was also shown. For the compression tube, the lowest performance is limited by its length, and the corresponding parameters were obtained for the test atmospheres of interest. This lower performance limit is then given in the performance envelopes. For the test gas, as the pressure decreases, and the pressure ratio between the driver pressure and the test pressure increases, performance increases accordingly.

Using Mirels theory, the test times for Earth and Mars atmospheres were obtained. The influence that the driver gas conditions have on the test time was also studied, and for most of the conditions, the test time increases with lower performances.

Besides the double stage configuration, a single stage configuration performance was also simulated, showing that for lower performances this configuration has a limited operational range.

On the experimental campaign of ESTHER's combustion driver, there were two main goals, proving the performance and operability of the driver, and study high-pressure combustion inside closed vessels. Firstly, the parametric study was presented.

The influence that the filling pressure, Helium dilution, equivalence ratio, and ignition type was analysed. The Helium dilution was one of the most influencing filling parameters, wherewith decreasing values, the onset of detonations, and transitions to detonations were more likely. With lower dilution, the compression ratio, the amplitude of the accoustic waves, and the average flame propagation speed increased.

With increasing pressure, the onset of detonation that comes with more energetic accoustic waves is more likely. These accoustic waves were damped with an increasing equivalence ratio, and hence, richer Oxygen mixtures.

Although the equivalence ratio influences the accoustic wave amplitude for higher pressures ($> 50bar$), for lower pressures this isn't the case. Nevertheless, it was shown that the compression ratio increased as the mixture conditions got closer to the stoichiometric conditions.

Changing the laser ignition from focused to unfocused and maintaining the initial conditions, showed that the accoustic wave amplitude depends on the flame dynamics inside the chamber since the amplitude obtained with unfocused ignition was 6 times greater than the ones from the focused ignition shot.

Besides this parametric study, further operability and performance of the driver were given, where the pressure range was proven, and repeatability was also achieved. Considering the parametric study, the initial filling conditions depend on the desired final pressure, since strong accoustic waves and detonations aren't desirable.

In the third part of this thesis, a CFD numerical study with high-pressure premixed combustion of $\mathrm{He/H_2/O_2}$ was given. Firstly, one has to bear in mind that this was the first time the SPARK code was used for 2D combustion studies. Secondly, the purpose of this part of the work was subjected to several changes since it was found that SPARK wasn't suitable to simulate the initial case study. Therefore it was decided to decrease the level of complexity and to try to model laminar premixed freely expanding flames so that in future studies more complex problems like turbulent flames may be studied.

During this process, many numerical issues were encountered and the strategy had to change more than once. Nevertheless, some improvements were done, like the ignition source being changed from a density constant Gaussian to a pressure constant one for unconfined flames.

The laminar flame speeds obtained are much higher than similar experimental conditions, and qualitatively speaking, the results differences when changing the dilution were found to be physical, but not when the equivalence ratio was varied. In similar works, fine-tuning of the numerical models has to be done before the results get close to experimental ones.

Although some of the results show that the gas model may be il-suited, some shortfalls were identified and these results still pave the way for future 2D combustion studies using the SPARK code.

5.2 Future Work

For future work regarding the studied subjects, the following is recommended.

For ESTHER's performance estimations and range studies:

- Include real gas modelling in the compression tube to understand the influence of using $\mathrm{N_2}$ as the intermediate gas;
- Include performances with pressurized (50 bar to 100 bar) He or $\mathrm{N_2}$ in the driver, although this would require a different diaphragm configuration;
- Once ESTHER is commissioned, update Milne correlations values with experimental data;
- Update the performance maps considering the experimental results of the driver qualification campaign, with the range of the final temperatures and pressures.

Regarding the driver experimental campaign and high-pressure combustion studies, the following is recommended:

- Use different laser ignition configurations. Ignition could be achieved in the middle of the chamber by changing the focal point;
- Use $\mathrm{N_2}$ as the bath gas instead of He and study the performance differences and respective combustion outputs;
- Study the effects of geometry and compare the driver shots with the ones from the scaled driver campaign;

For future 2D premixed high-pressure combustion studies using the SPARK code, the following recommendations are given:

- If a Gaussian heat source is used, a detailed analysis of the initialization has to be done. A suggestion is to initialize the gas with the 1D profiles of a fully developed flame, instead of just initializing the temperature and the density/pressure;
- Implement a flame thickening model that will increase the flame thickness. With this, coarser meshes may be used, decreasing the computational cost significantly;
- For turbulent flames studies, currently it is only possible to do this using DNS, which can only be used in very small domains. For other applications, the implementation of LES or RANS models is necessary;
- To decrease computational costs, single-step chemistry may also be implemented;

- If LENS or RANS models are implemented, and premixed flame inside chambers is the subject of study, the results of the scaled combustion driver provide good experimental comparison since the computational cost for simulating this domain is much smaller when compared to the full-scale driver.
- Validate the code with experimental results or with other computational studies.

Bibliography

[1] National Aeronautics and Space Administration. https://mars.nasa.gov/mars2020/, . Accessed on the 24th of February, 2021.

[2] P. A. Gnoffo, C. O. Johnston, and B. Kleb. Challenges to computational aerothermodynamic simulation and validation for planetary entry vehicle analysis. Technical report, NASA Langley Research Center, 2010.

[3] European Space Agency. https://mars.nasa.gov/mars2020/. Accessed on the 25th of February, 2021.

[4] M. A. Barucci, M. Yoshikawa, P. Michel, J. Kawagushi, H. Yano, J. R. Brucato, I. A. Franchi, E. Dotto, M. Fulchignoni, and S. Ulamec. Marco polo: Near earth object sample return mission march. *Experimental Astronomy*, 23, 2009.

[5] P. Reynier. Survey of high-enthalpy shock facilities in the perspective of radiation and chemical kinetics investigations. *Progress in Aerospace Sciences*, 85, 2016. DOI: 10.1016/j.paerosci.2016.04.002.

[6] National Aeronautics and Space Administration. $https://nssdc.gsfc.nasa.gov/planetary/factsheet/index.html$, . Accessed on the 1st of March, 2021.

[7] G. Herdrich, S. Lohle, and M. Fertig. Experimental simulation of high enthalpy planetary entries. *The Open Plasma Physics Journal*, 2009. DOI: 10.2174/1876534300902010150.

[8] D. Luís. Performance design of hypervelocity shock tube facilities. Ms. c thesis, Instituto Superior Técnico, Universidade de Lisboa, September 2018. available at https://fenix.tecnico.ulisboa.pt/cursos/meaer/dissertacao/ 1972678479054139.

[9] P. N. Desai, G. D. Qualls, and M. Schoenenberger. Reconstruction of the genesis entry. *Journal of Spacecraft and Rockets*, 45, 2008. DOI: 10.2514/1.30042.

[10] M. A. Shoemaker, J. C. van der Ha, and K. Fujita. Trajectory reconstruction of hayabusa's atmospheric reentry. *Acta Astronautica*, 71, 2012. DOI: 10.1016/j.actaastro.2011.08.006.

[11] P. N. Desaia, R. A. Mitcheltree, and F. M. Cheatwood. Entry trajectory issues for the stardust sample return capsule. *International Symposium on Atmospheric Reentry Vehicles and Systems*, 1999.

[12] National Aeronautics and Space Administration. $https : //en.wikipedia.org/wiki/mars_atmospheric_entry/media/file : mars - science - laboratory - mars - entry - trajectory.png,$. Accessed on the 1st of March, 2021.

[13] B. Kazeminejada, D. H. Atkinson, M. Pérez-Ayúcard, J. Lebretond, and C. Sollazzo. Huygens' entry and descent through titan's atmosphere—methodology and results of the trajectory reconstruction. *Planetary and Space Science*, 55, 2007. DOI: 10.1016/j.pss.2007.04.013.

[14] B. Harvey. *Russian Planetary Exploratio: History, Development, Legacy, Prospects*, chapter 6: The high summer of Soviet planetary exploration, 1975-1986.

[15] R. Beebe and L. Dudzinski. Saturn atmospheric entry probe trade study. Mission concept study, NASA, 2010.

[16] T. R. Spilker, C. S. Borden, M. Adler, M. M. Mun, R. W. Powell, R. D. Braun, P. M. Beauchamp, J. A. Cutts, P. F. Wercinski, and the A-Team. An assessment of aerocapture and application to future missions. Technical report, NASA, 2016.

[17] Oxford Thermofluids Institute. http://oti.eng.ox.ac.uk/facilities/t6-stalker-tunnel/. accessed December 13, 2020.

[18] S. P. Sharma and C. Park. Operating characteristics of a 60-and 10-cm electric arc-driven shock tube-part ii: The driven section. *Journal of Thermophysics and Heat Transfer*, 4, 1990. DOI: 10.2514/3.56243.

[19] K. C. Hendershot. Development of a combustion driven shock tunnel. *In Symposium on Hypersonic Tecniques*, 1960.

[20] M. L. da Silva, R. Ferreira, J. Vargas, R. Rodrigues, B. Carvalho, L. L. Alves, B. Goncalves, A. Smith, J. Merrifield, S. McDowelld, D. Evans, P. Reynier, V. F. Villace, and L. Marraffa. European shock-tube for high enthalpy research: Design and instrumentation, manufacturing, and acceptance testing. *AIAA Scitech 2020 Forum*, Jan. 2020. DOI: 10.2514/6.2020-0624.

[21] R. A. Alpher and D. R. White. Flow in shock tubes with area change at the diaphragm section. *Journal of Fluid Mechanics*, 3, 1958. DOI: 10.1017/S0022112058000124.

[22] H. Mirels. Test time in low-pressure shock tubes. *Physics of Fluids*, 6, 1963. DOI: 10.1063/1.1706887.

[23] A. Roshko. On flow duration in low-pressure shock tubes. *The Physics of Fluids*, 3, 1960. DOI: 10.1063/1.1706147.

[24] W. J. Hooker. Testing time and contact-zone phenomena in shock-tube flows. *The Physics of Fluids*, 4, 1961. DOI: 10.1063/1.1706147.

[25] R. J. Stalker. An investigation of free piston compression of shock tube driver gas. Report MT 44, National Research Council Canada, Division of Mechanical Engineering, Gas Dynamics Section, 1961.

[26] R. J. Stalker. A study of the free-piston shock tunnel. *AIAA*, 5(12), 1967.

[27] M. J. Lewis. A description of the v. k. i. piston driven shock tube. Report TM 20, The von Karman Institute for Fluid Dynamics, 1970.

[28] P. Jacobs, R. Morgan, A. Brandis, D. Buttsworth, A. Dann, M. D'Souza, T. E. D. Gildfind, R. Gollan, C. Jacobs, M. McGilvray, T. McIntyre, N. Mudford, H. Porat, D. Potter, and F. Zande. Design, operation and testing in expansion tube facilities for super-orbital re-entry. Technical report, The University of Queensland, 2013.

[29] D. Potter, R. Gollan, T. Eichmann, T. McIntyre, R. Morgan, and P. Jacobs. Simulation of CO2-N2 Expansion Tunnel Flows for the Study of Radiating Shock Layers. *46th AIAA Aerospace Sciences Meeting and Exhibit*, Jan. 2008. DOI: 10.2514/6.2008-1280.

[30] A. G. Dann, R. G. Morgan, D. E. Gildfind, P. A. Jacobs, M. McGilvray, and F. Zander. Upgrade of the x3 super-orbital expansion tube. *Proceedings of the 18th Australasian Fluid Mechanics Conference*, 2012.

[31] A. Andrianatos, D. Gildfind, and R. Morgan. Driver condition development for high-enthalpy operation of the x3 expansion tube. *31st International Symposium on Shock Waves 2*, 2019. DOI: 10.1007/978-3-319-91017-8_37.

[32] R. Morgan, T. McIntyre, D. R. Buttsworth, P. A. Jacobs, D. Potter, A. M. Brandis, R. J. Gollan, B. C. C. Jacobs, M. McGilvray, and T. Eichmann. Impulse facilities for the simulation of hypersonic radiating flows. *38th AIAA Fluid Dynamics Conference and Exhibit*, June 2008. DOI: 10.2514/6.2008-4270.

[33] T. Abe, A. Matsuda, and K. F. S. Sato. Experimental study of nonequilibrium phenomena behind strong shock waves generated in super-orbital reentry flight. Report, Institute of Space and Astronautical Science, 2003.

[34] A. Matsuda, K. Fujita, S. Sato, and T. Abe. Nonequilibrium phenomena behind strong shock waves generated in super orbital re-entry flight. *Journal of Thermophysics and Heat Transfer 18*, 2004. DOI: 10.2514/1.6244.

[35] A. Matsuda, K. Fujita, S. Sato, and T. Abe. Absorption spectroscopy for temperature measurement behind shock wave at super-orbital velocity. *Journal of Thermophysics and Heat Transfer 19*, 2005. DOI: 10.2514/1.12452.

[36] G. Yamada, T. Suzuki, H. Tajayanagi, H. Tajayanagi, and K. Fujita. Development of shock tube for ground testing reentry aerothermodynamics. *Transactions of the Japan Society for Aeronautical and Space Sciences*, May 2011. DOI: 10.2322/tjsass.54.51.

[37] M. Mcgilvray, L. J. Doherty, R. G. Morgan, D. Gildfind, and P. J. P. Ireland. T6: The oxford university stalker tunnel. *Transactions of the Japan Society for Aeronautical and Space Sciences*, 2015. DOI: 10.2514/6.2015-3545.

[38] S. P. Sharma and C. Park. Operating characteristics of a 60-and 10-cm electric arc-driven shock tube-part i: The driver. *Journal of Thermophysics and Heat Transfer*, 4, 1990. DOI: 10.2514/3.175.

[39] A. Dufrene, M. MacLean, R. Parker, and M. Holden. Experimental characterization of the lens expansion tunnel facility including blunt body surface heating. *49th AIAA Aerospace Sciences Meeting including the New Horizons Forum and Aerospace Exposition*, 2011. DOI: 10.2514/6.2011-626.

[40] A. Paull and R. J. Stalker. Test flow disturbances in an expansion tube. *Journal of Fluid Mechanics*, 245, 1992.

[41] J. H. Spurk. Design, operation and preliminary results of the brl expansion tube. *Fourth Hypervelocity Techniques Symposium*, 1965.

[42] G. D. Norfleet, J. J. Lacey, and J. D. Whitfield. Results of an experimental investigation of the performance of an expansion tube. *Fourth Hypervelocity Techniques Symposium*, 1965.

[43] A. Dufrene, M. MacLean, R. Parker, T. Wadhams, and M. Holden. Characterization of the new lens expansion tunnel facility. *48th AIAA Aerospace Sciences Meeting Including the New Horizons Forum and Aerospace Exposition*, 2010. DOI: 10.2514/6.2010-1564.

[44] J.H.Grinstead, M.C.Wilder, D.C.Reda, C.J.Cornelison, B. A. Cruden, C. J. Cornelison, and B. A. Cruden. Shock tube and ballistic range facilities at nasa ames research center. Technical report, NASA, 2010.

[45] D. W. Bogdanoff. Shock tube experiments for earth and mars entry conditions. Report, NASA, 2009.

[46] M. L. da Silv and B. B. de Carvalho. High-Pressure H2/He/O2 Combustion Experiments for the Design of the ESTHER Shock-Tube Driver. *46th AIAA Thermophysics Conference*, June 2016. DOI: 10.2514/6.2016-4156.

[47] A. J. Smith. Esther performance estimation. Technical report, Fluid Gravity Engineering Ltd, October 2011.

[48] Z. A. Walenta. Optimization of the parameters of a double-diaphragm shock tube. *Archiwm Mechaniki Stosowanej*, 5(19), 1967.

[49] S. Billett. *STAGG User Manual*. Fluid Gravity Engineering Ltd, December 2018.

[50] R. J. Stalker and B. P. Edwards. Hypersonic blunt-body flowns in hydrogen-neon mixtures. *Journal of Spacecraft and Rockets*, 35, 1998. DOI: 10.2514/2.3399.

[51] S. R. Turns. *An Introduction to Combustion: Concepts and Applications*, chapter Chapter 8: Laminar Premixed Flames. 3rd edition edition, 2012.

[52] T. Poinsot and D. Veynante. *Theoretical and numerical combustion*. RT Edwards, Inc., 2005.

[53] F. N. Egolfopoulos and C. K. Law. Chain mechanisms in the overall reaction orders in laminar flame propagation. *Combustion and Flame*, 80, 1990. DOI: 10.1016/0010-2180(90)90049-W.

[54] M. P. Burke, M. C. F. L. Dryer, and Y. Ju. Negative pressure dependence of mass burning rates of h/co/o/diluent flames at low flame temperatures. *Combustion and Flame*, 157, 2010. DOI: 10.1016/J.COMBUSTFLAME.2009.08.009.

[55] S. D. Tse, D. L. Zhu, and C. K. Law. Morphology and burning rates of expanding spherical flames in H2/O2/inert mixtures up to 60 atmospheres. *Proceedings of the Combustion Institute*, 28, 2000. DOI: 10.1016/S0082-0784(00)80581-0.

[56] G. Ciccarelli and S. Dorofeev. Flame acceleration and transition to detonation in ducts. *Progress in Energy and Combustion Science*, 34, 2008. DOI: 10.1016/j.pecs.2007.11.002.

[57] J. K. Bechtold and M. Matalon. Hydrodynamic and diffusion effects on the stability of spherically expanding flames. *Combustion and Flame*, 67, 1987. DOI: 10.1016/0010-2180(92)90085-4.

[58] S. Kwon, L. K. Tseng, and G. M. Faeth. Laminar burning velocities and transition to unstable flames in H2/O2/N2 and C3H8/O2/N2 mixtures. *Combustion and Flame*, 90, 1992. DOI:.

[59] L. H. C. K. L. C. J. Sun, C. J. Sung. Dynamics of weakly stretched flames: quantitative description and extraction of global flame parameters. *Combustion and Flame*, 188, 1999. DOI: 10.1016/S0010-2180(98)00137-0.

[60] S. M. Kogarko. Amplification of compression waves in the combustion zone. *Symposium (International) on Combustion*, 8, 1961. DOI: 10.1016/S0082-0784(06)80614-4.

[61] J. Leyer and N. Manson. Development of vibratory flame propagation in short closed tubes and vessels. *Symposium (International) on Combustion*, 13, 1971. DOI: 10.1016/S0082-0784(71)80056-5.

[62] F. Tamanini and j. L. Chaffee. Turbulent vented gas explosions with and without acoustically-induced instabilities. *Symposium (International) on Combustion*, 24, 1992. DOI: 10.1016/S0082-0784(06)80216-X.

[63] C. J. M. V. Wingerden and J. P. Zeeuwen. On the role of acoustically driven flame instabilities in vented gas explosions and their elimination. *Combustion and Flame*, 51, 1983. DOI: 10.1016/S0010-2180(98)00137-0.

[64] A.J.Laderman, P.A.Urtiew, and A.K.Oppenheim. Effect of ignition geometry on initial flame acceleration in a spark ignited explosive gas. *Combustion and Flame*, 6, 1962. DOI: 10.1016/0010-2180(62)90110-4.

[65] A. Teodorczyk and J. H. S. Lee. Detonation attenuation by foams and wire meshes lining the walls. *Shock Waves*, 4, 1995. DOI: 10.1007/BF01414988.

[66] R. Borghi. On the structure and morphology of turbulent premixed flames. In *Recent advances in the Aerospace Sciences*. Springer, 1985.

[67] J. E. Shepherd and J. H. S. Lee. On the transition from deflagration to detonation. In *Major research topics in combustion*, pages 439–487. Springer, 1992.

[68] P. Laffitte and P. Dumanois. Influence of pressure on the formation of the explosive wave. *Comptes Rendus de l'Académie des Sciences Paris*, 183, 1926.

[69] P. Laffitte. Influence of temperature on the formation of explosive waves. *Comptes Rendus de l'Académie des Sciences Paris*, 186, 1928.

[70] L. E. Bollinger, M. C. Fong, and R. Edse. Experimental measurements and theoretical analysis of detonation induction distances. *ARS Journal*, 31(5), 1961.

[71] G. A. Campbell and P. V. Rutledge. Detonation of hydrogen peroxide vapour. In *Institution of Chemical Engineers Symposium Series*, volume 33, 1972.

[72] L. E. Bollinger, R. Edse, and J. A. Laughrey. Experimental detonation velocities and induction distances in hydrogen-nitrous oxide mixtures. 1962.

[73] M. Gonzalez, R. Borghi, and A. Saouab. Interaction of a flame front with its self-generated flow in an enclosure: The "tulip flame" phenomenon. *Combustion and Flame*, 88(2), 1992. DOI: 10.1016/0010-2180(92)90052-Q.

[74] C. Tang, Z. Huang, C. Jin, J. He, J. Wang, X. Wang, and H. Miao. Explosion characteristics of hydrogen–nitrogen–air mixtures at elevated pressures and temperatures. *International Journal of Hydrogen Energy*, 34, 2009.

[75] B. Lewis and G. von Elbe. *Combustion, flames and explosions of gases.* 3rd editiom edition, 1987. Pg. 388.

[76] H. Xiao, Q. Duan, and J. Sun. Premixed flame propagation in hydrogen explosions. *Renewable and Sustainable Energy Reviews*, 81, 2018.

[77] C. S. Draper. The physical effects of detonation in a closed cylindrical chamber. Technical report, NASA, 1935.

[78] R. Ferreira. Laser Ignition of a High-pressure H2/He/O2 combustible mixture. Ms. c thesis, Instituto Superior Técnico, Universidade de Lisboa, November 2017. available at https://fenix.tecnico.ulisboa.pt/cursos/meft/dissertacao/565303595501456.

[79] C. R. Wilke. A viscosity equation for gas mixtures. *The Journal of Chemical Physics*, 18, 1950.

[80] F. G. Blottner, M. Johnson, and M. Ellis. Chemically reacting viscous flow program for multicomponent gas mixtures. Technical report sc-rr-70-754, 1971.

[81] G. Palmer and M. Wright. A comparison of methods to compute high-temperature gas thermal conductivity. 2003. DOI: 10.2514/6.2003-3913.

[82] B. Lopez and M. L. da Silva. Spark: A software package for aerodynamics, radiation and kinetics. 2016. DOI: 10.2514/6.2016-4025.

[83] M. Burke, M. Chaos, Y. Ju, F. Dryer, and S. Klippenstein. Comprehensive H2/O2 kinetic model for high-pressure combustion. *International Journal of Chemical Kinetics*, 44, 2012. DOI:10.1002/kin.20603.

[84] X. Lu, E. Hu, X. Li, J. Ku, and Z. Huang. Non-monotonic behaviors of laminar burning velocities of H2/O2/He mixtures at elevated pressures and temperatures. *International Journal of Hydrogen Energy*, 42(34), 2017.

[85] R. S. Cant, C. J. Rutland, and A. Trouvé. Statistics for laminar flamelet modeling. In *Proceedings of the summer program*, page 271. Center for Turbulence Research Stanford, 1990.

[86] Z. Hong, D. F. Davidson, E. A. Barbour, and R. K. Hanson. A new shock tube study of the H+ O2→ OH+ O reaction rate using tunable diode laser absorption of H2O near 2.5 μm. *Proceedings of the Combustion Institute*, 33(1), 2011.

[87] D. Baulch, C. Bowman, C. Cobos, R. Cox, T. Just, J. Kerr, M. Pilling, D. Stocker, J. Troe, W. Tsang, R. Walker, and J. Warnatz. Evaluated kinetic data for combustion modeling: Supplement ii. *Journal of Physical and Chemical Reference Data*, 34, 2005. DOI: 10.1063/1.1748524.

[88] J. V. Michael and J. W. Sutherland. Rate constant for the reaction of h with h/sub 2/o and oh with h/sub 2/by the flash photolysis-shock tube technique over the temperature range 1246-2297 k. *The Journal of Physical Chemistry A*, 92(13), 1988.

[89] W. Tsang and R. F. Hampson. Chemical kinetic data base for combustion chemistry. part i. methane and related compounds. *Journal of physical and chemical reference data*, 15(3), 1986.

[90] N. K. Srinivasan and J. V. Michael. The thermal decomposition of water. *International journal of chemical kinetics*, 38(3), 2006.

[91] J. Troe. Detailed modeling of the temperature and pressure dependence of the reaction H+ O2 (+ M)→ HO2 (+ M). *Proceedings of the combustion institute*, 28(2), 2000.

[92] Initiation in H2/O2: rate constants for H2+ O2→ H+ HO2 at high temperature, author=J. V. Michael and J. W. Sutherland and L. B. Harding and A. F. Wagner, journal=Proceedings of the Combustion Institute, volume=28, number=2, year=2000,.

[93] J. Li, Z. Zhao, A. Kazakov, and F. Dryer. An updated comprehensive kinetic model of hydrogen combustion. *International Journal of Chemical Kinetics*, 36, 2004. DOI:10.1002/kin.20026.

[94] A. Fernandez-Ramos and A. J. C. Varandas. A VTST study of the H+ O3 and O+ HO2 reactions using a six-dimensional DMBE potential energy surface for ground state HO3. *The Journal of Physical Chemistry A*, 106(16), 2002.

[95] L. F. Keyser. Absolute rate constant and branching fractions for the atomic hydrogen+ hydroperoxyl radical reaction from 245 to 300 k. *The Journal of Physical Chemistry*, 90(13), 1986.

[96] H. Hippler, J. Troe, and J. Willner. Shock wave study of the reaction HO2+HO2→H2O2+O2: Confirmation of a rate constant minimum near 700 K. *The Journal of chemical physics*, 93(3), 1990.

[97] J. Troe. The thermal dissociation/recombination reaction of hydrogen peroxide H2O2 (+ M) → 2OH (+ M) III.: Analysis and representation of the temperature and pressure dependence over wide ranges. *Combustion and Flame*, 158(4), 2011.

[98] Z. Hong, R. D. Cook, D. Davidson, and R. Hanson. A shock tube study of OH+ H2O2→ H2O+ HO2 and H2O2+ M→ 2OH+ M using laser absorption of H2O and OH. *The Journal of Physical Chemistry A*, 114(18), 2010.

Appendix A

Shock Tube Theory

A.1 Shock waves equations

In a one dimensional normal shock wave the continuity, momentum, and energy equations are given by equations A.1, A.2, and A.3 respectively. The variable u_s is the gas velociity ahead of the shock, and $u_s - u_2$ is the velocity of the gas behind the shock wave.

$$\rho_1 u_s = \rho_2 \left(u_s - u_2\right) \tag{A.1}$$

$$p_1 + \rho_1 u_s^2 = p_2 + \rho_2 \left(u_s - u_2\right)^2 \tag{A.2}$$

$$h_1 + \frac{1}{2} u_s^2 = h_2 + \frac{1}{2} \left(u_s - u_2\right)^2 \tag{A.3}$$

A.2 Expansion waves equations

The expansion ratio across an unsteady isentropic wave, by applying the Riemann invariant, is given by equation A.4.

$$\frac{p_a}{p_b} = \left(\frac{\rho_a}{\rho_b}\right)^{\gamma} = \left(\frac{a_a}{a_b}\right)^{\frac{2\gamma}{\gamma-1}} = \left[\frac{2+(\gamma-1)M_b}{2+(\gamma-1)M_a}\right]^{\frac{2\gamma}{\gamma-1}}. \tag{A.4}$$

For a steady isentropic process, this ratio is given by equation A.5.

$$\frac{p_a}{p_b} = \left(\frac{\rho_a}{\rho_b}\right)^{\gamma} = \left(\frac{a_a}{a_b}\right)^{\frac{2\gamma}{\gamma-1}} = \left[\frac{2+(\gamma-1)M_b^2}{2+(\gamma-1)M_a^2}\right]^{\frac{\gamma}{\gamma-1}}. \tag{A.5}$$

A.3 Double diaphragm shock tube with cross section area reduction

For a double diaphragm shock tube with cross section area reduction, the pressure ratio p_{11}/p_3 necessary for a given velocity ratio u_3/a_7 is given by equation (2.12), where p_{11}/p_3 is given by (A.6).

$$\frac{p_{11}}{p_8} = \left[k - \frac{\gamma_{11}-1}{\gamma_7+1}\frac{a_7}{a_{11}}\left(M_{s7} - \frac{1}{M_{s7}}\right)\right]^{-\frac{2\gamma_{11}}{\gamma_{11}-1}} \tag{A.6}$$

The parameter k from the previous equation is given by (A.7), and the Mach number in region 10 can be calculated with equation (A.8).

$$k = \left[\frac{2+(\gamma_{11}-1)M_{10}^2}{\gamma_{11}+1}\right]^{\frac{1}{2}} \left[\frac{\gamma_{11}+1}{2+(\gamma_{11}-1)}M_{10}\right] \tag{A.7}$$

$$\frac{1}{M_{10}}\left[\frac{2}{\gamma_{11}+1}\left(1+\frac{\gamma_{11}-1}{2}M_{10}^2\right)\right]^{\frac{\gamma_{11}+1}{2(\gamma_{11}-1)}} = \frac{A_{11}}{A_7} \tag{A.8}$$

The pressure ratio p_8/p_6 is equal to one since it is the pressure ratio across a contact surface, and p_6/p_5 can be given by (A.9), where the variable X is expressed in (A.10) and can be calculated from A.11.

$$\frac{p_6}{p_5} = \frac{\gamma_7+1}{\gamma_7-1}\left(\frac{2\gamma_7}{\gamma_7-1}X^2 - 1\right)^{-1} \tag{A.9}$$

$$X = \frac{U_R + u_6}{a_6} \tag{A.10}$$

$$\left(X^2 + \frac{2}{\gamma_7-1}\right)\left(\frac{2\gamma_7}{\gamma_7-1}X^2 - 1\right) - \left(\frac{2}{\gamma_7-1}\right)^2 \frac{1}{M_5^2}\left(1 + \frac{\gamma_7+1}{2}M_6 X - X^2\right)^2 = 0 \tag{A.11}$$

, where the Mach number in regions 6 and 5 are given by equations (A.12) and (A.13), respectively.

$$M_6 = \frac{M_{s7}^2 - 1}{\left[\left(\gamma_7 M_{s7}^2 - \frac{\gamma_7-1}{2}\right)\left(\frac{\gamma_7-1}{2}\gamma_7 M_{s7}^2 + 1\right)\right]^{1/2}} \tag{A.12}$$

$$\frac{1}{M_5}\left[\frac{2}{\gamma_7+1}\left(1+\frac{\gamma_7-1}{2}M_5^2\right)\right]^{\frac{\gamma_7+1}{2(\gamma_7-1)}} = \frac{A_7}{A_1} \tag{A.13}$$

The pressure ratios p_5/p_4 and p_4/p_3 are expressed in equations (A.14) and (A.15)

$$\frac{p_5}{p_4} = \left[\frac{2}{\gamma_7+1}\left(1+\frac{\gamma_7-1}{2}M_5^2\right)\right]^{-\frac{\gamma_7}{\gamma_7-1}} \tag{A.14}$$

$$\frac{p_4}{p_3} = \left[\frac{\gamma_7+1}{2} - \frac{\gamma_7-1}{2}\frac{u_3/a_7}{a_4/a_7}\right]^{-\frac{2\gamma_7}{\gamma_7-1}} \tag{A.15}$$

, where a_4/a_7 is given by (A.16).

$$\frac{a_4}{a_7} = \frac{a_6}{a_7}\frac{a_5}{a_6}\frac{a_4}{a_5} \tag{A.16}$$

From the previous equation, a_6/a_7 is given by (A.17), where u_6/a_7 is expressed in (A.18).

$$\frac{a_6}{a_7} = \frac{1}{M_6}\frac{u_6}{a_7} \tag{A.17}$$

$$\frac{u_6}{a_7} = \frac{2}{\gamma_7 + 1}\left(\mathrm{M}_{s7} - \frac{1}{\mathrm{M}_{s7}}\right) \tag{A.18}$$

From equation (A.16), the sound of speed ratio a_5/a_6 is given by (A.19) and a_4/a_5 is given by (A.20).

$$\frac{a_5}{a_6} = \left\{\frac{\frac{\gamma_7+1}{2}X}{\left[\left(\gamma_7 X^2 - \frac{\gamma_7-1}{2}\right)\left(\frac{\gamma_7-1}{2}X^2+1\right)\right]^{1/2}}\right\}^{-1} \tag{A.19}$$

$$\frac{a_4}{a_5} = \left[\frac{2}{\gamma_7+1}\left(1 + \frac{\gamma_7 - 1}{2}M_5^2\right)\right]^{1/2} \tag{A.20}$$

As it was mentioned in section 2.1.3, the pressure ratio p_{11}/p_3 depends on M_{s7} and it can be calculated with equation (2.13), where p_6/p_7 is given by equation(A.21).

$$\frac{p_6}{p_7} = \frac{2\gamma_7}{\gamma_7 + 1}\left(M_{s7}^2 - \frac{\gamma_7 - 1}{2\gamma_7}\right) \tag{A.21}$$

But if one wants to optimize the value of M_{s7}, considering (2.14), this equation can be rewritten with (2.12), (A.13), and (A.14), giving equation (A.22).

$$\frac{\partial}{\partial M_{s7}}\left(\ln\frac{p_4}{p_3}\right) = -\frac{d}{dM_{s7}}\left(\ln\frac{p_{11}}{p_8}\right) - \frac{d}{dM_{s7}}\left(\ln\frac{p_6}{p_5}\right) \tag{A.22}$$

From A.6, it follows equation (A.23).

$$\frac{d}{dM_{s7}}\left(\ln\frac{p_{11}}{p_8}\right) = \frac{\frac{2\gamma_{11}}{\gamma_7+1}\frac{a_7}{a_{11}}\left(1+\frac{1}{M_{s7}^2}\right)}{k - \frac{\gamma_{11}-1}{\gamma_7+1}\frac{a_7}{a_{11}}\left(M_{s7} - \frac{1}{M_s}\right)} \tag{A.23}$$

With (A.9), (A.23) can rewritten as (A.24).

$$\frac{d}{dM_{s7}}\left(\ln\frac{p_6}{p_5}\right) = -\frac{4\gamma_7}{\gamma_7+1}\left(\frac{p_6}{p_5}\right)X\frac{dX}{dM_{s7}} \tag{A.24}$$

From (A.11), dX/dM_{s7} is given by (A.25).

$$\frac{dX}{dM_{s7}} = \frac{\left(\frac{2}{\gamma_7-1}\right)^2\frac{(\gamma_7+1)}{2M_5^2}X\left(1+\frac{\gamma_7+1}{2}M_6X - X^2\right)\frac{dM_6}{dM_{s7}}}{X\left[\frac{4\gamma_7}{\gamma_7-1}X^2 + \left(\frac{4\gamma_7}{(\gamma_7-1)^2} - 1\right)\right] + \left(\frac{2}{\gamma_7-1}\right)^2\frac{1}{M_5^2}\left(1+\frac{\gamma_7+1}{2}M_6X - X^2\right)\left(2X - \frac{\gamma_7+1}{2}M_6\right)} \tag{A.25}$$

From (A.12), dM_6/dM_{s7} is given by (A.26)

$$\frac{dM_6}{dM_{s7}} = \frac{2M_6 M_{s7}}{\left(M_{s7}^2 - 1\right)} \left\{ 1 - \frac{M_6^2 \left[\gamma_7 \left(\gamma_7 - 1\right) M_{s7}^2 + \gamma_7 - \left(\frac{\gamma_7 - 1}{2}\right)^2 \right]}{2\left(M_{s7}^2 - 1\right)} \right\} \tag{A.26}$$

By differentiating and rearranging (A.15), u_3/a_7 is (A.27)

$$\frac{u_3}{a_7} = \frac{\gamma_7 + 1}{\gamma_7 - 1} \frac{a_4}{a_7} \frac{\frac{\partial}{\partial M_{s7}} \left(\ln \frac{p_4}{p_3}\right)}{\frac{\partial}{\partial M_{s7}} \left(\ln \frac{p_4}{p_3}\right) - \frac{2\gamma_7}{\gamma_7 - 1} \frac{d}{dM_{s7}} \left(\ln \frac{a_4}{a_1}\right)} \tag{A.27}$$

From (A.13), (A.16), and (A.20), the previous equation is rewritten as (A.28).

$$\frac{d}{dM_{s7}} \left(\ln \frac{a_4}{a_7}\right) = \frac{d}{dM_{s7}} \left(\ln \frac{a_6}{a_7}\right) + \frac{d}{dM_{s7}} \left(\ln \frac{a_5}{a_6}\right) \tag{A.28}$$

From (A.12), (A.17), and (A.18), the previous equation is rewritten as (A.29).

$$\frac{d}{dM_{s7}} \left(\ln \frac{a_6}{a_7}\right) = \frac{\gamma_7 \left(y_7 - 1\right) M_{s7}^2 + \gamma_7 - \left(\frac{\gamma_7 - 1}{2}\right)^2}{\left(\frac{\gamma_7 + 1}{2}\right)^2 M_{s7} \left(\frac{a_6}{a_7}\right)^2} - \frac{1}{M_{s7}} \tag{A.29}$$

Finally, from (A.19) we get (A.20).

$$\frac{d}{dM_{s7}} \left(\ln \frac{a_5}{a_6}\right) = \left[\frac{\gamma_7 \left(\gamma_7 - 1\right) X^2 + \gamma_7 - \left(\frac{\gamma_7 - 1}{2}\right)^2}{\left(\frac{\gamma_7 + 1}{2}\right)^2 X \left(\frac{a_5}{a_6}\right)^2} - \frac{1}{X} \right] \frac{dX}{dM_{s7}} \tag{A.30}$$

As it was mentioned in section 2.1.3, these equations are valid if the flow in region 8 is supersonic or sonic (A.31), the primary shock wave reflects from the second diaphragm as a shock (A.32), and the flow in region 3 is supersonic or sonic (A.33).

$$M_{s7} \geq \frac{\gamma_7 + 1}{\gamma_{11} + 1} \frac{a_{11}}{a_1} \frac{k}{2} + \left[1 + \left(\frac{\gamma_7 + 1}{\gamma_{11} + 1} \frac{a_{11}}{a_2} \frac{k}{2} \right)^2 \right]^{\frac{1}{2}} \tag{A.31}$$

$$M_6 \geq M_5 \tag{A.32}$$

$$\frac{u_3}{a_7} \geq \frac{a_4}{a_7} \tag{A.33}$$

Appendix B

Thermodynamic Relations

B.1 Gas mixture composition

The gas composition mixture can be described by each species number of particles in a specific volume of gas, and for that we have the molar density n_i that is defined by the number of moles per cubic meter, or the number density N_i, that is the number of particles per cubic meter. With each species number density or molar density, it is possible to obtain the global number and or/molar density, given in equation B.1

$$N = \sum_i N_i \qquad n = \sum_s n_i \qquad n_i = \frac{N_i}{N_\mathrm{A}} \tag{B.1}$$

With the density numbers deifned, the each species partial dentisty can be obitained from the particle wieght m_i, or the molar weight M_i, given in equation B.2.

$$\rho_i = N_i m_i \qquad \rho_i = n_i M_i \qquad m_i = \frac{M_i}{N_\mathrm{A}} \tag{B.2}$$

Simililarly to the global molar/number senity, the global density will be given by the sum of each partial desnity, given in eqaution B.3

$$\rho = \sum_s \rho_s \tag{B.3}$$

With these quantities, it is possible to obtain the dimensioneless composition properties, given in equation B.4, that are the mass fraction c_i , and the molar fraction x_i, respectively.

$$c_i = \frac{\rho_i}{\rho} \qquad x_i = \frac{N_i}{N} = \frac{n_i}{n} \qquad \sum_i c_i = \sum_i x_i = 1 \tag{B.4}$$

Each dimensionless composition variable is related to one another by the equations B.5,

$$x_i = \frac{M c_i}{M_i} \qquad n_i = \frac{x_i \rho}{M} \qquad c_i = \frac{n_i M_i}{\rho} \tag{B.5}$$

,where M is the molar mass of the global mixture and it can be given by equation B.6.

$$M = \sum_i x_i M_i = \left(\sum_i \frac{c_i}{M_i} \right)^{-1} = \frac{1}{n} \sum_i n_i M_i \tag{B.6}$$

B.2 Equation of state

For this work, it is assumed that each chemical species behaves as an ideal gas, and under theses conditions, the Dalton's law of partial pressures is given by B.7.

$$p = \sum_i p_i \tag{B.7}$$

Each partial pressure p_i will obey to the equation of state given in equations B.8, rewritten in more than one format, where V is the volume of the global mixture and R_i is the specific gas constant.

$$p_i = \rho_i R_i T, \quad p_i = \frac{n_i}{V} R_u T \quad \text{or} \quad p_i = \frac{N_i}{V} k_B T \tag{B.8}$$

The specific gas constant R_i can be written in terms of the universal gas constant R or to the Boltzmann constant k_B, given in equation B.9.

$$R_i = \frac{R_u}{M_i} = \frac{N_A k_B}{M_i} = \frac{k_B}{m_i} = \frac{R/N_A}{m_i} \tag{B.9}$$

B.3 Calorific Equations of State

The specific internal energy and enthalpy of a gas mixture are a function of temperature and volume, and temperature and pressure, respectively.

$$e = e(T, v) \tag{B.10a}$$

$$h = h(T, p) \tag{B.10b}$$

By differentiating B.10b and B.10a, general equations for e and h are given in B.11a and B.11b, respectively.

$$\mathrm{d}e = \left(\frac{\partial e}{\partial T} \right)_v \mathrm{d}T + \left(\frac{\partial e}{\partial e} \right)_T \mathrm{d}v \tag{B.11a}$$

$$\mathrm{d}h = \left(\frac{\partial h}{\partial T} \right)_p \mathrm{d}T + \left(\frac{\partial h}{\partial p} \right)_T \mathrm{d}p \tag{B.11b}$$

The partial derivatives with respect to temperature, are the constant pressure and constant temperature specific heats, respectively, given in equations B.12a and B.12a.

$$c_v \equiv \left(\frac{\partial u}{\partial T} \right)_v \tag{B.12a}$$

$$c_p \equiv \left(\frac{\partial h}{\partial T}\right)_P \tag{B.12b}$$

Since it is assumed that each chemical species behaves as an ideal gas, the partial derivatives with respect to specific volume are zero.

By integrating equation B.11b, each chemical species specific enthalpy is given by B.13, where h_i^* is the species enthalpy density of formation at the reference temperature T^*, and c_{p_i} the species specific heat at constant pressure.

$$h_i = h_i^* + \int_{T^*}^{T} c_{p_i}(T)\mathrm{d}T \tag{B.13}$$

Each specific heat c_{p_i} can be obtained using the polynomial in equation B.14, where each coefficient $b_{n,i}$ from $b_{1,i}$ to $b_{9,i}$ are the numerical coefficients supplied in NASA thermodynamic files.

$$\frac{c_{p_i}}{R} = \sum_{n=1}^{9} b_{n,i} T^{n-1} \tag{B.14}$$

The mixture specific heat c_p will be given by the sum of each c_{p_i} times the species mass fraction c_i.

$$c_p = \sum_{i=1}^{N_s} c_i c_{p_i} \tag{B.15}$$

To obtain the specific enthalpy, it can be given by the sum of each chemical species specific enthalpy times its mass fraction, given in equation B.16.

$$h = \sum_i c_i h_i \tag{B.16}$$

The Heat capacity ratio is given by B.17.

$$\gamma = \frac{c_p}{c_v} \tag{B.17}$$

Appendix C

Kinetics

C.1 Reaction Rate Constant Models

When considering temperature dependent reactions, the main approach used to compute the reaction rate constant is the Arrhenius reaction rate model, given in equation C.1, where A is the pre exponential factor, n is the temperature exponent, and E_a is the activation energy for the reaction.

$$k = AT^n e^{-\frac{E_a}{RT}} \tag{C.1}$$

When the same reaction has two distinct set of Arrhenius parameters it can be useful to use a “mixed” reaction rate with these two sets of values, one obtained at low temperatures (lT), and the other at high temperatures (hT). This is given in equation C.2.

$$\begin{aligned} k_{\text{duplicate}} &= k_{lT} + k_{hT} \\ &= A_{lT} T^{n_{lT}} e^{-\frac{E_a lT}{RT}} + A_{hT} T^{n_{hT}} e^{-\frac{E_a hT}{RT}} \end{aligned} \tag{C.2}$$

For some conditions, reactions rates can depend not only on temperature, but also pressure. In this kind of situation, the Arrhenius law can’t model the rate constant correctly, so others models are available. The one presented next is the Troe formalism, where the reaction rate constant is given by equation C.3.

$$k = k_\infty \left(\frac{P_r}{1 + P_r} \right) F \tag{C.3}$$

Each parameter related to this model is given from equation C.4 to C.11, where P_r is called the reduced pressure, and $[M]$ is the mixture enhanced concentration considering third body efficiencies.

$$k_\infty = A_\infty T^{n_\infty} e^{-\frac{E_a \infty}{RT}} \tag{C.4}$$

$$k_0 = A_0 T^{n_0} e^{-\frac{E_a}{RT}} \tag{C.5}$$

$$P_r = \frac{k_0[M]}{k_\infty} \tag{C.6}$$

$$\log F = \left[1 + \left[\frac{\log P_r + c}{n - d\left(\log P_r + c\right)}\right]^2\right]^{-1} \log F_{cent} \tag{C.7}$$

$$F_{cent} = (1-\alpha)e^{-\frac{T}{T^{**}}} + \alpha e^{-\frac{T}{T^{*}}} + e^{-\frac{T^{**}}{T}} \tag{C.8}$$

$$c = -0.4 - 0.67 \log F_{\text{cent}} \tag{C.9}$$

$$n = 0.75 - 1.27 \log F_{\text{cent}} \tag{C.10}$$

$$d = 0.14 \tag{C.11}$$

C.2 Kinetic Scheme

In this work, the high pressure $\mathrm{H_2/O_2}$ kinetic scheme updated by Burke et. al in [83] is used, and given in table C.1.

Table C.1: H_2/O_2 kinetic scheme in [83] with He as the bath gas.

			A	n	Ea	Ref.
(1)	H + O_2 = O + OH		1.04E+14	0.00	1.531E+04	[86]
(2)	O + H_2 = H + OH	Duplicate	3.82E+12	0.00	7.948E+03	[87]
	O + H_2 = H + OH	Duplicate	8.79E+14	0.00	1.917E+04	
(3)	H_2 + OH = H_2O + H		2.16E+08	1.51	3.430E+03	[88]
(4)	OH + OH = O + H_2O		3.34E+04	2.42	-1.930E+03	[87]
(5)	H_2 + M= H + H + M		4.58E+19	-1.40	1.040E+05	[89]
	ε_{H_2} = 2.5, ε_{H_2O} =12.0, ε_{He} = 0.0					
	H_2 + He = H + H + He		5.84E+18	-1.10	1.040E+05	
(6)	O + O + M = O_2 + M		6.16E+15	-0.50	0.000E+00	[89]
	ε_{H_2} = 2.5, ε_{H_2O} = 12.0, ε_{He} = 0.0					
	O + O + He = O_2 + He		1.89E+13	0.00	-1.790E+03	
(7)	O + H + M = OH + M		4.71E+18	-1.00	0.000E+00	[89]
	ε_{H_2} = 2.5, ε_{H_2O} = 12.0, ε_{He} = 0.75					
(8)	H_2O + M = H + OH + M		6.06E+27	-3.32	1.208E+05	[90]
	ε_{H_2} = 3.0, ε_{H_2O} = 0.0, ε_{O_2} = 1.5, ε_{He} = 1.1					
	H_2O + H_2O = H + OH + H_2O		1.01E+26	-2.44	1.202E+05	
(9)	H + O_2 + M = HO_2 +M		4.65E+12	0.44	0.000E+00	[91]
			9.04E+19	-1.50	4.920E+02	
	ε_{H_2} = 3.0, ε_{H_2O} = 21.0, ε_{O_2} = 1.1, ε_{He} = 1.2					
(10)	HO_2 + H = H_2 + O_2		2.75E+06	2.09	-1.451E+03	[92]x0.75
(11)	HO_2 + H = OH + OH		7.08E+13	0.00	2.950E+02	[93]
(12)	HO_2 + O = O_2 + OH		2.85E+10	1.00	-7.239E+02	[94]x0.6
(13)	HO_2 + OH = H_2O + O_2		2.89E+13	0.00	-4.970E+02	[95]
(14)	HO_2 + HO_2 = H_2O_2 + O_2	Duplicate	4.20E+14	0.00	1.200E+04	[96]
	HO_2 + HO_2 = H_2O_2 + O_2	Duplicate	1.30E+11	0.00	-1.630E+03	
(15)	H_2O_2 + M = OH + OH + M		2.00E+12	0.90	4.875E+04	[97]
			2.49E+24	-2.30	4.875E+04	
	ε_{H_2O} = 7.5, $\varepsilon_{H_2O_2}$ = 7.7,ε_{O_2} = 1.2, ε_{He} = 0.65, $\varepsilon_{H_2} = 3.7$					
(16)	H_2O_2 + H = H_2O + OH		2.41E+13	0.00	3.970E+03	[89]
(17)	H_2O_2 + H = HO_2 + H_2		4.82E+13	0.00	7.950E+03	[89]
(18)	H_2O_2 + O = OH + HO_2		9.55E+06	2.00	3.970E+03	[89]
(19)	H_2O_2 + OH = HO_2 + H_2O	Duplicate	1.74E+12	0.00	3.180E+02	[98]
	H_2O_2 + OH = HO_2 + H_2O	Duplicate	7.59E+13	0.00	7.270E+03	

Appendix D

Driver CFD Simulations

D.1 Temperature field

In this section, an example of previous simulations with the full driver is given. The initial conditions were 20bar, and a gas composition of $\mathrm{He}/\mathrm{H}_2/\mathrm{O}_2$ with a 6:2:1 ratio. The simulation was launched as a 2D axisymmetric flow, with walls as boundary conditions for the driver outer domain, and a symmetry condition on the driver axis.

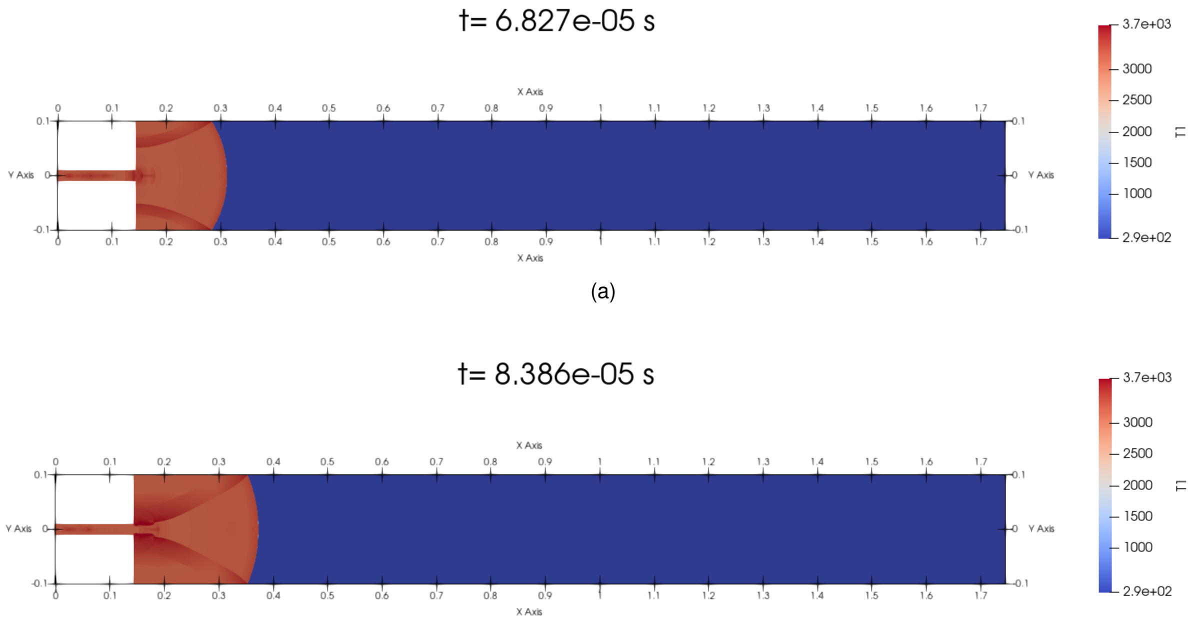

(a)

(b)

Figure D.1: Temperature field snapshots.

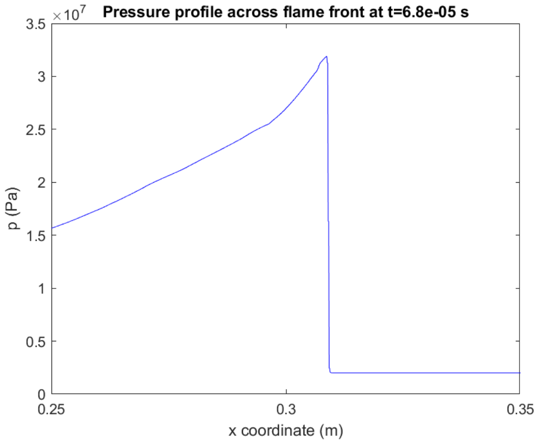

Figure D.2: Pressure profile across flame front.